Dynamical Decoupling using NMR for Quantum Computing

A thesis submitted for the degree of Doctor *rerum naturalium*
at the Faculty of Physics at TU Dortmund

Mustafa Ahmed Ali Ahmed

May 14, 2013

First referee: Prof. Dr. Dieter Suter
Second referee: Prof. Dr. Götz S. Uhrig

NMR probes are very expensive so extremely care is important

Contents

1. Introduction

Why quantum computers?

Quantum computers can execute certain tasks more efficiently than classical computers by processing information in a system governed by the laws of quantum mechanics. The basic unit of quantum computation is a qubit. A qubit is typically a microscopic system such as an atom or spin or photon [1]. A quantum mechanical two-level system (like a spin-1/2) can be used as a computational basis by identifying their eigenstates with these values, e.g. $|0\rangle$ for spin up and $|1\rangle$ for spin down.

One of the main advantages of quantum computers in contrast to classical computers is "quantum parallelism". Quantum parallelism is based on the superposition principle in quantum mechanics. The number of basis states for N qubit system is 2^N. Unlike in classical computers these states are established in superposition states. The number of parallel function evaluations grows exponentially with the number of qubits in quantum computers, whereas it increases linearly with the number of input bits in classical computers. This powerful computation algorithm, implemented in a quantum computer, makes it possible to solve problems which are hard or impossible for classical computers such as the factorization of large numbers Preskill [2], Vandersypen *et al.* [3], DiVincenzo [4].

Simulating quantum systems in a classical computers is awkward because the required resources grow exponentially with the system size (e.g. superposition states do not exist in classical computers). Inspired by Fredkin's results about reversible computations, Feynman thought in the opposite direction, that quantum simulations can be performed in a system built of quantum mechanical elements that obey quantum laws. Thus quantum computers can compute information more efficiently than any classical device [5, 6, 2, 7, 8].

NMR quantum computation

The principle of nuclear magnetic resonance (NMR) spectroscopy, where the nuclear magnetic moment is directly measured experimentally and nuclear precession is described, was first discovered by Rabi *et al.* in 1938. It has been fifty-nine years after this discovery, then NMR was realized as a quantum computational system by two groups working in liquid-state NMR. In that initial demonstrations the concept of bulk quantum computing is introduced. Bulk quantum computing depends on addressing the ensemble of approximately 10^{23} spins as one qubit [9, 10, 11].

The fascinating variety indiscipline fields of quantum mechanics in atomic physics, quantum optics, NMR, electron spin resonance ESR, superconducting physics and quantum dot research are connected to the quantum physics and quantum computation. NMR quantum information processing (QIP) was the first approach for quantum information systems listed by the advanced research and development activity (ARDA) based on their underlying experimental physics sub-fields, besides other approaches (such as trapped ions, trapped neutral atoms, cavity quantum electrodynamic, photons as optical qubits,

solid-state such as impurity spins and spins in quantum dots and superconducting circuits and "unique" qubits (e.g. electrons on liquid helium, spectral hole burning etc.)) [12]. The NMR quantum computation approach started as good testbed for the most conceptually advanced quantum information processors developments and is expected to remain in future applications Suter and Mahesh [8], Stolze and Suter [5], DiVincenzo [4], Vandersypen *et al.* [3].

If all these spins were distinguishable the result would be a massive quantum computer. However, partial distinguishability occurs naturally in molecules due to their electronic environments. The ability of the fine control of these nuclear spins which is implemented in NMR spectrometers through radio frequency pulses enables us to construct pulse sequences for quantum computation. This results in a great success achieved recently by NMR quantum information processing [7, 8, 11]. Another advantage of spin 1/2 qubits is that it exactly realizes a qubit in its two dimensional Hilbert space [8]. Since experimental systems have similar problems in quantum control, ideas and concepts from liquid-state NMR are adopted in a variety of other quantum computational implementations. On the other hand quantum computing also provides a new powerful and systematic perspective in NMR technique such as using Uhrig Dynamical Decoupling sequence (UDD) to improve the image quality in magnetic resonance imaging (MRI) for some tissue types [2, 13]. In hybrid systems like single nitrogen-vacancy defect (NV) center, it is used as an atomic-size magnetic field sensor to detect NMR from nanoscale samples, this technique is based on measuring the statistical polarization of the spin population near the NV center with a dynamical decoupling method [14].

In quantum information processing and quantum memory applications, it is very important to keep the information isolated from the environment: uncontrolled interactions with the environment tend to degrade the quantum information. This environment-induced loss of quantum information is called 'decoherence' [15, 16, 17]. Decoherence not only limits the time for which quantum information can be used, but also the distance over which quantum information can be transferred [18]. Successful quantum computations are scaled with the decoherence time. Avoiding decoherence is simply done by choosing systems with long decoherence times compared to gate times [4, 19]. Towards implementing a fault-tolerant quantum computer in a physical system, DiVincenzo suggested five requirements as discussed in NMR point of view in Sec. (2.3.1). In Ref. [20] the the DiVincenzo's criteria is generalized into

1. Scalability : the system should be able to grow in the Hilbert space exponentially without exponential cost of resources.

2. Universal logic : this follows the DiVincenzo's criterion where the system in the large Hilbert space should be accessible through a finite set of control operation.

3. Correctability : in order to make operations in the initialized computer state, it must be possible to remove the errors introduced by the influence from the outside world of the quantum computer.

The criteria required the ability of fast switching between measurement "on" to readout the results and "off" during computation to avoid decoherence. Therefore quantum computation looks hard because qubits should strongly interact with each other and not interact with the environment until we measure them. In practical systems coherent control pro-

cesses suffer from imperfections in the control field of the qubits. These imperfections can limit the computer's performance more than decoherence itself [20, 8].

Dynamical decoupling

One of the biggest challenges for many qubit systems such as NMR is understanding and eliminating decoherence [20]. If one is able to control the system and thereby reduces the detrimental effect of the system-environment (SE) interaction, one can preserve the quantum state for a longer time. This way of fighting decoherence by applying fast and strong pulses has been termed dynamical decoupling (DD). DD techniques originate from NMR spectroscopy [21, 22, 23, 24, 25, 26]. The main attraction of DD is that it requires few additional resources. In contrast to quantum error correction (QEC) ,e.g., it does not require additional qubits. QEC assumes that encoding and error correction are error free [27, 28, 29, 30]. DD can be traced back to Hahn's 'spin echo' experiment, where a refocusing pulse induces a time reversal of the SE interaction of nuclear spins [31]. This increases the decay time or decoherence time of the stored information in the qubit. The technique has evolved significantly since then and its efficiency was studied, developed and demonstrated in many different systems [32, 33, 34, 35, 36, 37, 38, 39, 40, 41, 42, 43, 44, 45, 46, 47, 48].

It has been shown that the type as well as the spectral density of the SE interaction play a significant role in finding the optimal DD sequences Kofman and Kurizki [49, 50], Zhang *et al.* [51], Gordon *et al.* [24], Bhaktavatsala Rao and Kurizki [52], Bylander *et al.* [53], Álvarez and Suter [54], Almog *et al.* [43], Kotler *et al.* [55], Bar-Gill *et al.* [56]. Furthermore, unavoidable errors in the control pulses are also an important source of decoherence [57, 58, 36, 42, 59, 60, 61, 62, 63, 64, 65, 66, 19]. Therefore optimal DD sequences must be able to reduce the effective SE interaction while compensating the effects of non-ideal control fields [67, 40, 42, 66, 61, 64, 68, 65, 19]. There are several ways to improve DD schemes, reference [66] is a recent review of this subject.

The goal of this thesis is focused on enhancement of the coherence times obtained by DD sequences. Towards this goal we compare the performance of different DD sequences in a system where pulse errors are the dominant source of decoherence. In our system, pulse errors become the most significant effect because most of the effects of the SE interaction have been eliminated. To this end, we prepare a system where the spectral density of the SE coupling has two main contributions. One source of noise is almost static and can therefore be refocused by all tested DD sequences. The other contribution is a rapidly fluctuating noise, whose correlation time is much shorter than the time required for an inversion of the spins. This type of noise cannot be refocused by any DD sequence. Therefore the main difference between the performance of the DD sequences is their susceptibility to pulse errors. The optimum DD sequence should have the longest coherence time and minimal resources.

In this work [36, 42], in particular it has been found that the Carr, Purcell, Meiboom and Gill (CPMG) sequence [69, 70], a well known sequence in the NMR community, is strongly initial state dependent and performed particularly well for specific initial states. In this case the decoherence time was one order of magnitude longer than the robust sequences that reduced decoherence symmetrically with respect to arbitrary initial states. We found that this difference arose because the system qubit, a ^{13}C spin, interacted with neighboring ^{13}C spins. While the CPMG sequence was able to reduce the effect of $^{13}C-^{13}C$ couplings,

the robust sequences were not [54]. Since the tested DD sequences were not designed for eliminating the effect of homonuclear couplings, the longer decoherence times for CPMG applied to certain initial conditions cannot be taken as a measure of its performance. In this work we therefore use a system that does not exhibit homonuclear interactions. This allows us to show that the robust sequences can also achieve optimal decoherence time observed under CPMG, and this performance is independent of initial condition.

The next chapters in this thesis are organized as follows. We give a brief introduction to NMR and quantum computation in the second chapter. In the third chapter the experimental setup of the spectrometer is discussed. A new setup for the H-channel is proposed. We have also introduced some measurement for the electronic noise in the receiving part of the spectrometer and solutions to reduce the noise. Optimization procedures for system preparation is also described. This includes optimizing pulses using tune-up sequences and preparing the system to avoid long experimental times and obstacle for NMR experiments such as radiation damping. In chapter four we introduce the DD sequences under our environmental consideration and compare their robustness against pulse error effects for the prepared system. To complete the picture we give the theoretical analysis of the underlying physics in terms of the average Hamiltonian theory taking pulses length errors into account. Then we introduce an approach to engineer the environment by applying additional signals to the system. For that we need to build a new coil and provide additional devices for the setup. In the last chapter we draw some conclusions. For future work we have suggested a molecule of five-spin system for testing dynamical decoupling sequences. In the appendix (a) I show a protocol for testing the NMR signal through different devices in the 360 MHz spectrometer, in which some of the errors look trivial but are likely to occur. In (b) and (c) two interpreter pulse programs are included with a brief description..

2. NMR basics

2.1. Theoretical background

Matter is composed of atoms which contains electrons and protons, these charged particles give atoms their different physical and chemical properties. NMR spectroscopy is based upon the fact that nuclei have angular momentum. Particularly NMR technique measure protons angular magnetic momentum in medical applications, termed magnetic resonance imaging (MRI), however other nuclei such as ^{13}C are used for other applications[71, 72]. In quantum mechanics the total spin angular momentum of any physical system $\vec{S}$ is quantized so the allowed value are $\hbar\sqrt{s(s+1)}$, similar like other angular momentum, where $\hbar = h/2\pi$, h is Planck's constant, s is the spin quantum number which can take the values 0, 1/2, 1, 3/2, 2, etc [73].

Substances exposed to magnetic fields possess magnetic interaction energy gives by Eq. (2.1.1), depending on the magnetic field strength $\vec{B}_0$ and the magnetic moment $\vec{\mu}$.

$$E = -\vec{\mu}\vec{B}_0. \tag{2.1.1}$$

Since $\vec{\mu}$ and $\vec{B}_0$ are vector quantities, the dot product with the negative sign indicates that the magnetic energy will reach the minimum when the magnetic moment $\vec{\mu}$ is parallel to $\vec{B}_0$ field [74, 75].

Detection of different materials in NMR depends on their gyromagnetic ratio γ unit: (rad/sec·T), which is the proportional constant between the magnetic moment and the spin angular momentum $\vec{S}$. As shown in Eq. (2.1.2) nuclei with higher gyromagnetic ratio have higher magnetic moment thus higher detection sensitivity [76].

$$\vec{\mu} = \gamma\vec{S}. \tag{2.1.2}$$

There are two type of materials, the first type has intrinsic magnetism. It tends to align with an external magnetic field e.g. the earth magnetic field. The second type show induced magnetism in a magnetic field. This induced magnetism is proportional to the magnetic field given by Eq. (2.1.3).

$$\vec{\mu}_{induced} = \frac{1}{\mu_0} V\chi\vec{B}_0, \tag{2.1.3}$$

where: $\mu_0 = 4\pi\times10^{-7}$ (Henry/m) is the magnetic susceptibility of the vacuum, V represents volume and χ is the magnetic susceptibility, a dimensionless constant that indicates the degree of magnetization of the material when the magnetic field $\vec{B}_0$ is applied [74].

2.1.1. The nuclear Zeeman effect

Application of a magnetic field breaks the degeneracy of the nuclear spin state. A nucleus with nuclear spin $s = 1/2$ will split $2s + 1$ in presence of a magnetic field[1]. This is known as Zeeman effect[74]. Equation (2.1.4) shows the Hamiltonian operator for a magnetic field oriented along the z-axis in terms of the angular momentum operator along z-axis $\hat{I}_z$, as in Figure 2.1.1, the splitting energy is magnetic field dependent.

$$\hat{\mathcal{H}} = -\gamma\hbar B_0 \hat{I}_z. \tag{2.1.4}$$

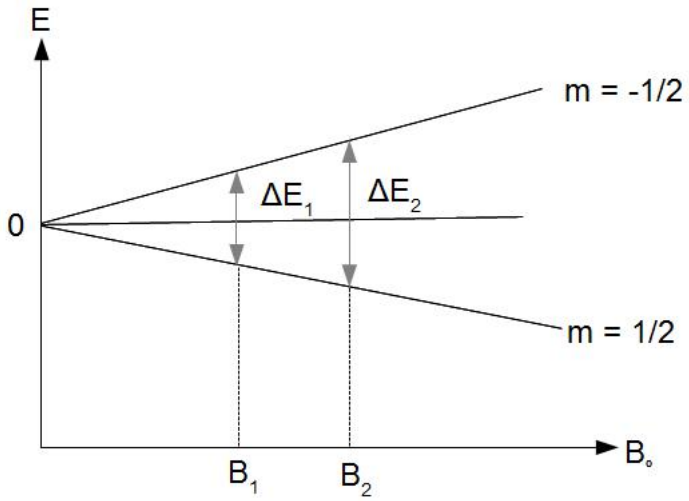

Figure 2.1.1.: Energy differences of two adjacent levels as a function of the magnetic field.

Consider a nuclear spin quantum state $|\psi\rangle$we can describe the system dynamics using the Schrödinger Eq. (2.1.5)

$$i\hbar\frac{\partial}{\partial t}|\psi\rangle = \hat{\mathcal{H}}|\psi\rangle. \tag{2.1.5}$$

If the energy operator Hamiltonian $\hat{\mathcal{H}}$ is time-independent, we can solve Eq. (2.1.5) using the evolution operator as in Eq. (2.1.7):

$$|\psi\rangle(t) = U(t)|\psi\rangle(0), \tag{2.1.6}$$

where $U(t)$ in Eq. (2.1.6), the evolution operator takes the form:

$$U(t) = exp(-i\hat{\mathcal{H}}t/\hbar). \tag{2.1.7}$$

For spin-1/2 the angular momentum operator for z components has two eigenfunctions labeled $m_z = \pm 1/2$. Using Eq. (2.1.4) we get two energy levels in a single spin-1/2 in a magnetic field labeled E_α, E_β:

[1]Nuclei which has non-spherical charge distribution, also called quadrupolar nuclei, have a spin number s grater than 1/2 e.g. 1, 3/2, 5/2,..,etc. Spin 1/2 nuclei have two orientations while Spin 1 nuclei have three orientations such as Deuterium (s=1).

$$E_\alpha = -\frac{1}{2}\hbar\gamma B_0 \quad , \quad E_\beta = +\frac{1}{2}\hbar\gamma B_0. \tag{2.1.8}$$

Transitions are only allowed between E_α and E_β as in Eq. (2.1.8).

2.1.2. Precession and Larmor condition

In a typical NMR sample such as liquid water, nuclear magnetic moments are pointing in all possible directions. If we immerse this sample in a magnetic field B, the magnetic moment of the spin precess around the field on a cone keeping a constant angle between the spin magnetic moment and the field.

Spin precession depends on the energy difference ΔE between the two levels in Eq. (2.1.8), where transition are possible when the external magnetic field fulfills Eq. 2.1.9 where ω_0 is called the Larmor frequency.

$$\omega_0 = \gamma B_0. \tag{2.1.9}$$

To calculate the energy difference $\triangle E$ we use Boltzmann's relationship (2.1.10):

$$\triangle E = e^{-\frac{\gamma\hbar B_0}{k_B T}} \approx 1 - \frac{\gamma\hbar B_0}{k_B T}. \tag{2.1.10}$$

If we consider an NMR sample in a magnetic field 8.4555 Tesla at 300 k using Eq. (2.1.10) for proton:

$\nu_\circ = \omega_\circ/2\pi = 360$ MHz, $\gamma\hbar B_\circ = 360$ MHz$\cdot 6.62 \cdot 10^{-34}$ J$\cdot$s$=2.38 \cdot 10^{-25}$ J

The denominator gives: $k_B T = 1.38 \cdot 10^{-23}$ J/K$\cdot 300$ K$= 4.14 \cdot 10^{-21}$ J.

The sensitivity of the NMR signal depends on this energy difference, as illustrated in the example above, the ratio approaches $\approx 10^{-4}$ so the sensitivity to detect an NMR signal proportional with the difference which is 1 part in $5 \cdot 10^3$. The Larmor frequency for the nucleus changes slightly with different molecular environment in the NMR sample. This small variations causes small shifts in the NMR spectrum, on the order of 1 part in 10^9 which known as chemical shift in NMR spectroscopy. Chemical Shift is very useful in studying different chemical compounds and their properties [2][75].

2.1.3. Density matrix operator

Let us consider an NMR sample which contains protons such as in pure water. This bulk sample contain approx. 10^{23} protons (i.e. spins) ml^{-1}, which have different orientations for magnetic moment and precess independently. These spins known as ensemble. We classically i.e in the experiment, measure the average magnetization overall spins. Magnetization is a macroscopic quantity. The way to solve that is to use the method of the density operator. Consider spin $\frac{1}{2}$, using the wave function $\psi = a\,|\alpha\rangle + b\,|\beta\rangle$ where $|a|^2 + |b|^2 = 1$ and $|\alpha\rangle$,$|\beta\rangle$ are the eigenstate of the operator $\hat{I}_z$ with eigenvalue $\pm\frac{1}{2}$. The coefficients a and b are different for all spins in the ensemble. The average is taken over the whole sample with N spins is given by Eq. (2.1.13).

The eigenvalue equation of the angular momentum operator $\hat{I}_z$ is written for base states $|\alpha\rangle$ with eigenvalue $\frac{1}{2}$:

[2] A good online book about NMR: `http://www.cis.rit.edu/htbooks/nmr/inside.htm`

$$\hat{I}_z \left|\alpha\right\rangle = +\frac{1}{2} \left|\alpha\right\rangle . \tag{2.1.11}$$

Besides $\hat{I}_z$ we define the angular momentum operators $\hat{I}_y$ and $\hat{I}_z$ which do not commute with each other according to the commutation relation Eq. (2.1.12):

$$[\hat{I}_x, \hat{I}_y] = i\hat{I}_z. \tag{2.1.12}$$

We can write the density matrix ρ with the matrix elements m,n as in Eq. (2.1.13)

$$\rho_{mn} = \langle m \left|\rho\right| n\rangle = \overline{a_m^* b_n} = \frac{1}{N} \sum_i a_i^* b_i, \tag{2.1.13}$$

ρ contains all information about the ensemble, so any operator $\hat{O}$ may be written as

$$\overline{\left\langle \psi \left|\hat{O}\right| \psi \right\rangle} = Tr(\hat{O}\hat{\rho}), \tag{2.1.14}$$

where the right hand side of Eq. (2.1.14) represents the trace over the matrix product.

Further more, the variation of $\hat{\rho}$ with time may be written using the Schrödinger Eq. (2.1.5) :

$$i\frac{\partial \hat{\rho}(t)}{\partial t} = \left[\hat{\mathcal{H}}, \hat{\rho}(t)\right] . \tag{2.1.15}$$

Equation (2.1.15) known as Liouville-von Neumann equation. We can also write $\hat{\rho}(t)$ (i.e. in the interaction picture) in terms of $\hat{\rho}(0)$ in the case of time independent-hamiltonian $\hat{\mathcal{H}}$ as:

$$\hat{\rho}(t) = \hat{U}(t)\hat{\rho}(0)\hat{U}^{-1}(t), \tag{2.1.16}$$

where $\hat{U}$ is defined in Eq. (2.1.7)[75, 71, 77].

2.1.4. Radio frequency pulses

The magnetization vector precess in a cone around the z axis due to Zeeman field as we discuss in Section (2.1.2). This Zeeman field is usually took place by a powerful superconducting magnet. So now we need to detect NMR signal. Applying a radio frequency field (rf) - usually pulses - with frequency at or near the Larmor frequency $\omega_\circ$ to the NMR coil where the sample is located generates a magnetic field B_1 rotating at the Larmor frequency ω_0. This magnetic field B_1 is week compared to the Zeeman field. However this rf field is able to tilt the field to the xy plane for detection when the resonance condition is met (i.e. the rf pulses is equal to the Larmor frequency).

2.1.5. Laboratory frame and rotating frame of reference

This rf field B_1 is applied to set of spins in a field. Suppose we move to a co-ordinate system which is no more static (laboratory frame) but rotating in the same direction and at the same rate of the field B_1. This called the rotating reference frame. This treatment removes the time dependence from the rf field B_1 and let it appear stationary, in simple

analogy the car driver in Figure 2.1.2 will be appear constant when the observer changes his co-ordinate to the car co-ordinate[71].

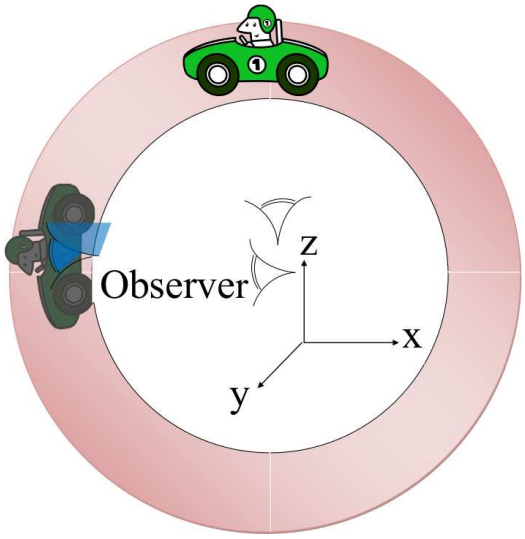

Figure 2.1.2.: Observer reference frame and rotating frame.

Accordingly the Hamiltonian in the laboratory frame may be written as a sum of two components from the rf field and the Zeeman field where the two components are rotating in the same direction as spin precession where the counter rotating component is ignored at the resonance condition $\omega = \omega_\circ$ due to $B_1 \ll B_\circ$ Eq. (2.1.17) :

$$\hat{\mathcal{H}}_{Lab} = -\gamma B_0 \hat{I}_z - 2\gamma B_1 cos(\omega t)\hat{I}_x \tag{2.1.17}$$

Since we assume we are in the rotating frame, the frequency will reduced by ω and the apparent longitudinal field vanishes leaving the effective field in the rotating frame so Eq. (2.1.17) becomes:

$$\hat{\mathcal{H}}_{rot} = -\gamma(B_0 - \omega/\gamma)\hat{I}_z - \gamma B_1 \hat{I}_x \tag{2.1.18}$$

2.1.6. Bloch equations

Describing spins in motion in macroscopic model, the torque is the rate of change of angular momentum $\vec{M}/\gamma$, so we can write the equation of motion for the magnetization vector $\vec{M}$ as :

$$\frac{d\vec{M}}{dt} = \gamma \vec{M} \times \vec{B}, \tag{2.1.19}$$

where B in Eq. (2.1.19) is the magnetic field with amplitude $\vec{B}_0$ corresponding to the precession of the magnetization at the Larmor frequency in static field in the z direction. The trend of the magnetization towards its equilibrium value $M_z = M_0$ can be describe using the Eq. (2.1.20)

$$\frac{dM_z}{dt} = -\frac{(M_z - M_0)}{T_1}, \tag{2.1.20}$$

where $T_1$is the longitudinal relaxation time which concerned the drift of the magnetization towards their thermal equilibrium value. Applying small rf field, will add a component to the nuclear magnetization and because the spins are not free but rather interacting with each other and their surrounding environment, the transverse magnetization decays also according to Eq. (2.1.21)

$$\frac{dM_x}{dt} = -\frac{M_x}{T_2}, \frac{dM_y}{dt} = -\frac{M_y}{T_2}, \tag{2.1.21}$$

where $T_2$is the transverse relaxation time which concerned the decay of the coherence between $|\alpha\rangle$,$|\beta\rangle$.

For short strong rf pulses one can write the oscillatory component of the rf transverse field

$$\hat{B}_1(t) = \frac{-\omega_{nut}}{\gamma} cos(\phi)\hat{i} - (\frac{\omega_{nut}}{-\gamma})sin(\phi)\hat{j}, \tag{2.1.22}$$

where $\hat{i}, \hat{j}, \hat{k}$ are unit vector along x, y, z. In the rotating frame, as in the previous Section (2.1.5), it shows that there is an effective static field given by Eq. (2.1.24) and the nutation frequency of the rf field $\omega_{nut}$is calculated the flip angle and the pulse width τ_p using Eq. (2.1.23)

$$\beta_p = \omega_{nut}\tau_p, \tag{2.1.23}$$

$$\vec{B_{eff}} = (B_0 + \frac{\omega}{\gamma})\hat{k} + \hat{B}_1, \tag{2.1.24}$$

where ω is the rotating frame frequency. Assuming that B_1 has only one component in the x direction i.e. $\phi = 0$ we can write the effective field in Eq. (2.1.24)

$$\vec{B_{eff}} = \frac{\Delta\omega_0\hat{k} - \omega_{nut}\hat{i}}{\gamma}, \tag{2.1.25}$$

where $\triangle\omega_\circ = \omega_- \omega_\circ$.

The total rate of change of the magnetization can be calculate by adding Eqs. (2.1.20),(2.1.21) to the rf field $\hat{B}_1$ using the equation of motion (2.1.19) as

$$\frac{d\tilde{M}}{dt} = \gamma((\tilde{M}_x\hat{i} + \tilde{M}_y\hat{j} + M_z\hat{k}) \times \vec{B_{eff}}) - \frac{(\tilde{M}_x\hat{i} + \tilde{M}_y\hat{j})}{T_2} - \frac{(M_z - M_0)\hat{k}}{T_1}, \tag{2.1.26}$$

where $\tilde{M}_x$, $\tilde{M}_y$ is the transversal magnetization component in the rotating frame.

From Eq. (2.1.26) we obtain the Bloch differential equations which provide a general frame work for treating the magnetization under the previous conditions

$$\frac{d\tilde{M}_x}{dt} = -\tilde{M}_x + \Delta\omega_0\tilde{M}_y, \tag{2.1.27}$$

$$\frac{d\tilde{M}_y}{dt} = -\Delta\omega_0\tilde{M}_x - \frac{\tilde{M}_y}{T_2} - \omega_{nut}M_z, \tag{2.1.28}$$

$$\frac{dM_z}{dt} = \frac{-(M_z - M_0)}{T_1} + \omega_{nut}\tilde{M}_y. \tag{2.1.29}$$

The transverse component M_x , M_y in the laboratory frame could be calculated from the rotating component $\tilde{M}_x$, $\tilde{M}_y$ using equations (2.1.30) , (2.1.31)

$$M_x = \tilde{M}_x cos(\omega t) - \tilde{M}_y sin(\omega t), \tag{2.1.30}$$

$$M_y = \tilde{M}_x sin(\omega t) + \tilde{M}_y cos(\omega t). \tag{2.1.31}$$

Bloch equations treats the dynamics of spins which experience rf fields and relaxation at the same time. On the other hand transverse relaxation destroy the transverse magnetization, so after long time the transverse magnetization should be zero. However at sufficient long time, the system settled down in a stationary state. As a result of this steady state the left terms on the Bloch equations (2.1.27), (2.1.28), (2.1.29) vanishes, because the magnetization components are not changing with the time. Solving the Bloch equations we can get the magnetization in the steady state $\tilde{M_{(ss)}}$ as a function of the offset from the resonance $\Delta\omega_0$, the relaxation times and the rf strengthω_{nut}

$$\tilde{M_{y(ss)}} = \frac{-(T_2\omega_{nut})}{(1+\omega_{nut}^2 T_1 T_2 + \Delta\omega_0^2 T_2^2)} M_\circ, \tag{2.1.32}$$

similarly we can write:

$$\tilde{M_{x(ss)}} = \frac{-(T_2^2\omega_{nut}\Delta\omega_0)}{(1+\omega_{nut}^2 T_1 T_2 + \Delta\omega_0^2 T_2^2)} M_\circ, \tag{2.1.33}$$

Equation (2.1.32) shows that the magnetization exist as long as T_2 is not too short and the nutation frequency ω_{nut} is not too large comparing to T_2, T_2. To simplify equations (2.1.32) , (2.1.33) we assume (T_1=T_2) and substitute ($a = -\Delta\omega_0 T$) and ($b = -T\omega_{nut}$) , then we can write

$$\tilde{M_{y(ss)}} = \frac{b}{(1+a^2+b^2)} M_0, \tag{2.1.34}$$

$$\tilde{M_{x(ss)}} = \frac{ab}{(1+a^2+b^2)} M_0, \tag{2.1.35}$$

Eq. (2.1.34) known as absorption mode where the optimum peak absorption occurs for (b=1) and Eq. (2.1.35) known as dispersion mode where it goes through zero on the exact resonance condition when (a=0)[75, 77, 78, 79].

2.2. Introduction to Quantum computation

Quantum computation is the study of information processing using quantum mechanical system. Quantum computers are designed to solve problems more efficiently than classical computer [17].

2.2.1. Quantum Bit

In analogy to the classical computational concept 'bit', quantum computation uses quantum bits or qubits for short. Computational basic states are $|0\rangle$and $|1\rangle$ which correspond to the classical states 0 and 1. Qubits are realized to be actual physical systems, however, qubits are treated as mathematical objects. So, unlike classical bit, it is also possible to have combination of states, known as superposition:

$$|\psi\rangle = a\,|0\rangle + b\,|1\rangle\,. \tag{2.2.1}$$

In Eq. (2.1.18) a and b give us the probability of finding the the basic computational states, so they summed to one $|a|^2 + |b|^2 = 1$.

If we add another qubit to our computational basic states, we obtain four computational basis state from two qubits denoted $|00\rangle$,$|01\rangle$,$|10\rangle$ and $|11\rangle$. Similar to one qubit Eq. (2.1.18), we can write a pair of qubits as superposition of those four states

$$|\psi\rangle = \alpha_{00}\,|00\rangle + \alpha_{01}\,|01\rangle + \alpha_{10}\,|10\rangle + \alpha_{11}\,|11\rangle\,, \tag{2.2.2}$$

where the total probability of measuring all possible x states is unity: $\sum_x |\alpha_x|^2 = 1$.

2.2.2. Single and multiple qubit gate

Quantum computers are built from quantum circuits containing "wires" and quantum gates to carry and manipulate information. As an example for single qubit gates which acts only on one qubit the "NOT" gate, takes the state $|0\rangle$ to $|1\rangle$ and vice versa and did not tell us what happened to the superposition of state $|0\rangle$ and $|1\rangle$ without further knowledge about the previous state. Representing NOT gate is possible in matrix form acting on one qubit by 2×2matrix. The quantum gate has this form :

$$NOT \equiv X = \begin{bmatrix} 0 & 1 \\ 1 & 0 \end{bmatrix},$$

and the quantum state represents with the vector notation: $\begin{bmatrix} a \\ b \end{bmatrix}$, the gate will act on the state by multiplying its matrix from the left as shown in Eq. (2.2.3):

$$X \begin{bmatrix} a \\ b \end{bmatrix} = \begin{bmatrix} b \\ a \end{bmatrix}. \tag{2.2.3}$$

Quantum gates have to be unitary, so the matrix describing the gate should be unitary, satisfying the condition Eq. (2.2.4) where X^* is the hermitian conjugate of X and I is the identity operator .

$$XX^* = I. \tag{2.2.4}$$

Reverse is an important feature of unitary operations. Thus reversible logic preserved information and consumes less power for computation in contrast to Boolean logic (which contains only true or false values). A typical multiqubit gate is the controlled gate or CNOT gate. U_{CNOT} (see Eq. 2.2.5) shows the matrix representation of the CNOT gate[5, 16].

$$U_{CNOT} = \begin{bmatrix} 1 & 0 & 0 & 0 \\ 0 & 1 & 0 & 0 \\ 0 & 0 & 0 & 1 \\ 0 & 0 & 1 & 0 \end{bmatrix}. \tag{2.2.5}$$

2.3. Liquid state NMR Quantum computing

NMR is concerned with measuring properties of liquids, solid and gases, determination the structure of molecules or imaging materials or investigating biological systems and monitoring interactions. Those many applications have led the technology of NMR to the current status. Recently NMR spectroscopy has also been used for quantum information processing (QIP). This new role relies on the capability of direct manipulation and detection of nuclear spin in NMR.

2.3.1. Quantum computer in DiVincenzo view

DiVincenzo discussed five requirement for quantum computer. Here, we discuss them from stand point of liquid state NMR :

1. Recognizing qubits is not trivial: We need for a quantum computer well characterized qubits i.e. their internal Hamiltonian and other physical properties e.g. interaction with other qubits should be well defined. In liquid NMR the bulk sample contains approx. 10^{23} spins can not be addressed individually. However the resonance frequency differentiates between the spins. Nevertheless they are not scalable.

2. State initialization: This initialization to well defined state can be done naturally i.e. the system is cooled to reach the ground state like NMR where this is achieved by relaxation.

3. Long decoherence times compared to gate times: Decoherence scale the computations, liquid state NMR has long decoherence times.

4. A universal set of quantum gates: A quantum algorithm is a sequence of unitary transformations acting on qubits. This is the heart of quantum computing and this is well done in liquid state NMR i.e these Hamiltonians are identified to physical specifications. Physical devices are designed to be turned on and off in defined intervals.

5. A qubit selective read out: At the end of the computational process, the result of the qubits should be read out with high efficiency. Liquid NMR address different qubits through their chemical shifts[5, 4].

2.3.2. Decoherence

It is the characterize the interaction of the qubit with its environment and one of the large obstacles in front of long computation scale. We can describe the life time of non-equilibrium classical state and quantum superposition through the relaxation times T_1,T_2.

One source of the decoherence is the phase randomization or thermalization of the spin to their equilibrium environment which originate from the spin spin coupling, usually represented with T_1, which are all irreversible processes. However the dephasing process results form the inhomogeneous static fields which leads the spins to presses with different rates. This shortens the coherence time, fortunately this a reversible process. These relaxations times formed the exponential decay in the magnetizations[4, 16].

3. Experimental setup

In this chapter we describe the main experimental configurations used in this work, including the detection and noise measurements and evaluation. This is followed by the sample preparation procedure and pulse parameters optimization.

3.1. Spectrometer configuration

It is familiar that NMR spectrometers are classified according to their field strength related with the Larmor frequency of the ^{1}H atom as in Eq. (2.1.9). In the 360 MHz spectrometer the superconducting magnet has a magnetic field strength $B_\circ$ of 8.4555 Tesla, which corresponds to the ^{1}H Larmor frequency 360 MHz, in the z direction.

3.1.1. Controlling the 360 MHz spectrometer

In the 360 MHz spectrometer setup a personal computer PC is used to control the different devices in the experiment. The PC (Mac-mini) controls the, direct digital synthesizers (DDS's), word generator, shim system and the oscilloscope using the MacExp as interface software. MacExp is a software package designed for Mac OX system with a flexible interface for different NMR experiment configurations, e.g. acquiring, processing and analyzing NMR data, streamlined and convenience. Communication signals are transmitted between the PC and other devices through Ethernet connections in a virtual local area network VLAN. Whereas MacExp is also used for other experimental configurations in our laboratories, this VLAN should be configured correctly to avoid conflicts between different devices which have the same IP addresses through the networks in the laboratories. Since the DDS's, the oscilloscope (Lecroy, Waverunner LT344), and the word generator have GPIB ports, they are controlled via GPIB-Ethernet converter (Ethernet Proglogix).

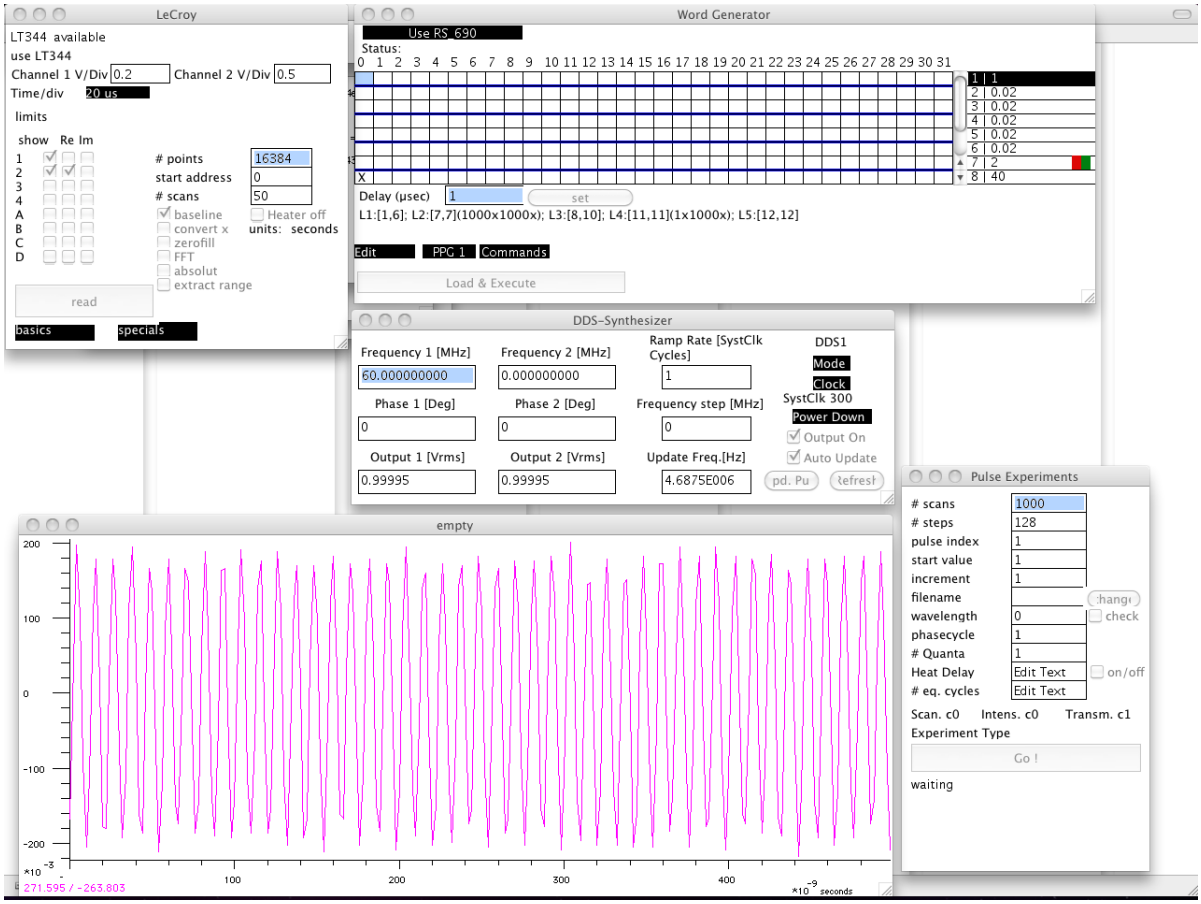

Figure 3.1.1.: Controlling the 360 MHz spectrometer.

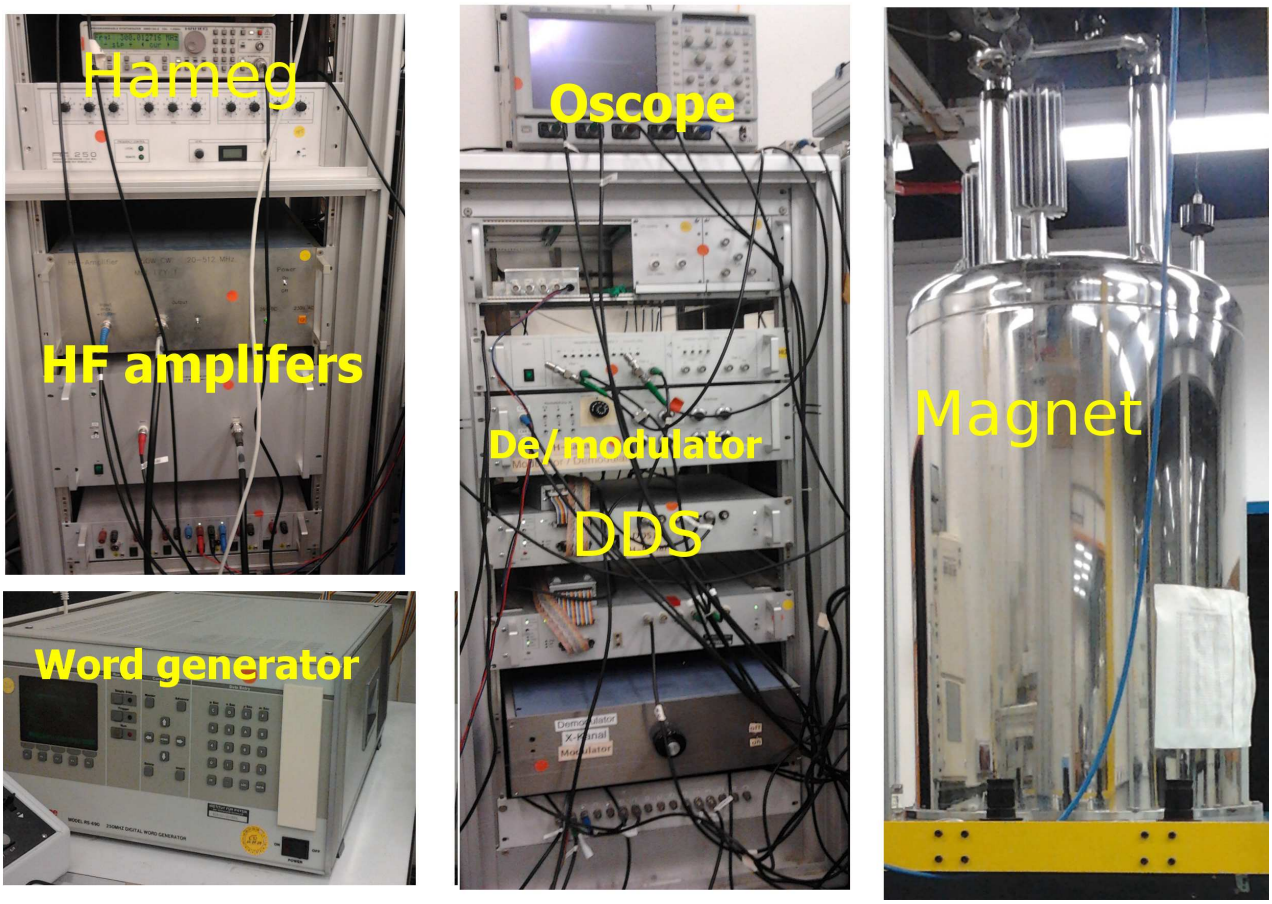

Figure 3.1.2.: Main components of the 360 MHz spectrometer.

Figure 3.1.1 illustrates control windows for the most important devices in the MacExp graphical interface. Using MacExp make it easy to run different types of experiments automatically e.g. multidimensional NMR experiments, storing the results sequentially and process them.

Figure 3.1.2 shows the main different components of the 360 MHz spectrometer. The spectrometer is composed of two channels, which are labeled usually ^{1}H-channel and X-channel, corresponds to the Larmor frequencies for each nucleus. The frequency of the X-channel can be varied to detect other active NMR nuclei around the 90 MHz. A block diagram of the 360 MHz spectrometer is drawn in Figure 3.1.3, where two main parts are separated from each other with the dashed box in the right hand side. Inside the dashed box is the transmitter section.

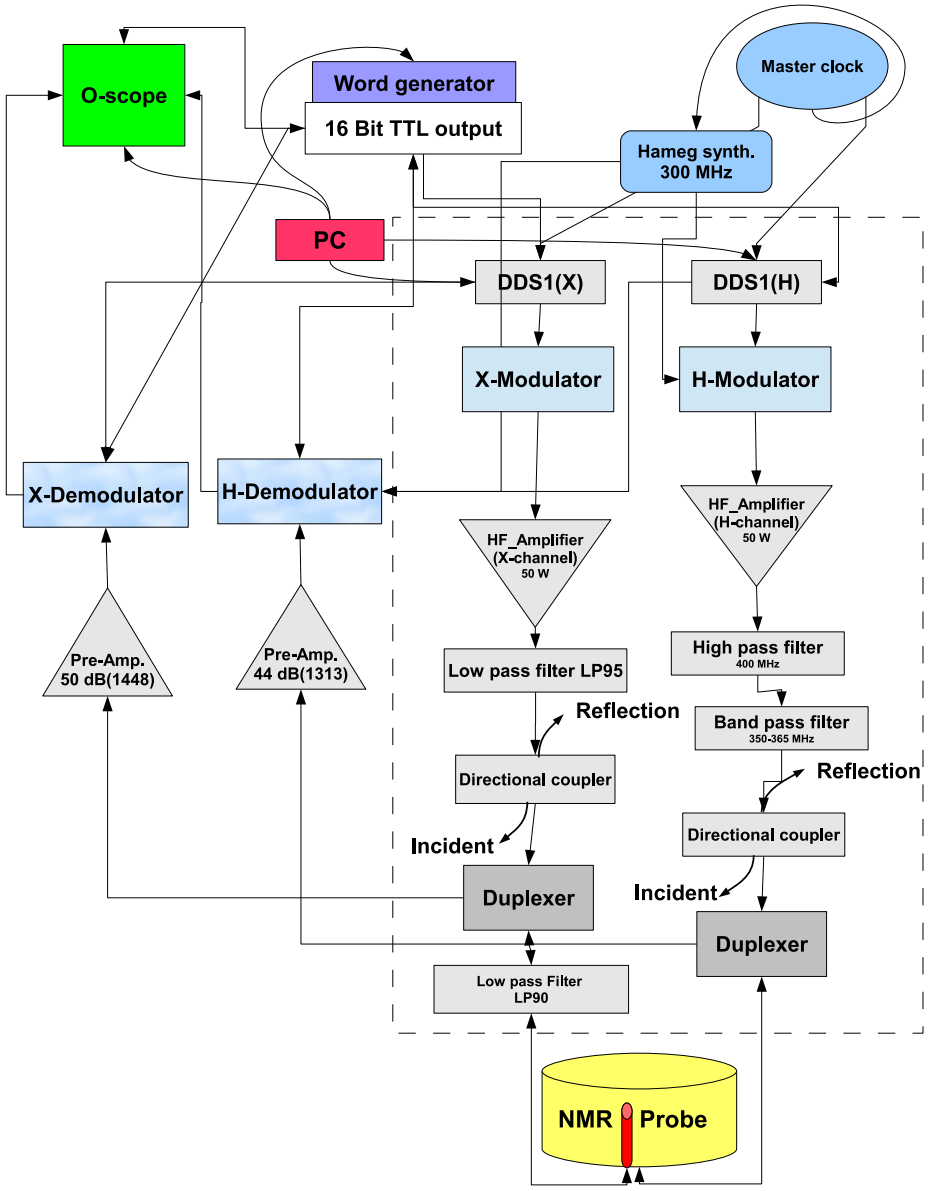

Figure 3.1.3.: Block diagram for the 360 MHz spectrometer.

3.1.2. The transmitter

The transmitter part generates rf pulses. Since most of the experiments in this work were done on the ^{1}H-channel, these rf pulses are usually close to the Larmor frequency of ^{1}H.

In the^{1}H-channel, the principle of mixing frequency, "intermediate frequency" is used. In the modulator which is shown inside the dashed box (Figure 3.1.4), the DDS1(H) generates a frequency of 60 MHz and the Hameg frequency synthesizer generates a frequency of 300 MHz, these frequencies are mixed using mixers. The mixer is a device composed usually of diodes, it uses the nonlinearity of the diode to generate an output contains the sum and the difference of the input signals. Mixers are called frequency translation devices. In the modulator the two signals are mixed and the rf pulses are modulated to be sent to the high frequency HF-amplifier, then the difference is filtered to obtain the 360 MHz[80, 81].

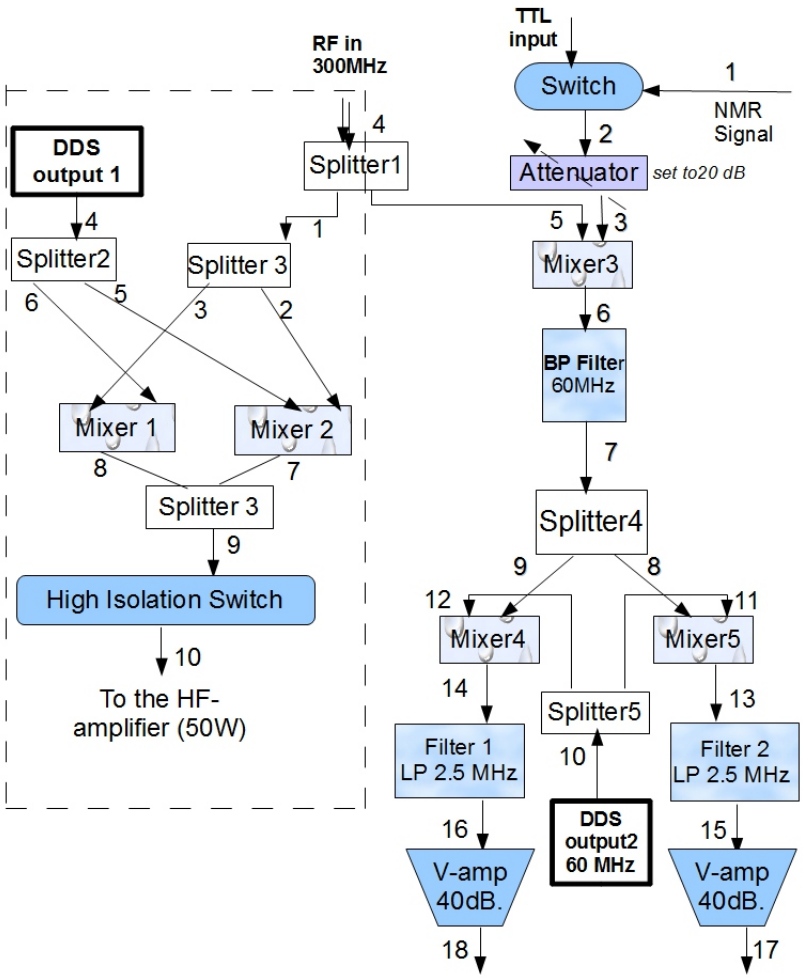

Figure 3.1.4.: Bloch diagram of the^{1}H-channel modulator/demodulator.

Consider the following equations (3.1.1), (3.1.2) to calculate the modulated frequency from the modulator at (10), Figure 3.1.4. The DDS1(H) has two output signals with relative 90° phase difference LO_1, LO_2. The output goes to mixer (1),mixer (2) in (see Figure 3.1.4) and ω_s from the rf Hameg frequency synthesizer (300 MHz):

$$LO_1 = \cos(\omega_{lo}t), \tag{3.1.1}$$

$$LO_2 = \sin(\omega_{lo}t), \tag{3.1.2}$$

then at the output of mixer(1) Figure 3.1.4 we get :

$$S_1 = \sin(\omega_s t)\cos(\omega_{lo}t) = \frac{1}{2}\left[\sin(\omega_s t - \omega_{lo}t) + \sin(\omega_s t + \omega_{lo}t)\right], \tag{3.1.3}$$

similarly for the other mixer2 we can write Eq. (3.1.4):

$$S_2 = \sin(\omega_s t)\sin(\omega_{lo}t) = \frac{1}{2}\left[\cos(\omega_s t - \omega_{lo}t) - \cos(\omega_s t + \omega_{lo}t)\right]. \tag{3.1.4}$$

Then shifting the output at (S_2) with 90°Eq. (3.1.4) yields:

$$S_2^{+90} = -\frac{1}{2}\left[\sin(\omega_s t - \omega_{lo}t) - \sin(\omega_s t + \omega_{lo}t)\right], \tag{3.1.5}$$

therefore adding (S_1), (S_2) from Eq. (3.1.3) and (3.1.5), the output signal (S_3):

$$S_3 = \sin((\omega_s + \omega_{lo})t) \tag{3.1.6}$$

The output pulses from the HF amplifier is filtered using a high-pass filter, then they are sent to the probe through the duplexer. It is worth noting here that the Hameg frequency synthesizer and the DDS1(H) should be synchronized with the master clock to have stable rf pulses with defined phases, so the DDS1(H) should use the external clock 10 MHz and the Hameg frequency synthesizer should be set to external trigger to the same clock. DDS1(H) output1 and DDS1(X) output1 could be varied to change the pulse power for both channels respectively. The duplexer keeps the rf pulses transmitted to the probe and protect the receiver circuit against high power rf pulses. The duplexer is composed of quarter-wave stub 'BNC' cable and crossed diodes, which attenuates the power at the defined frequency, and allow the rf pulse to pass to the probe and prevent the NMR signal from reflecting back to the modulator. These quarter waves cables with specific length work only for specific frequency (360 MHz, 90 MHz). It behaves as a transformer, in fact it is often referred to as a quarter-wave transformer and the input impedance is calculated using the Eq. (3.1.7)

$$Z_i = \frac{Z_0^2}{Z_l}, \tag{3.1.7}$$

where: Z_i is the input impedance, Z_l is the load impedance. In a simple way when Z_l =0, in a short cable there will be standing wave when the cable length matches the frequency and Z_i =∞, and so the impedance mismatching is used effectively for this application[74, 80, 82].

3.1.3. The RS690 word generator

The word generator acts as a heart of the spectrometer in time synchronization between different devices. It controls the pulse timing (width, delays) repetition rate with respect to internal trigger of the word generator. The minimum duration of the RS690 is 16 ns with resolution 4 ns, however it is set by default to a minimum duration of 20 ns. The maximum duration of the RS690 is 7500 μs, loops are used for longer durations. In a rectangular pulse train the duty cycle is defined as the ratio between the total pulse durations and the total period. For continuous rf irradiation the duty cycle is 100%. The Default maximum duty cycle value is set to 1% by MacExp. This value should be carefully adjusted taken into account not to exceed the maximum duty cycle of the probe maximum power. Time diagram of pulse sequence is produced using pulse programs which are read by the interpreter using the word generator. The word generator sends commands to control the experimental pulse parameter within the modulator and the demodulator through 16-bit TTL while other 32 ports are assigned to control the DDS's[83].

3.1.4. The Receiver

The receiver part picks the diverted NMR signal through the duplexer to the detection part. In the first stage the signal is amplified using the preamplifier, which should have low noise, high sensitivity, cover a wide frequency range and recover quickly from large overload signals. Then the signal is sent to the demodulator (see Figure 3.1.4). According to the current electronic circuit (Figure 3.1.4) for the H-demodulator ,the DDS1 output2 (used for detection) should be set from the DDS control panel to $\Longrightarrow$ 1 which gives 0.5V (+7 dBm) at the Mixer inputs$_{(LO)}$(4,5) where the mixer perform ideally. Similarly according to the current electronic circuit for the X-demodulator, the DDS2 output2 should be set from the DDS control panel to $\Longrightarrow$ 0.74 which gives also 0.5V (+7 dBm) at the Mixer inputs$_{(LO)}$. In NMR experiments, the detecting signal can be characterized through its amplitude, phase and frequency. To detect the phase a quadrature detector is used. The quadrature receiver combines the NMR signal which oscillates at Larmor frequency $\omega_\circ$ with a reference frequency ω_{rf} in order to generate a new signal which oscillates at a relative Larmor frequency, ω_1 as in Eq. (3.1.8) equal to the frequency in the rotating frame (see Sec. (2.1.2).

$$\omega_1 = \omega_0 - \omega_{rf}. \tag{3.1.8}$$

These relative frequencies ω_1 are quite low, usually in the Hz to kHz range. Cables should have defined lengths or symmetric to adjust the phase between the two outputs of the receiver which are 90° phase shifted with respect to each other, labeled as real and imaginary components of the NMR signal. These signals are considered to be equivalent to the projection of the transverse magnetization on to the x axis and y axis, they are assigned M_x and M_y respectively. The output signal is phase sensitive detected signal, i.e. it is DC coupled signal. However DC offset, e.g. from the amplifiers, is one of possible artifacts associated with the rf detector[76, 82].

3.1.5. Alternative ^{1}H-channel demodulator/modulator

In the first version of DDS (DDS1), the chip is able to generate maximum frequencies up to 120 MHz[83]. Under these conditions the DDS1 should be mixed with other high frequency to reach the 360 MHz. Different electronic components for the alternative ^{1}H demodulator/modulator is shown in Figure(3.1.5).

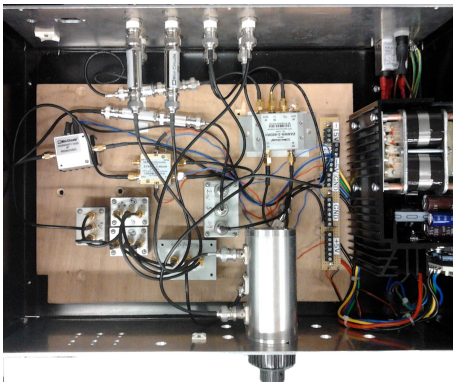

Figure 3.1.5.: Alternative ^{1}H-channel modulator/demodulator.

To eliminate the complexity of mixing frequencies we can use the third versions of DDS i.e. DDS3E to generate the rf frequency. DDS3E has the advantage of controlling through an Ethernet connection and it has a variable amplitude. Figure 3.1.6 illustrates a block diagram circuit for an alternative demodulator/modulator can be used for the ^{1}H channel without need of two sources and frequencies mixing.

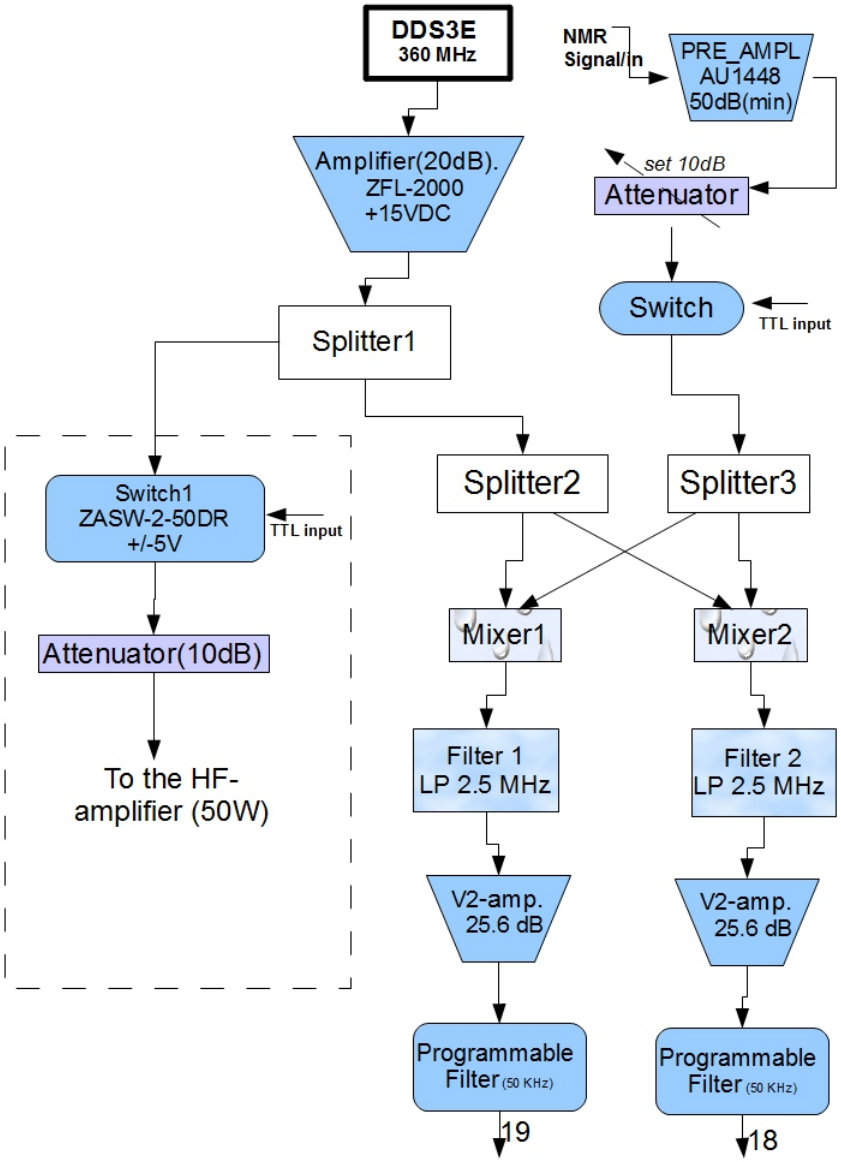

Figure 3.1.6.: Alternative[1]H-channel modulator/demodulator block diagram using the DDS3E.

3.1.6. The probe-head

The NMR probe-head keeps the sample in the region of the homogenous magnetic field which is commonly the center of the superconducting coils. The coil generates an oscillating magnetic field B_1 during the rf pulse, and detect the NMR signal using the induction principle. A poorly tuned probe reflects a lot of the power of the pulses, so that what should be a 90° pulse rf is in reality only ~ 50° pulse. As a result probe tuning affects the signal to noise ratio (S/N), where the signal will become worse due to mismatch between impedances.

When radio frequency power is transmitted over transmission lines some loss can occur

due to impedance mismatching between the probe and other circuits in the NMR spectrometer. The basic NMR probe circuit is consists of a coil which generates an oscillating magnetic field perpendicular to the main field at the sample during the rf pulse as input signal and then detects the precessing nuclear magnetization from the sample as output NMR signal. In liquid-state NMR probes saddle coils are used, and two variable capacitors, one of them called tuning capacitor (C_1), which is used to adjust the frequency to find the resonance frequency (to enhance the current in the coil by electromagnetic resonance), the other capacitor is used to match the impedance of the probe circuit to 50 Ω, known as matching capacitor (C_2). The circuit diagram is shown in Figure 3.1.7. The matching capacitor couples the external signals into the probe to avoid the power loss mentioned above. To avoid distortion, different components of the probe are preferred to be non-magnetic[84, 82, 76, 74, 73].

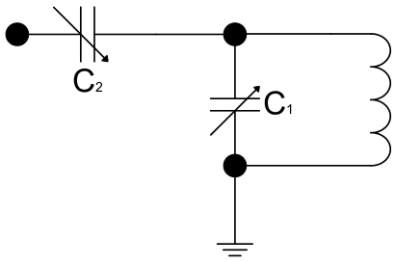

Figure 3.1.7.: Simple NMR probe circuit

Tuning the probe is done firstly using the network analyzer (8712ET) with changing the matching and tuning capacitors in order to get a good resonance shape at 360 MHz and 50 Ω impedance. The reflection power should be low with comparison to the incident power. In Figure 3.1.8 the network analyzer data shows that the reflected power was about -25.3 dB @ 360 MHz (that means 0.29% of the power is reflected back in this case).

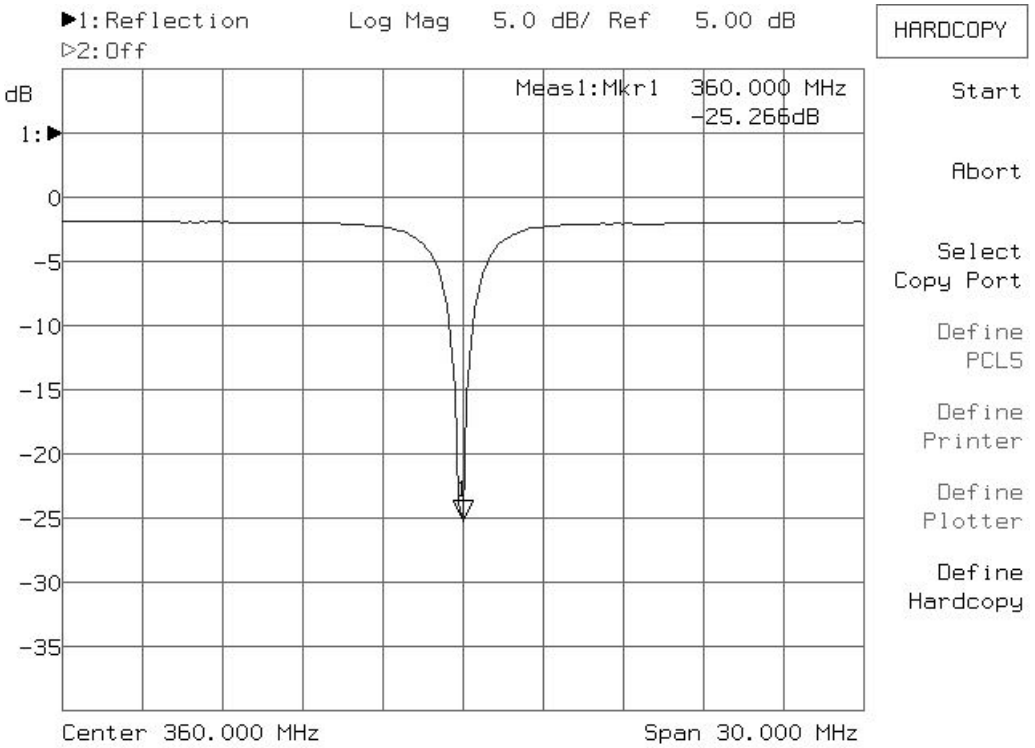

Figure 3.1.8.: Wobbling curve during probe tuning using the network analyzer for the ^{1}H-channel

This first tuning measurement is preliminary after then we consider the probe is connected with the other parts of the spectrometer, the circuit configuration will change and the probe could be tuned further using the voltage ratio[1] (reflection/incident) which is measured with the directional coupler. A directional coupler is an asymmetric power divider with four ports as shown in the block diagram Figure 3.1.3 for both channels of the spectrometer. It splits the incident rf signal to a small part which goes to the scope as incident pulse and the other part to the sender (HF) amplifier and it does the same for the reflection signal. For a well tuned probe, the rf reflected power should not exceed 1% of the rf incident power. Figure 3.1.9 shows (a) incident pulse and (b) reflection pulse with 2 μsec pulse width from the ^{1}H-channel directional coupler.

[1]The power ratio will be the square of the voltage ratio

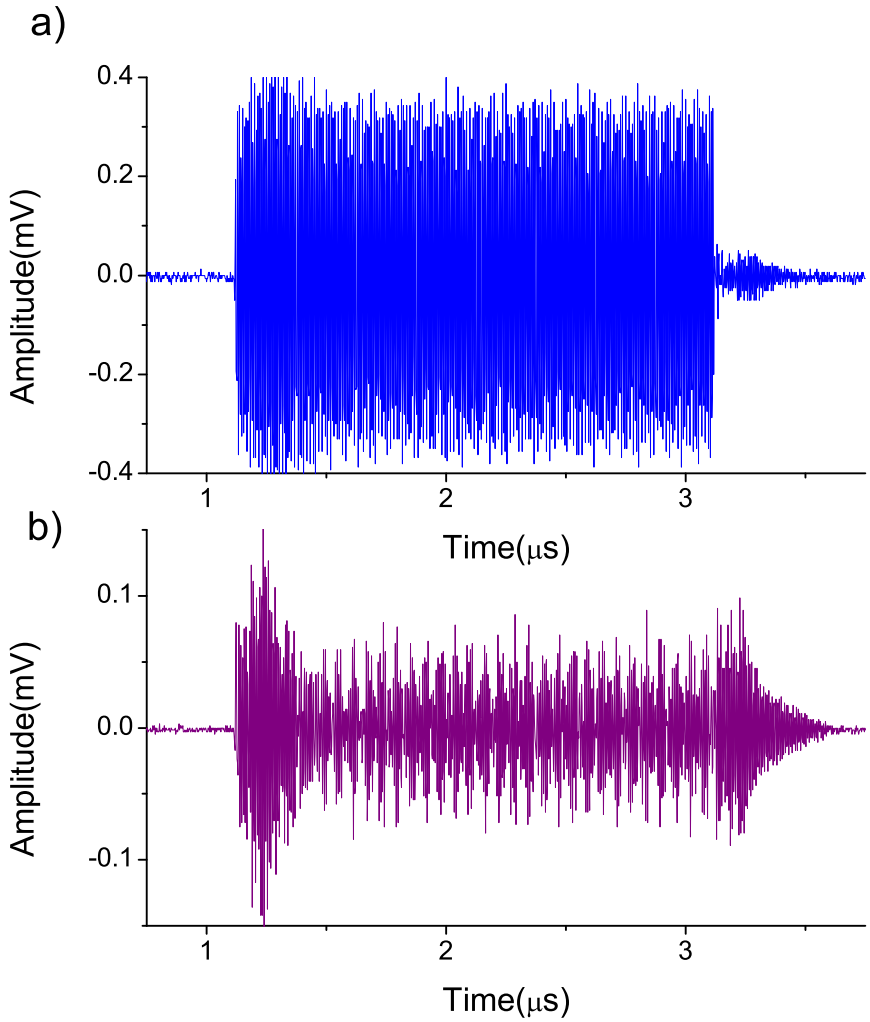

Figure 3.1.9.: Tuning the ^{1}H-channel using the directional coupler : 2 μsec pulse for a) incident pulse and b) reflected pulse

The reflected power decreases when the probe is tuned in the right direction. If the ratio is one that means all the power is reflected and the circuits should be followed step by step. The coupling factor (C.F.) of the directional coupler is given by the equation

$$C.F. = -10log\frac{P_3}{P_1}, \tag{3.1.9}$$

where:

P_1 : Input power, P_3 : coupled power(from the incident part).

As an example we calculate the coupling factor (C.F.) for the directional coupler in the X-channel (P_3= 6.8 dBm, P_1 =40.65 dBm)

$$C.F. = P_3(dBm) - P_1(dBm) = 33.85. \tag{3.1.10}$$

3.1.7. Shimming the 360 MHz spectrometer

The superconducting magnet generates a magnetic field $B_\circ$, which is equivalent to Larmor frequency in high frequency range. This high value makes it hard using only the superconducting magnet to limit the variation in the magnetic field across the sample to 10^{-9} . Corrections to the field homogeneity $\Delta B_\circ$ are made by using the shim coils[2], shimming means adjusting the resolution of the signal by optimizing the homogeneity of the magnetic field so that every part in the sample experiences the same field. These inhomogeneities caused by different aspects starting from the magnet installation and design through variations in the thickness of the sample tube, sample permeability, and ferromagnetic materials around the magnet. Superconducting shim coils are set during installation of the magnet. Room temperature shim coils generate small magnetic fields for correcting gradient in all Cartesian coordinates. In the shimming unit of the 360 MHz spectrometer there are 34 different room temperature shim coils to optimized the magnetic field homogeneity. Passage of current through these coils adjust the inhomogeneity of $B_\circ$.

Before starting the shimming procedure the probe coil should be set in the middle of the superconducting coil. Axial shims for different orders named z0, z, z2, z3, ...,z7 correct inhomogeneities in the magnetic field along the z axis, where radial shims like x, y, ..., etc correct inhomogeneities in the xy plane. The z0 changes the field B_0. Figure 3.1.10 shows that the relative Larmor frequency variates linearly with z0 changes. However B_0 is changed slightly over the time due to the small resistance of the coil, which is known as normal magnets drift. A typical magnet drift for the 360 MHz spectrometer is 1.68 Hz per day as shown in Figure 3.1.11. Beside that B_0 exhibit variations due to magnetic materials moving near the magnet. Installing new magnets nearby shows shift in the B_0 field. Experiments are unlikely to be done during the filling process of liquid He or N, because the superconducting coils temperature is unstable and therefore the B_0 field.

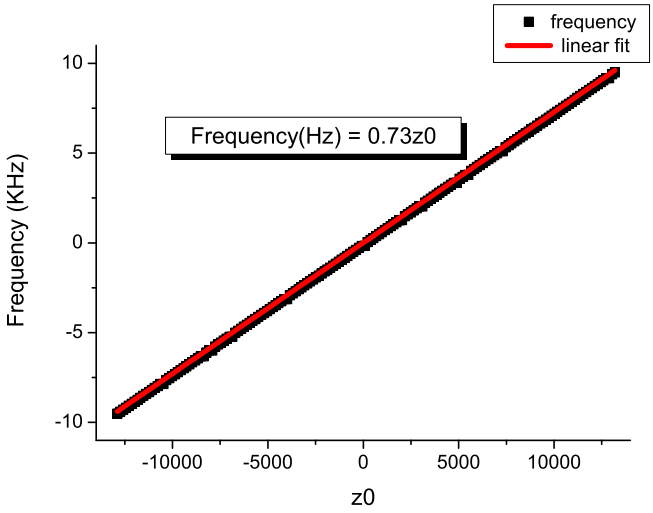

Figure 3.1.10.: Relative Larmor frequency versus z0 variation.

[2]The name 'shim' comes historically earlier where small piece of nonmagnetic metal was used to improved the homogeneity of the electromagnet by changing the distance between the halves of the magnet

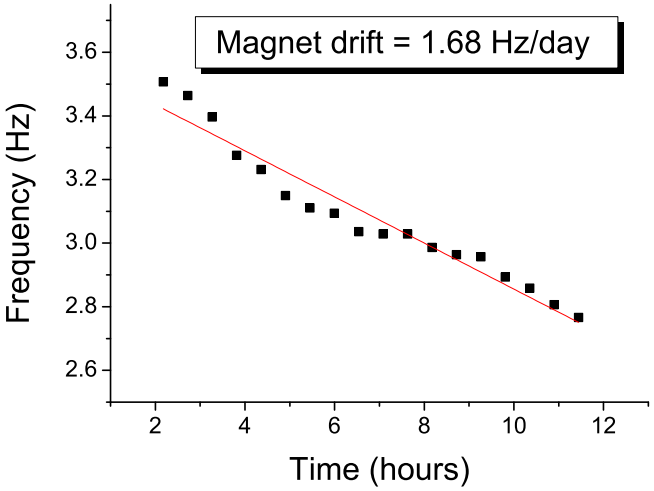

Figure 3.1.11.: Typical magnet drift for the 360 MHz spectrometer.

Important shim coils like z, z2 and z3, where the biggest effects in the line width occur, should be adjusted first. Passage of current adjust the inhomogeneity of B_0 field. Table (3.1.1) shows the mathematical expressions for the additional fields generated by the shims z[3], z2, z3, x, y. Figure 3.1.12 shows how these additional fields are represented according to the equations in Table (3.1.1). Configuration of current sources is varied over a wide range of number of channels, the 360 MHz spectrometer's shimming unit has a limit of ±32767 for gradient coil values, however the combined contribution from many gradients may exceed this limit and give message that values are out of range.

Order	Equation for field generated	Shim
0	1	z0
1	z	z
2	$z^2 - (x^2 + y^2)$	z2
3	$z[2z^2 - 3(x^2 + y^2)]$	z3
4	x	x
5	y	y

Table 3.1.1.: Mathematical representation of z0, z, z2, z3, x, y shims which are proportional with correction field $\Delta B_\circ$.

[3]z shim also called sometimes z1 shim but we use here the name z as in the shimming unit of the spectrometer

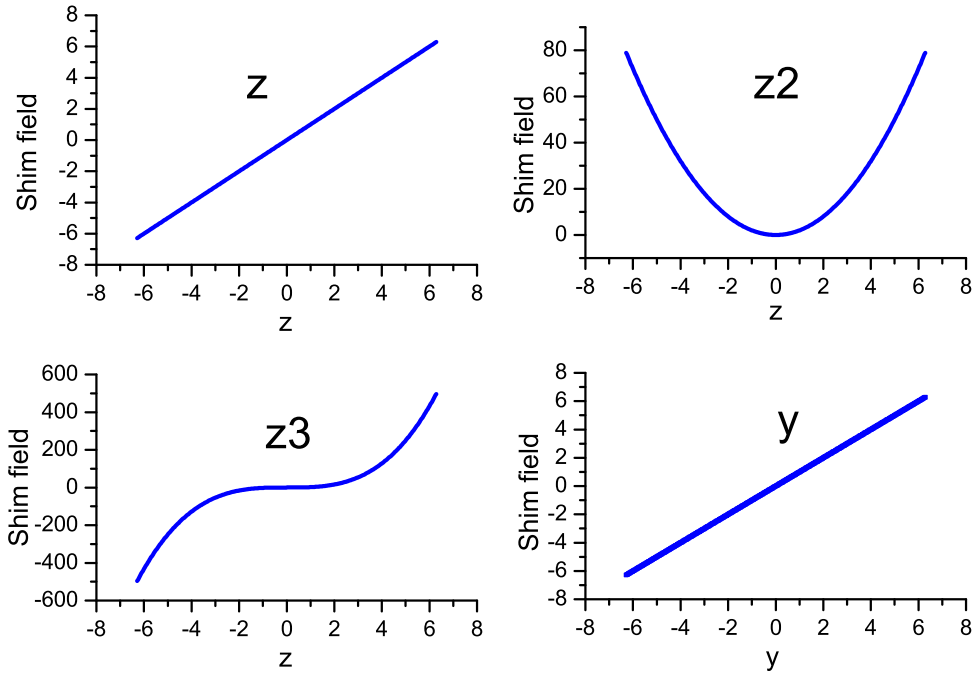

Figure 3.1.12.: The curves shows magnetic field corrections due to diffident shims variations: z1, z2, z3, y.

Shimming is performed in the 360 MHz spectrometer by optimizing the best line width of the ^{1}H signal. Shimming is time consuming procedure and many protocols can be used to achieve optimal results. First one may optimize z and z2 to get the narrowest line width. Then higher order like z can be optimized. Since shim coils are interacting with each others and lower orders contribute to higher orders, z and z2 should be optimized a gain after performing z3. In this sequential one can optimized other shim parameters. When all shim values are optimized, then the values are saved in text file and they can be set again using MacExp through RS-232 interface[85, 76, 86, 71, 87].

3.1.8. Noise reduction

Battle against noise is an essential part in most NMR experiments. Noise comes from the thermal motion of charged particle of the sample and thermal motion of electrons in the receiver coil. The noise and the NMR signal are amplified through different amplifiers in the circuit. In ^{13}C NMR experiments, the detected signal is very weak due to less natural abundance and lower gyromagnetic ratio. Comparison between the ^{1}H which has natural abundance 99.98% (with relative sensitivity of 1.0), and the ^{13}C which has 1.1% (with relative sensitivity of 1.6×10^{-2}), illustrates that during an NMR experiment, only about 1.1% of the carbon atoms in the sample are able to contribute to the signal. That causes the signal getting lost inside the noise. Many steps are used to increase the signal to noise ratio. Noise is often a limiting factor for the performance of a device or system. Depending on its source or its frequency bandwidth, noise can be classified into a number of categories.

Towards reduction of noise and obtaining a well defined NMR signal we will take into account categorizing noise, i.e. undesirable disturbance to NMR signal, into two essential

parts depending on its time characteristics:

3.1.8.1. Incoherent noise

The incoherent noise is independent of the NMR pulses so it occurs randomly and its value can not be predicted at any time. The thermal noise, also known as Johnson noise, is an incoherent noise which is frequency independent. Its power spectral density $\bar{V_n}$ is proportional to the absolute temperature with Eq. (3.1.11) so it is unavoidable at non-zero temperature[88].

$$\bar{V_n} = 2\sqrt{k_B T \Delta\nu R}, \tag{3.1.11}$$

where:

T≡ resistance absolute temperature (room temperature = 298 °K), $k_B \equiv$ Boltzmann constant, $R \equiv$ resistance of the noise source = 50 Ω and $\triangle\nu \equiv$ frequency bandwidth over the noise which is measured in Hz.

For a given bandwidth frequency for the preamplifier $\triangle f$ (500 MHz) the rms noise given with Eq. (3.1.12), can be calculated:

$$\bar{V_n} = 2\sqrt{1.38 \times 10^{-23}\, J/K \times 298\, K \times 500\, MHz \times 50\,\Omega} = 20.28\,\mu V \Rrightarrow -81\, dBm \tag{3.1.12}$$

A useful technique used to reduce thermal noise is signal averaging. Assuming that, at the output of the oscilloscope, the signal is a compound of NMR signal $S_{NMR}(t)$ and noise $S_{noise}(t)$ which are given by:

$$S(t) = S_{NMR}(t) + S_{noise}(t). \tag{3.1.13}$$

Running another identical NMR experiment, $S_{NMR}(t)$ will add coherently to give a total NMR signal $2S_{NMR}(t)$ S_t. The noise S_{noise} which supposed to be random with standard deviation σ_{noise} over all sampling points. The noise amplitude in the first experiment is given by the root mean square (rms) Eq. (3.1.17)

$$\sigma(1)_{noise} = \left\langle S^2_{noise}(1) \right\rangle^{1/2}, \tag{3.1.14}$$

on the assumption that the noise is stationary, its amount will be the same for the second experiments, then the sum will be:

$$\sigma_{noise}(1+2) = \left\langle (S_{noise}(1) + S_{noise}(2))^2 \right\rangle^{1/2}, \tag{3.1.15}$$

since the noise is uncorrelated between two experiments, the average term $\langle S_{noise}(1) S_{noise}(2) \rangle$ vanishes, Eq. (3.1.15) gives:

$$\sigma_{noise}(1+2) \cong \sqrt{2}\sigma_{noise}(1). \tag{3.1.16}$$

Extending this argument to N number of scans, we can decrease the noise by $\sqrt{N}$ given by Eq. (3.1.17):

$$\frac{S_t}{\sigma_t} = \sqrt{N}\frac{S_{NMR}}{\sigma_s} \tag{3.1.17}$$

Another useful technique affects the resolution or the signal to noise ratio (S/N) is apodization. It smooths the tail of the free induction decay (FID) signal to eliminate the sharp edge produced by the a rectangle function, goes through with multiplying the digitized FID by a mathematical function. Applying for example Gauss apodization results in clipping the tail of the spectrum where the signal is weakest and leave the early part unaffected[74, 76].

3.1.8.2. Coherent noise

This kind of noise is coherent with pulse sequences or receiving procedure. Such as impulse noise due to the transient nature of the NMR experiment where the sender is separated from the receiver through the duplexer which does not perform as an ideal barrier. Transient noise consists of relatively longer duration pulses compared to impulse noise. It could be also systematic noise such as the 50/60 Hz noise "hum" originates from the power supplies circuits[89, 82, 90].

Removal of the artifact during quadrature detection, where two signals 90°out of phase are sampled (M_x, M_y) is achieved through *phase cycling*. A Familiar method in NMR known as cyclops can be done by incrementing the rf pulse phase for four steps, every step with 90°. This will tilt the magnetization signals (M_x, M_y) in the different axises as explained in Table (3.1.2). The receiver phase is always in the same position relative to the magnetization. Since NMR signal change it is phase with the pulse phase, the data (real and imaginary) added and the artifact that do not follow this phase cycling will simply be canceled if the reviver phase is kept always the same. One should take care if the output cables are reversed, adding the signal will give zero.

Cycle counter	Phase of pulse	Receiver phase	M_x	M_y
0	+X	+X	+Y	+X
1	+Y	+X	-X	+Y
2	-X	+X	-Y	-X
3	-Y	+X	+X	-Y

Table 3.1.2.: Four-steps phase cycle

If an FID is displaced from the baseline by a constant amount then the spectrum will contain spurious resonance peaks around zero. *Removing this DC offset* is done by taking the value of last 10% points and subtracting this value from each point in the FID, which known as baseline correction[74].

Ground noise Ground noise can be characterized as coherent noise, for safety consideration the chassis or enclosure of an electric equipment should be grounded. Ground points should have well defined ground potential. In real systems the actual path taken by the ground has different impedances. This is causes a difference in potential between two physically separated ground points.

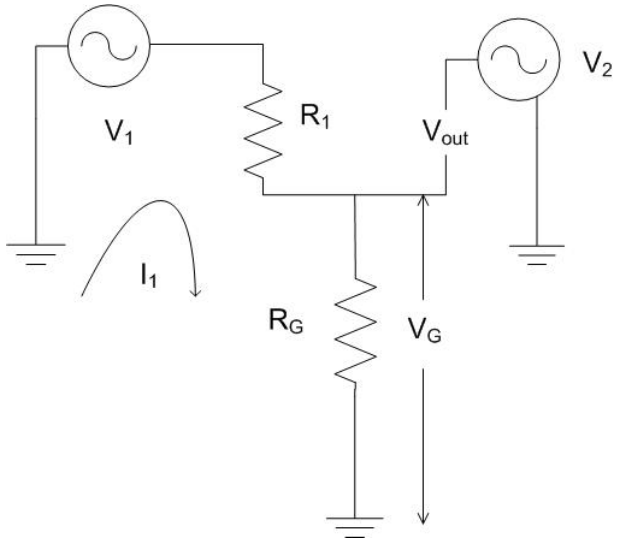

Figure 3.1.13.: A typical ground loop circuit diagram

In Figure 3.1.13 there are two circuits sharing common wire connection to the ground. If they share the ground at the same point, then (R_G=0). In other words if V_1 is isolated from V_2, then V_{out}=V_2.

In real circuits cables with different lengths have different resistances, assuming $R_G \neq 0$, a voltage drop from V_1 occurs, then, $V_G = R_G\ I_1$, V_G applied to the second circuit and added to the output voltage, which can be written by Eq. (3.1.18):

$$V_{out} = V_2 - V_G = V_2 - R_G(\frac{V_1}{R_G + R_1}). \tag{3.1.18}$$

Signal grounds are classified into three types as shown in Figure 3.1.14:

1. Single point grounds could be either parallel connections, also called separate ground systems which are preferred to avoid noise or series connections which are called common grounds and have the advantage of its wiring simplicity.

2. Multipoint grounds which is a good choice for high frequencies > 10 MHz to minimize the ground impedance.

3. Hybrid grounds, this are combination between single point grounds and multipoint grounds.

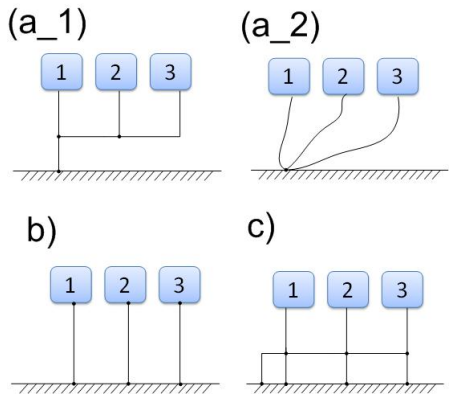

Figure 3.1.14.: Types of ground connections:(a_1) single point ground(common ground), (a_2) single point ground(separated ground), b) multipoint ground, c) hybrid ground

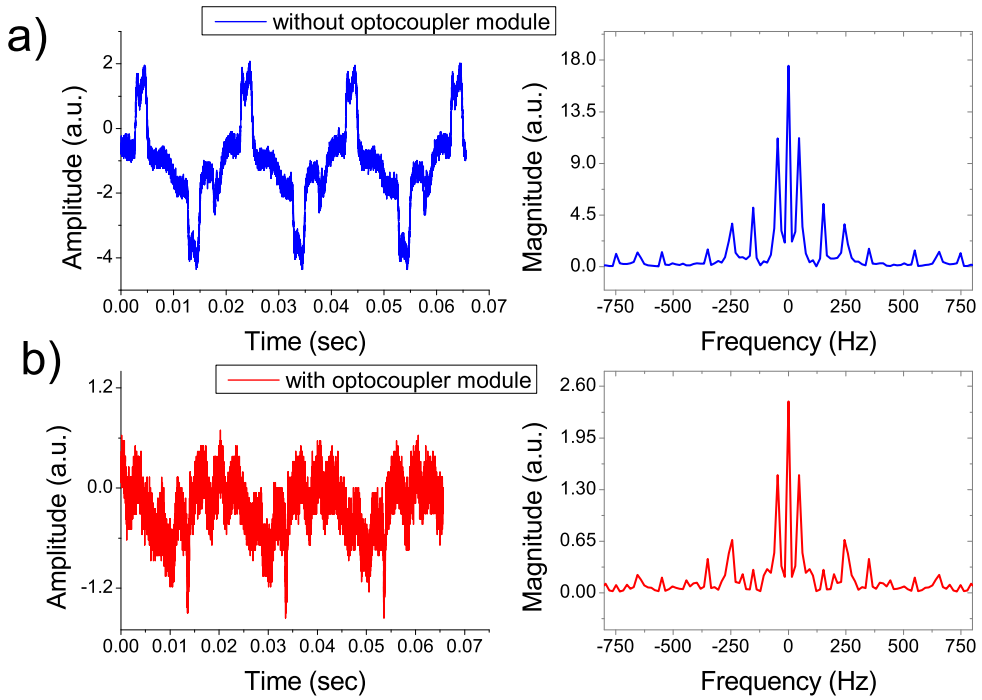

Figure 3.1.15.: A typical ground loops signal: a) left side is a time domain signal without using the optical coupler module and the right side shows its spectra , b) left side is a time domain signal with using the optical coupler module and the right side shows its spectra.

Switching all devices off, does not mean there is no source of noise active, as long as the AC cable is connected to the power supply there could be typical ground loop noise in the NMR circuits as shown in Figure 3.1.13 upper curves with blue color where the left part shows the time domain noise coupled with the 50 Hz and the right side shows its spectra. The main center peaks of the noise around 50 Hz and it is harmonic frequencies 100 Hz, 150 Hz ... etc. These ground loops are connecting through ground prongs. Removing this third connection, i.e. prongs, would be helpful only for diagnosis where is the problem

coming from, but this is not a safe solution in the long run. Connecting all sources at the same ground point is some times hard to achieve, where the devices are very far from each other. When the signal circuit is grounded at both end, the ground loop formed is susceptible to noise form magnetic field or different ground voltages, then these loops could be broken by using optical couplers.

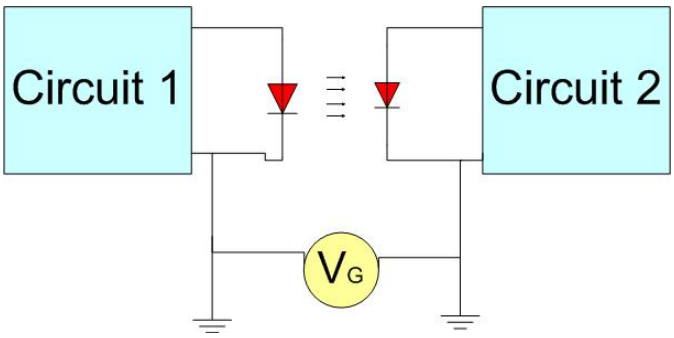

Figure 3.1.16.: Optical coupler circuit used for reducing ground loops noise

Optical couplers behave as electrical isolators and disconnect the ground connection from other ground loops because they transfer the signal as light as shown in the circuit diagram in Figure 3.1.16[91]. In the 360 MHz spectrometer as we mentioned in Section (3.1.2), the master clock is connected to the DDS and the Hameg synthesizer. The master clock has 16 outputs generates square wave with frequency of 10 MHz for each output. All outputs share the same ground. Ground loops are multiplied because of shared ground with other circuits. Connecting the optical coupler module (shown in Figure 3.1.17), which has four outputs (with separated ground) will contribute to reduce the 50 Hz noise with a factor of two in the lower part as in Figure 3.1.13 with red color in comparison with the upper part.

Figure 3.1.17.: Optical coupler module for the master clock

3.2. Sample preparation

3.2.1. Measurement of relaxation times T_1

In pulse NMR, nuclear spins are detected through their free induction decay (FID). To determine the maximum FID amplitude, which corresponds to a $\frac{\pi}{2}$ pulse, different pulse

lengths have been applied and the pulse length is plotted against the FID amplitude. This is known as a nutation experiment as shown in Figure 3.2.1. The analysis shows a $\frac{\pi}{2}$ pulse of 17.5 μs.

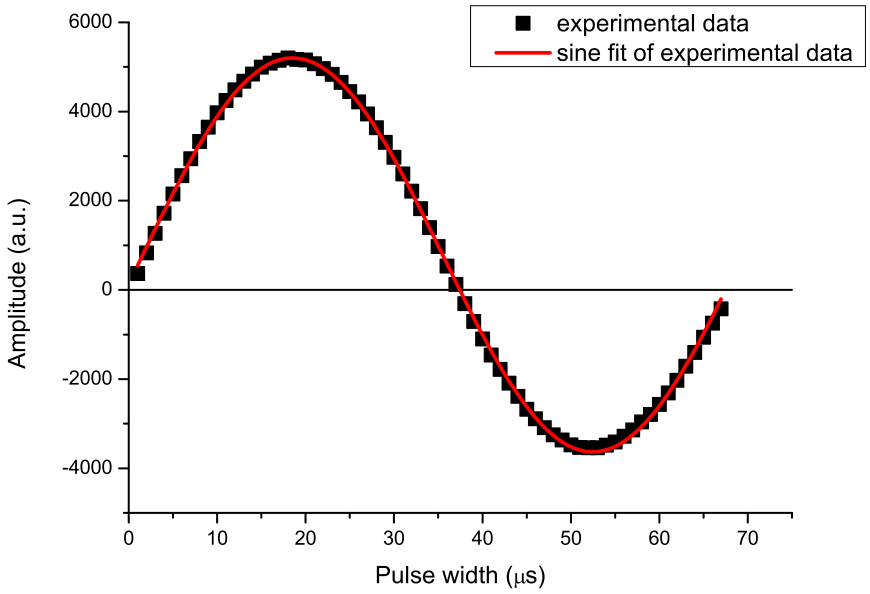

Figure 3.2.1.: Nutation experiment

The magnetic field strength is related to the pulse power as in Eq. (3.2.1)

$$B_1 \approx \sqrt{(3PQ/\nu_0 V)} \approx 3.7\sqrt{(PT_R/V)}, \tag{3.2.1}$$

where:

P : transmitter power in watt, Q : quality factor, ν_0 : frequency in MHz, V : coil volume in cm^3, T$_R$: ring-down coil time in μs[92].

3.2.2. Radiation damping

For strong NMR signals (high concentrated sample with higher gyromagnetic ratio), the strong signal induces a small rf current in the receiver coil. Because of the induction principle, another radio frequency field B$_{rad}$ is created, which is always of the opposite direction to B$_1$, known as radiation damping field.

If the magnetization rotation is induced by the coil through applied rf field, then the rotation is uniform given with the angular velocity:

$$\left(\frac{d\theta}{dt}\right)_{nut} = \gamma B_1 = \omega_1, \tag{3.2.2}$$

where θ is the angel between the magnetization and B$_1$ field.

On the other hand the angular velocity of radiation damping is not uniform, but depends on the sine function of θ given by:

$$\left(\frac{d\theta}{dt}\right)_{rad} = \gamma B_{rad} = -\frac{\sin(\theta)}{T_{rd}}, \tag{3.2.3}$$

where T_r is characteristic radiation damping time which is defined by Eq. (3.2.4) and the minus sign means the magnetization rotates in the opposite direction of the rotation induced by B_1field.

$$T_r = 1/(2\pi\eta\gamma Q M_0), \tag{3.2.4}$$

where: η is the filling factor,

Suppose we have an rf field due to rf pulse in $+x$-direction, the magnetization lies along $+y$-direction, B_{rad} lies along $-x$-direction. B_{rad} accelerates the decay of the NMR signal and broadens the resonance line. Thus the magnetic spin system is coupled to the coil, which is used for detection. Radiation damping grows with the net magnetization and the Q factor of the coil, so radiation damping is more relevant in high field magnet and relatively high Q factor NMR probes, where radiation damping rate is linearly proportional with the product QM_0 (see Eq. 3.2.2). Radiation damping produces a back-action field which tends to rotate the magnetization back to the equilibrium state[93, 94, 95, 96, 97].

The following experiments were done for different solutions to verify the radiation damping effect. In NMR experiments the bulk magnetization at thermal equilibrium is in the z direction. Applying a $\frac{\pi}{2}$ pulse, the bulk magnetization rotates from the z axis to the xy plane. The spins need time to return to thermal equilibrium which is called the recycle or repetition time. Usually this time is calculated to 1..5T_1. Inversion recovery method is used to measure T_1 for different concentration of D_2O/H_2O, where the pulse sequence is (π, τ, $\frac{\pi}{2}$). The delay τ is varied to calculate T_1. Figure 3.2.2 shows how the relaxation rates $1/T_1$ are change depending on the ratios D_2O/H_2O. It shows a linear increment with increasing H_2O concentration. These results are matched well with the results of Anderson *et al.* which are explained depending on the mutual dipole interaction among the nuclei. [98, 76]

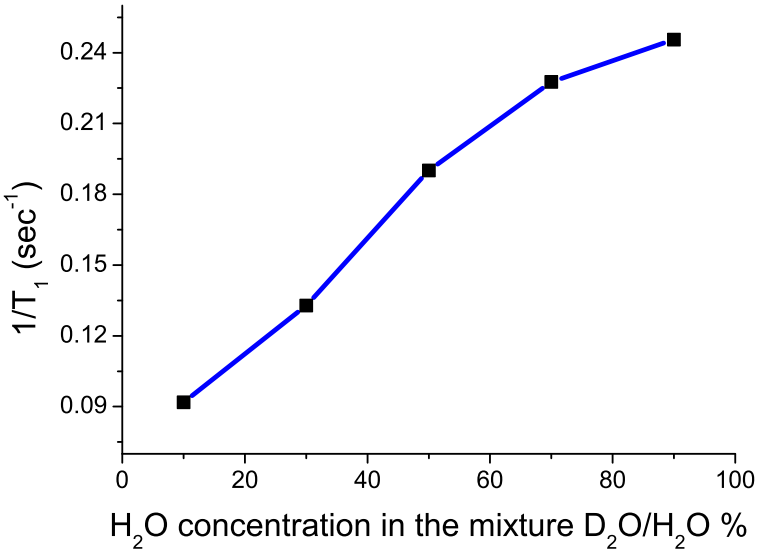

Figure 3.2.2.: Relaxation rate $1/T_1$ versus the relative volume concentration of the mixture D_2O/H_2O.

In the case of strong radiation damping, that means T_r is too short ($T_r < T_2^*$), difficulties in defining the exact value of $\frac{\pi}{2}$ pulse width arises because the nutation shape

deviates from the normal sinusoidal shape[99]. Figure 3.2.3 shows how the nutation curves converges towards the normal sinusoidal function when the ratios between the mixture D_2O/H_2O volumes increase. Increasing the ratio of D_2O means decreasing of the proton concentration consequently decreasing of the signal but fortunately decreasing the rate of radiation damping. In Figure 3.2.3 at ratios 30% and 40% of D_2O there is no strong effect of radiation damping where they fit the sinusoidal curve compared to the 10% and 20% ratios.

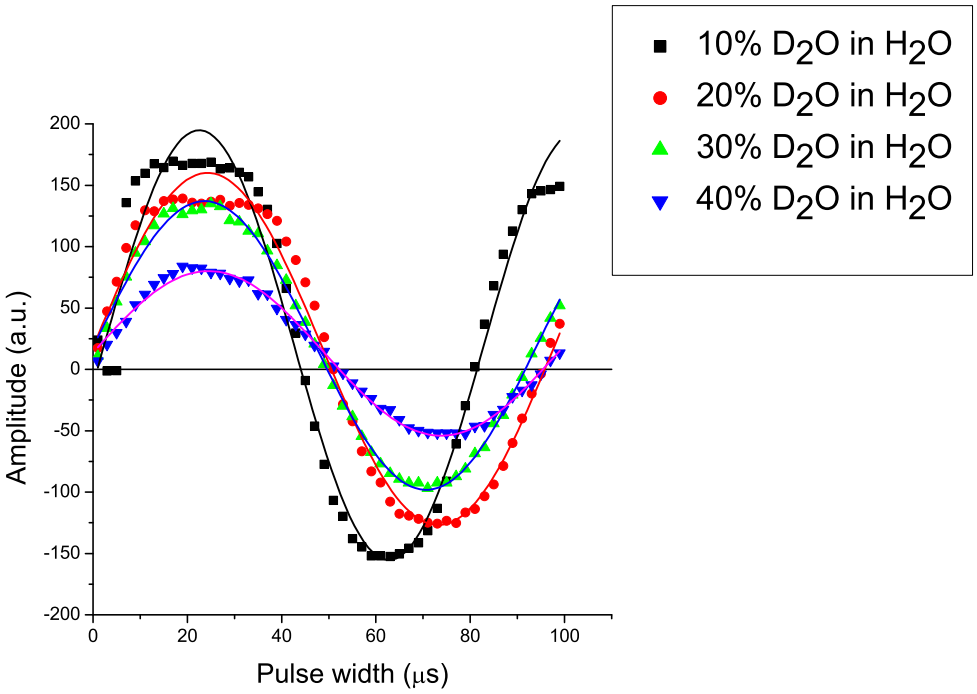

Figure 3.2.3.: Curves shows sine fit of nutation experiments for different mixtures of (D_2O/H_2O) and symbols are experimental data.

3.2.3. Pure water

In pure water there are two types of interactions, first the intramolecular interaction which is represented by dipolar interaction with other protons in the same molecule. Second type of interaction is the intermolecular interaction caused by protons in neighboring water molecules. These interactions fluctuate as water molecules diffuse in translation and rotational motion. Paramagnetic Impurities molecules in water solution act as relaxation centers. The dipolar interaction between the proton and the impurity ionic moment is modulated by the relative motion of water and the ions. Adding paramagnetic ions such as $CuSO_4$ is useful to decrease the recycle time for H_2O. In this experiment, a solution $H_2O/CuSO_4$ with a concentration of 5 g/100 mL is added to H_2O with different volume ratios. The relaxation time T_1 is inversely proportion with the $H_2O/CuSO_4$ volume ratio in the sample respectively the $CuSO_4$ concentration. Figure 3.2.4 shows how the relaxation rates change with the $CuSO_4$ concentration[75].

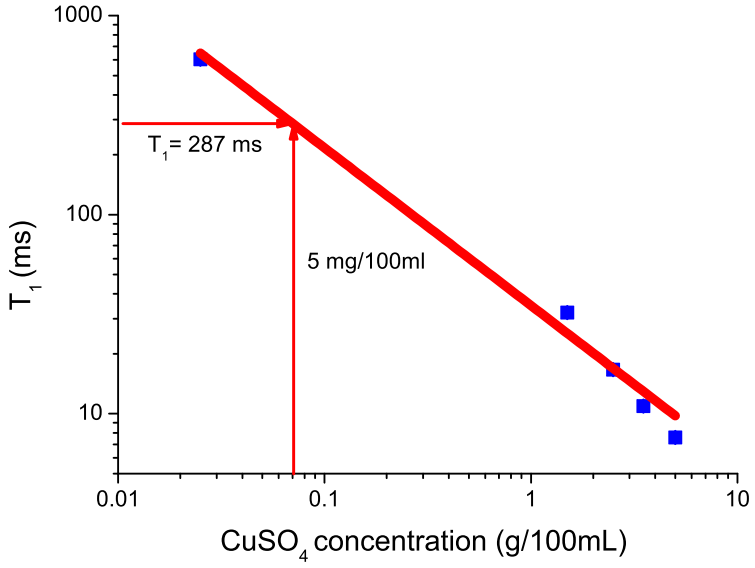

Figure 3.2.4.: Relaxation time T_1 plotted versus concentration of $CuSO_4$ in H_2O

3.2.4. Tune up sequences and pulse parameters optimization

In addition to the probe tuning procedure in Section (3.1.6) further adjustment for the pulse parameters before applying the multiple pulse sequences is useful to minimize the effect of pulse error and ensure that parameters are correctly set. An experimental verification by Burum *et. al.* shows that the so called "tune-up" pulse sequences are useful for minimizing phase transients[100]. Since it is hard to define the flip angles $\pi, \pi/2$ in the nutation experiment accurately as in Section(3.2.1), identical $\pi, \pi/2$ pulse sequences are used. The sequences are $(\pi_x - \tau - \pi_x - \tau)$ for π and $(\pi/2_x - \tau - \pi/2_x - \tau)$ for $\pi/2$.

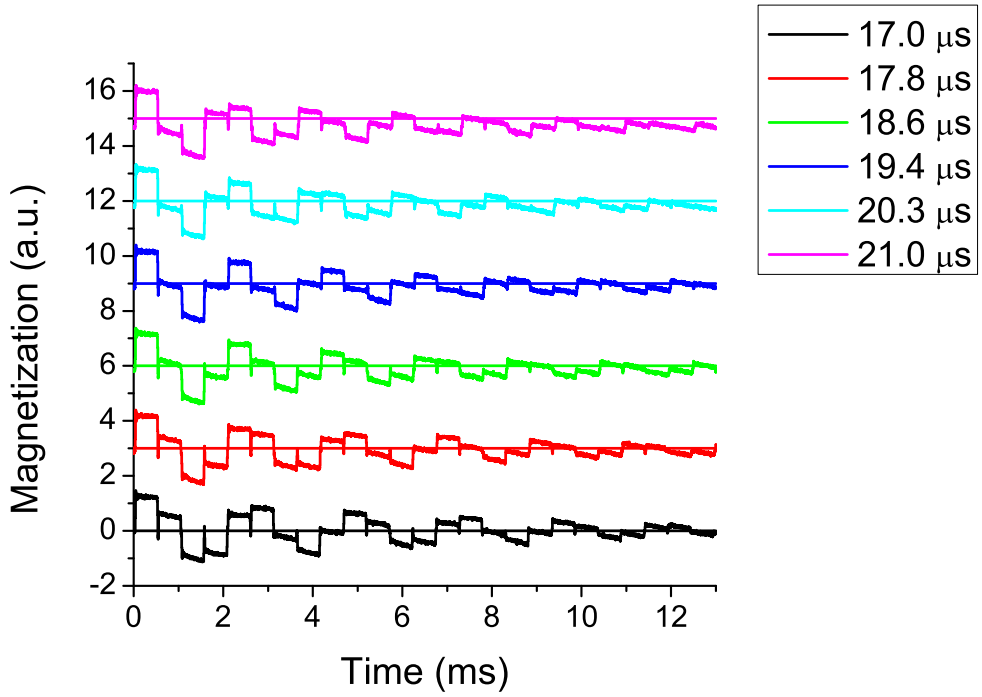

Figure 3.2.5.: Typical response from identical $\pi/2$ pulse sequences (24 pulses) for different values of pulse durations

Measuring the magnetization after each pulse for identical $\pi/2$ pulses shows a typical response as in Figure 3.2.5. The first $\pi/2$ pulse rotates the magnetization from the z direction to the xy plane (through horizontal lines above the base line for each pulse length the maximum magnetization is measured), a second $\pi/2$ returns the magnetization again to the z (measure zero for the transverse magnetization i.e. the base line for each pulse width). According to Figure 3.2.5 the optimal $\pi/2$ value is 19.4 μs, which shows symmetric shape around the baseline. As a result of the B_1 field inhomogeneity the magnetization values decays to minimum after 24 pulses with interpulse delay $\tau = 500$ μs. Similar optimization is done varying π values and the minimum value of the magnetization represents the optimized value of π pulse.

The optimal responses of identical pulses $\pi, \pi/2$ sequences are shown in Figure 3.2.6, for both $\pi, \pi/2$ sequentially, where the optimal pulse lengths are obtained.

Here are three tune-up sequences used for different purposes and their results correspond to each sequence:

1. Flip flip flop with x prepulse sequence $[\pi/2_x - \tau - (\pi/2_x - \tau - \pi/2_x - \tau - \pi_{-x} - \tau)]$ is used to adjust the relative phase of [x] and [-x] pulses. A typical response is shown in Figure 3.2.7

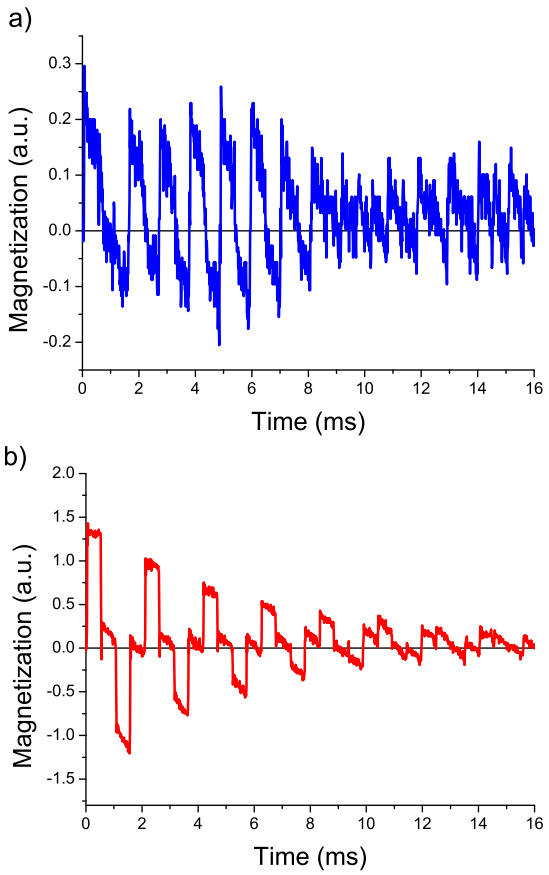

Figure 3.2.6.: Typical response of identical pulses $\pi, \pi/2$ sequences

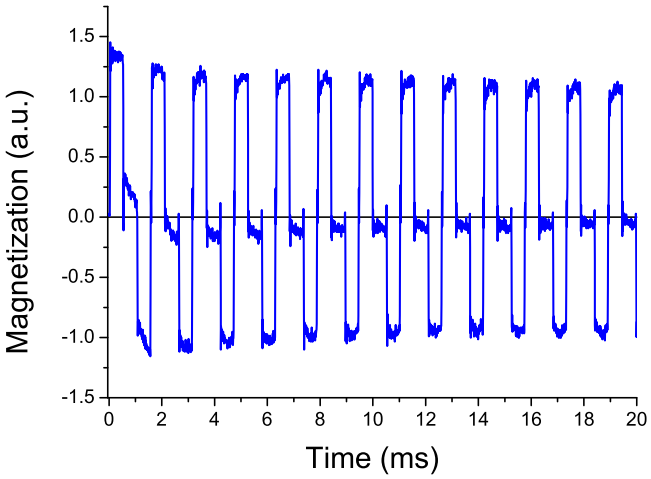

Figure 3.2.7.: Typical response of Flip flip flop sequence with prepulse

2. Flip flip flop without prepulse sequence $(\pi/2_x - \tau - \pi/2_x - \tau - \pi_{-x} - \tau)$ is used to eliminate asymmetric phase transition. A typical response is plotted in Figure 3.2.8

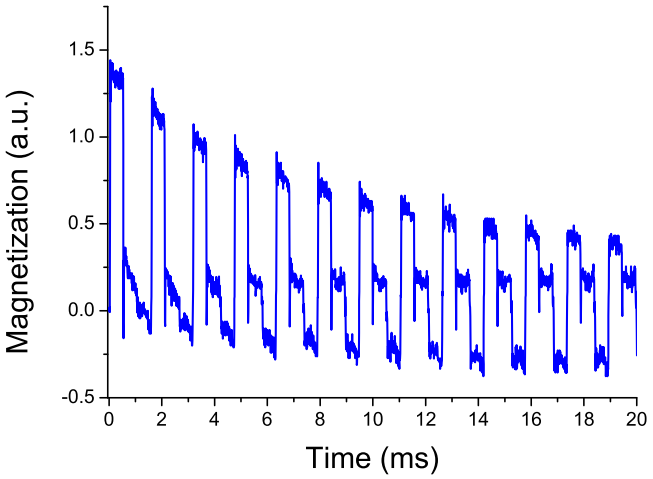

Figure 3.2.8.: Typical response of Flip flip flop sequence without prepulse

3. Flip flop sequence $(\pi/2_x - \tau - \pi/2_{-x} - \tau)$ is used to verify the tuning of the probe circuit. A typical response is shown in Figure 3.2.9

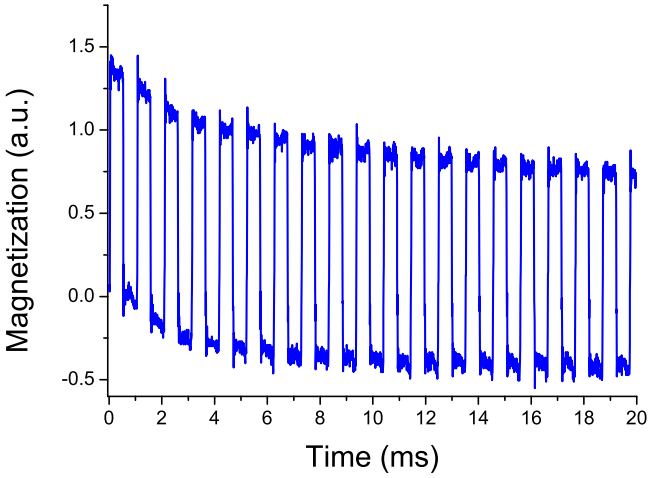

Figure 3.2.9.: Typical response of Flip flop sequence

3.2.5. Pulse visualization

A useful way to test the pulse sequences, in multiple pulse NMR experiments before running experiments, is to see the pulses applied to the probe. This test can be done by measuring the pulses through the demodulator, to verify if the pulses are identical to the intended pulse sequences. Figure 3.2.10 shows pulse sequences for different DD sequences whereas pulses are measured after the modulator using an external DDS as a reference to the demodulator to see the phase differences[4]. The detected pulse sequences are measured using phase sensitive detection method, i.e. two channels outputs which represent different phases of the pulses in red and blue as plotted in Fig. 3.2.10. The first

[4]The demodulator and modulator used the same DDS for the transmitting and receiving signals. If we want to see all phases we have to use an external frequency source, e.g. another DDS, then the change in the phase will not depends on the external source.

$\pi/2$ pulse in each sequence does not belong to the DD sequence, it is only prepares the initial condition for the DD sequence.

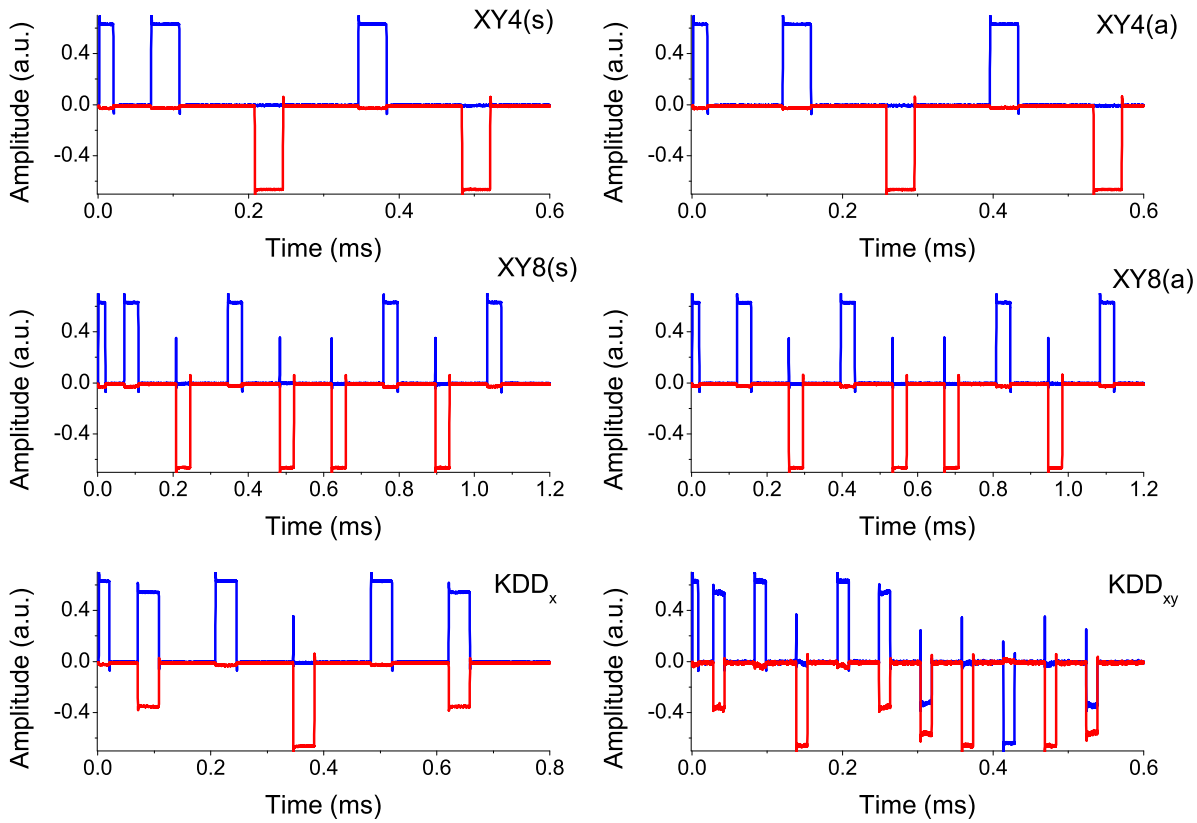

Figure 3.2.10.: Pulse sequences time line visualization for different DD sequences through the demodulator. The first cycle is shown for each sequence, in addition to the $\pi/2$ pulse, except for the KDD sequence where only half of the first cycle is shown. The second half of the cycle is similar to the first half in the KDD sequence . The blue pulse is the X component and Y component is the red pulse, the phase is calculated as $\tan^{-1}\left(\frac{Y}{X}\right)$.

The phase sensitive receivers aren't usually set to exactly 90° phase from each other. To measure the phase difference of our receiver precisely, an artificial signal is used, and the frequency difference from the reviver is detected. Figure 3.2.11 shows the measured spectra before phase calibration with a phase error 5%. Imperfect phases lead to ghosts "unwanted signals folded in the other region of the spectrum". The phase error effect can be defined as the ratio between the real and ghost peak amplitudes. The phase error is reduced to 1% by changing the cable length as shown in the inset of Fig. 3.2.11.

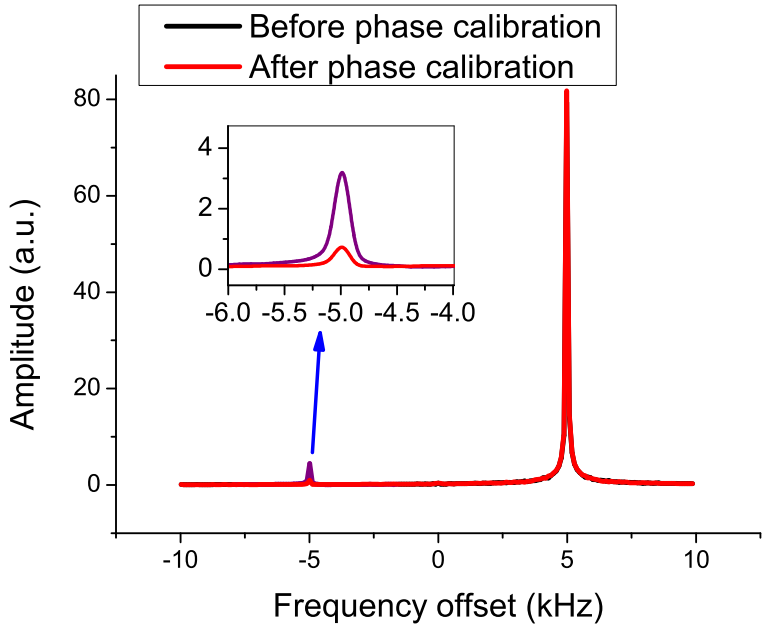

Figure 3.2.11.: Experimental phase calibration for a quadrature NMR receiver, the ghost peak has the same frequency of the real peak but with negative sign. The inset zooms the section to compare between the ghost peak before (black) and after calibration (red).

4. Dynamical decoupling

In this chapter we will describe general types of decoherence. Hence noise causes decoherence, we will then discuss the source of noise in our system. Next we address the DD sequences and how they can be designed to fight decoherence. Then we investigate the influence of pulse error on the effect of DD. Then we talk about a constructed experimental setup to introduce a modulation field to engineer the environment. Under these new environmental conditions we discuss the effect of this modulation field under a DD sequence. To complete the picture we give a theoretical analysis by average Hamiltonian theory for our experimental investigation under the influence of pulse errors.

4.1. Fighting against decoherence

Quantum computation on real quantum processors may be influenced by two sources: internal and external imperfections. Internal imperfections are imperfections due to "hardware imperfections", such as imperfections in the setting of the initial state, gate operations and/or final measurements. Uncontrollable interactions cause the magnetization to decay. Decoherence, can be defined as uncontrollable interactions with environmental degree of freedom. These uncontrollable interactions lead to a deviation between experiments and the ideal performance which is described by a unitary operator. There are fundamental limits of the experimental strategy against decoherence or system isolation that can be achieved to some degree of precision. External impact such as cosmic rays or the gravitational force which may changes the state of a qubit, are out of our control because it is hard to avoid their effects by shielding but some external impacts like the temperature are under control. Another experimental consideration is the amount of the power deposited in the system which often must be kept small to avoid heating effect on the sample[1] or damage the probe [66]. We can distinguish between four kinds of decoherence concerning the type of the coupling between the system and the environment [5, 101, 15, 30]

1. Total decoherence: this is a general case for decoherence where the coupling operator between the system and the environment has no restrictions.

2. Independent decoherence: here the coupling operator acts on individual qubits.

3. Collective decoherence: this process is called also collective dephasing, because the mutual phases between all qubits are destroyed, so the coupling operator acts simultaneous on all qubits.

[1] Liquid NMR samples are always subjected to evaporation, this can be avoided by well sealing the NMR tube, e.g., flame the top of the glass tube.

4. Cluster decoherence: in this case clusters of qubits decohere collectively and the different clusters decay independently.

A simple explanation to decoherence in liquid NMR systems can be given through relaxation times. The spin-lattice time T_1 is relevant to the energy dissipation between the system and its surrounding environment, also called the longitudinal relaxation time because it reduces the longitudinal magnetization. On the other hand the spin-spin relaxation time T_2, the phase damping time, is limited in liquid NMR systems by T_1. T_2 is also named the transversal relaxation times because it reduces the transversal magnetization [30, 10].

4.2. Our system and noise sources

Our experimental system is an ensemble of non-interacting spins 1/2. They consist of the protons of a water sample to which we added 5 mg/100 ml $CuSO_4$ to reduce the longitudinal relaxation time T_1. Figure 4.2.1 shows a typical experimental result of the inversion recovery pulse sequence $\pi_{(X)} - \tau - \pi/2_{(X)} - (t_{acqu})$ [74]. The magnetization M_0 is inverted with a π pulse, then during a time τ it allowed to relax along $+z$-axis. Then the magnetization is measured by applying a $\pi/2$ pulse. T_1 is determined by fitting the magnetization curve to

$$M_z(t) = M_0(1 - 2\exp(-\tau/T_1)). \tag{4.2.1}$$

The horizontal axis (Figure 4.2.1) represents the increment in the time τ between the pulses where the vertical axis represents the measured values of the magnetization by applying $\pi/2$ pulses each time. The experimental repetition time was 5 s, which is large enough compared with T_1.

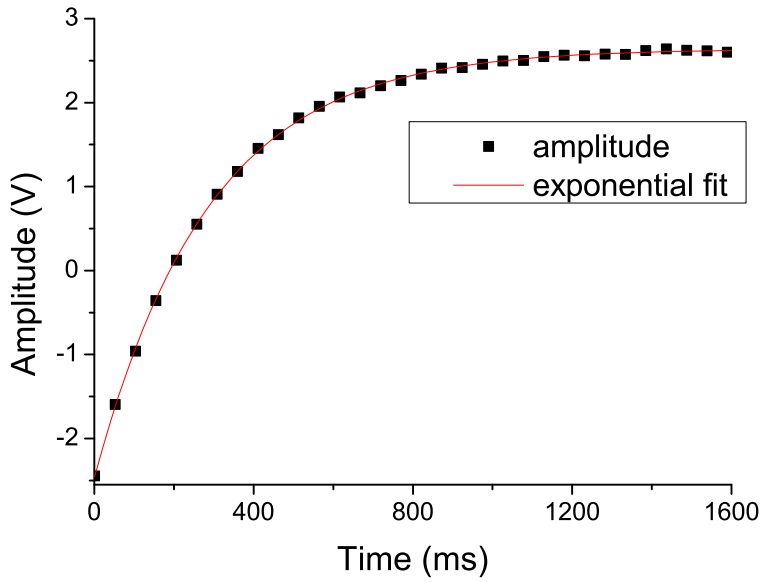

Figure 4.2.1.: Magnetization growth of the ^{1}H spin system after inversion recovery pulse sequence to determine the longitudinal relaxation time T_1

The longitudinal relaxation time T_1 in this case was 287 ms. As previously mentioned the addition of $CuSO_4$ results in a faster repetition times and shorter overall duration of the experiments, to run the DD experiment. The sample was placed in a static magnetic field along the z-direction and its Hamiltonian is

$$\mathcal{H}_s = \omega_s S_z, \tag{4.2.2}$$

where ω_s is the Zeeman frequency and S_z is the system spin operator along the z axis. Firstly the inhomogeneities of the static field correspond to a static perturbation, and molecular motion makes this perturbation time-dependent on a time scale that is slow compared with the delays between the DD pulses used in our experiments. This condition makes it possible to refocus this perturbation very effectively.

The second major source of noise is the fluctuating dipole-dipole interaction, whose correlation time is the molecular reorientation time ($\approx$ 35 fs), much faster than any conceivable control fields for nuclear spins and therefore not amenable to DD. On the other hand, these fluctuations are so fast that their average effect on the system is relatively small [102].

The experiments discussed in this chapter were performed on a home-built NMR spectrometer on the H-channel with a ^{1}H resonance frequency of 360 MHz (see the third chapter for the spectrometer configurations). To cancel the normal drift of the superconducting magnet and other abnormal effects, the transmitter frequency is calibrated. All experiments were performed on resonance unless otherwise stated. The radio frequency field strength was $2\pi \cdot 13.3$ kHz, which corresponds to a $\pi-$pulse duration of 37.5 µs. An initial state $\propto I_x$ or I_y was prepared by rotating the I_z equilibrium state with a resonant $\pi/2$ pulse.

4.3. How to construct a robust DD sequence?

DD sequences consist of repetitive trains of π-pulses. Figure 4.3.1 shows a schematic representation of a general DD pulse sequence. Errors in calibration of the pulse length make the implementations different from expected. Our goal is to implement unitary transformations, avoiding decoherence. The DD pulses are applied to the qubits to cancel or minimize errors by averaging them out. The delays between the pulses and their phases are important parameters for improving the performance of the DD sequences [69, 70, 103, 104, 21, 67, 22, 23].

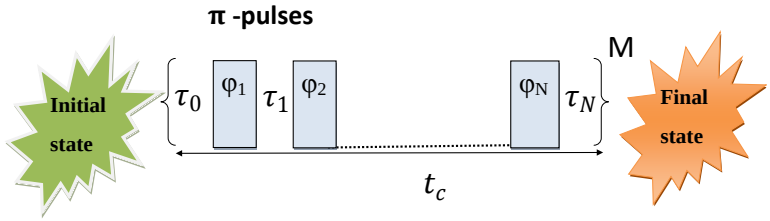

Figure 4.3.1.: Schematic representation of a general DD pulse sequence. One cycle contains N pulses and the cycle is repeated M times. The light blue squares are π pulses and the cycle time is t_c.

In particular the relative phases, which correspond to the directions of the rotation axes, are important for making the sequences robust against pulse imperfections and unwanted environmental interactions [40, 36, 42].

In experimental DD sequences, the nonidealness in implementing unitary transformations is either from flip angle errors and/or offset errors. In order to construct a robust DD sequence there are different ways: [66]

1. Improving the performance of pulses inside the DD sequence: this is can be done by using composite pulses which are robust against rf offset errors or pulse width errors. Another approach is to implement shaped pulses. In Ref. [105] the aim of the work was to study the performance of different shaped pulses to implement them in DD experiments [106]. In the previous study (i.e. Ref. [105]) the shaped pulses were divided into two parts composite shaped pulses and continuous shaped pulses. Because shaped pulses are often quite long, the effect of decoherence is dramatically stronger. These results in Ref. [105] were not conclusive because in that particular experiment radiation damping effect was not compensated. The effect of the radiation damping precludes determining the π pulse value when performing the nutation experiment. Recently Grace *et al.* showed that it is possible to improve the control of QIP by optimizing pulses when combining two criteria: the decoupling pulse criteria and the optimal control theory [107].

2. Making the DD sequence robust itself: this can be done either by optimizing the phases of the pulses by using different rotations such as the KDD sequence instead of the identical rotations axes like the CPMG sequence, or by variation of the delays between the pulses to be unequal. The non-equidistant pulse sequence was firstly proposed by Uhrig, Uhrig dynamical decoupling (UDD) sequence [23]. It worth noting that this variation between pulses can also be randomly or hybrid as suggested by Ref. [108] [60, 66, 30, 107]. Another approach for construction the DD sequences can be by numerical optimization based on genetic algorithm. Genetic algorithm is an approach for optimization and solving problems based on the natural evolution [109].

4.4. Initial experiments[2]

We start making comparison between two dynamical decoupling sequences CPMG and UDD. Both of them have identical rotation axes. The UDD sequence was first discovered by Uhrig for a pure dephasing spin-boson model, describing a spin 1/2 particle (two level system) interacting with an environment of large reservoir of bosonic field modes [110, 23]. The pulse timing in the sequence is governed by

$$\tau_j = t_c \sin^2\left(\frac{\pi j}{2(N+1)}\right), \tag{4.4.1}$$

where N is the UDD order which defines the number of pulses per one cycle, j takes the numbers 1,2,...,N, t_c is the cycle time.

It is obvious from Eq. (4.4.1) that UDD2 coincides with CPMG. In order to have different conditions for the environment, we incremented z1 (shim) values from -2739 to 4390 with 325 steps, this increment changes the field inhomogeneity. The line-width is dominated by field inhomogeneity, thus the line-width values can be a good measurement for the field inhomogeneity. The line-width values are obtained by measuring full width at half-height (abbreviated: FWHM) from the Fourier transform of the time domain signal.

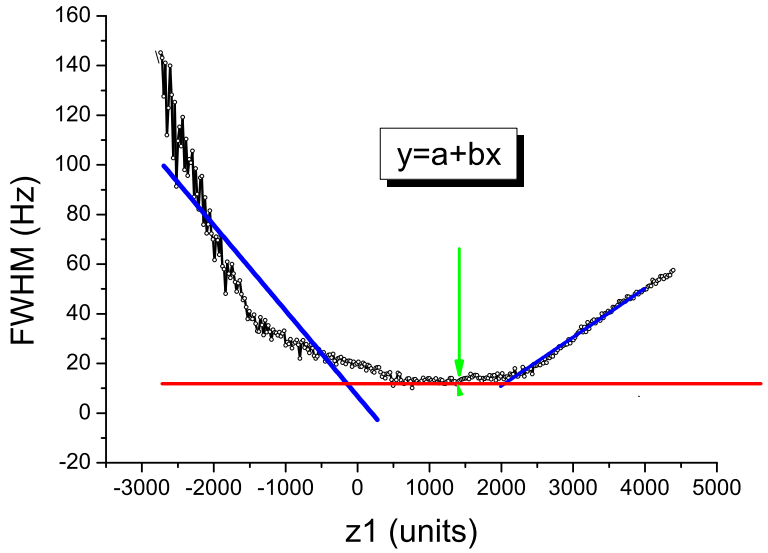

Figure 4.4.1.: The line-width (static field inhomogeneity) changes versus gradient strength values (z1). The black curves are experimental data while the blue lines are the calculated data.

Figure 4.4.1 shows the change of the z1 (negative and positive values) versus the FWHM values. We measured the slopes of the tangent of the curves (black) to define the change in the inhomogeneity. For instance the minimum value (shown with the green arrow in Fig. 4.4.1 @ z1=1390) represent the highest homogeneity of the magnetic field along z

[2]These initial experiments were done before the described optimization procedures (i.e. the tune-up sequence, shorten $T_1$by adding $CuSo_4$, the Pulse visualization)

axis. Table 4.4.1 gives the calculated slopes values and their intercepted values fitted to Eq. 4.4.2.

$$y = a + bx, \tag{4.4.2}$$

where: y≡ FWHM, x≡ z1 values, a≡ intercept from the y axis, b≡ slope.

	Intercept	Slope
Symbol	a	b
Line (left side)	6.8	-0.034
Line (right side)	-28.3	0.020

Table 4.4.1.: Slope calculations according to z1 changes versus line-width values

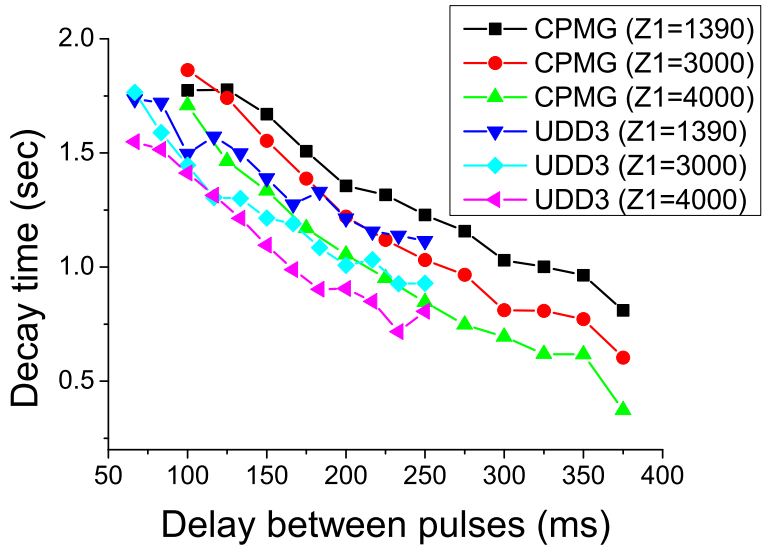

Figure 4.4.2.: Decay times comparison between CPMG and UDD3 under different conditions of field inhomogeneity (z1)

Figure 4.4.2 shows a comparison between the UDD pulse sequence to the third order (UDD3) and CPMG pulse sequence. Changes of z1 values cause a drift in the decay curves for different delays between pulses. However the CPMG sequence still outperforms the UDD3 sequence. The UDD sequence performance is strongly environmental spectral density dependent. As an example, experimental studies of the UDD sequence in a model atomic system shows that UDD sequence can dramatically outperform CPMG sequence in the presence of noise with an ohmic system and sharp cut-off [111, 34]. This is in good agreement that the UDD sequence cannot outperform the CPMG sequence in a systems with a soft cut-off frequency [36].

4.5. FID and Hahn echo sequence

Spin echo was discovered first by Erwin Hahn when two rf pulses are applied at a maximum rf field B_1 ($\pi/2$ pulses) separated by time intervals τ [112]. The physics behind the

experiment was explained in Hahn's famous paper in 1950 [31]. The pattern of the echo is always symmetric regardless of the spacing between the pulses. Refocusing is an important principle related with spin echo. The refocusing causes the phase differences of all spin vectors (with respect to the initial orientation established by the first pulse) to canceled effectively at the time where the echo is maximum. . The echo can never repeat again without applying another pulse. Figure 4.5.1 shows the Hahn echo pulse sequence applied, the experimental data shows the magnetization amplitude (black on y-axis and red on x-axis) after the $\pi/2$ pulse (blue rectangle above) and the π-pulse (green rectangle above). The second small echo, marked with the blue arrow in Fig. 4.5.1 at the end of the time line, is possibly related to the radiation damping effect. This can be explained as follows. Radiation damping acts as a new "pulse" after the π pulse and causes this second small echo.

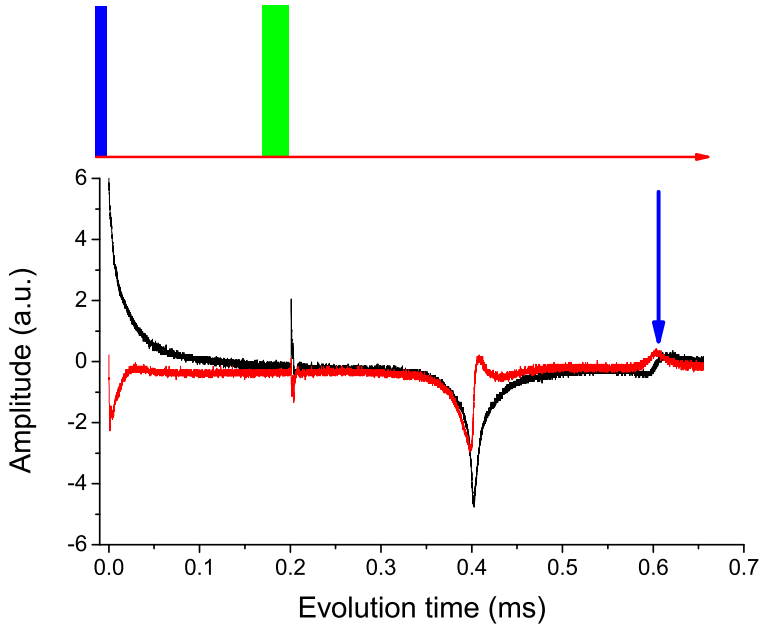

Figure 4.5.1.: Hahn echo experiment and the pulse sequence. The second echo at the end of the time evolution is induced by the radiation damping effect.

The free evolution decay of the transversal magnetization of our system has a decay time of 2.9 ms (FID). A simple Hahn-echo sequence [31] increases this time to 106 ms, as shown in Fig. 4.5.2.

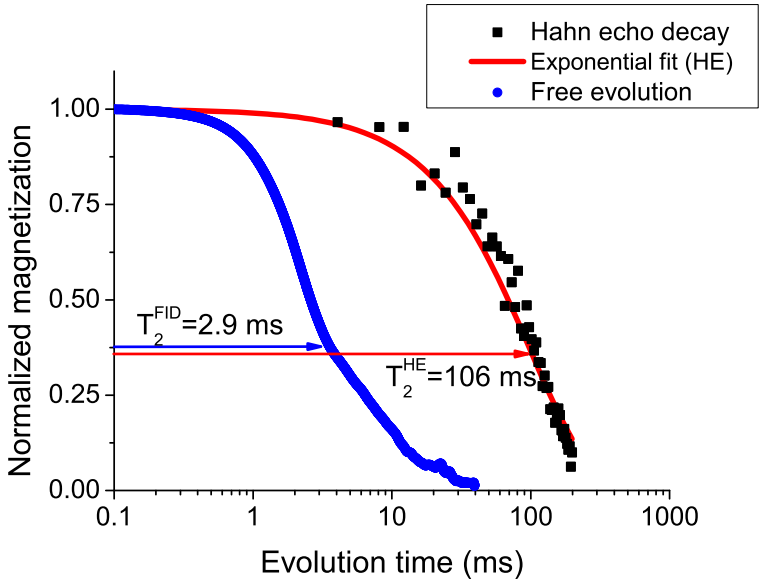

Figure 4.5.2.: Decay of the magnetization of the ^{1}H spin system under free evolution and in a Hahn spin-echo (HE) sequence.

4.6. Dynamical decoupling sequences

In earlier works using these sequences, the conditions were chosen such that the dominant perturbation was the environmental noise [36, 42, 62, 64, 65]. In this work, we focus on a system that allows us to make a comparison between these sequences in a regime where all sequences perform equally well at eliminating the environmental noise and any differences in their performance can be attributed directly to their robustness, i.e. to their efficiency in suppressing the effect of pulse imperfections.

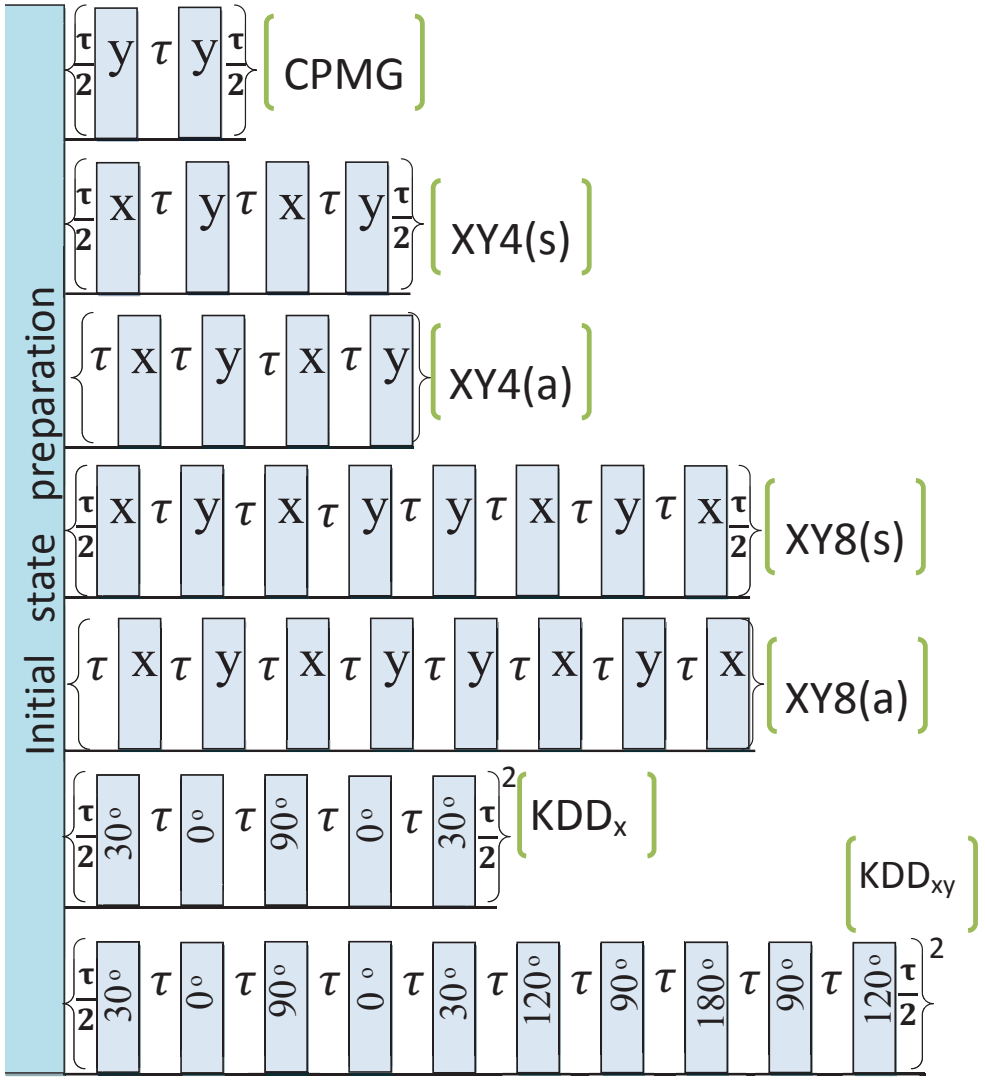

Figure 4.6.1.: Dynamical decoupling pulse sequences.

Figure. 4.6.1 gives an overview of the sequences that we examined to see the effect of pulse error on the performance of DD sequences. It shows a single cycle for each sequence, which is repeated as often as required. τ is the delay between the pulses. The Carr - Purcell (CP) sequence [69] and the version by Meiboom and Gill [70], well known in NMR community (CPMG), use the same sequence of refocusing pulses; they differ only with respect to the state to which they are applied. In the case of the CP sequence, the initial state is perpendicular to the rotation axis of the inversion pulses, while in the CPMG version, it is parallel. Errors in the flip angles leave the longitudinal component unscathed, but they destroy the perpendicular component [70, 36].

The sequence XY4 was introduced by Maudsley [103] and it reduces the effect of pulse imperfections for arbitrary initial states [103, 104, 36]. It consists of four pulses with

phases $x - y - x - y$ (Fig. 4.6.1). An asymmetric version of the XY-4 sequence was introduced by Viola *et al.* [21], which is designated XY4(a). The XY8-sequences are symmetrized versions of the XY4 sequences [104, 64]. Two DD sequences that are particularly robust against flip-angle and resonance offset errors are the KDD_x and KDD_{xy} sequences. KDD sequences are inspired from robustness of composite pulses [42, 65, 66]. KDD_{xy} is designed by combining the rotation pattern of the XY4 sequence with that of a robust composite pulse [113].

4.6.1. Data analysis

The extracted echoes (blue squares in Fig. 4.6.2) were fitted with an exponential function to obtain the decay time of the magnetization. Experiments were repeated for different delays between pulses, different DD sequences and initial conditions. Then the decay times plotted as a function of the delay between pulses. Figure 4.6.2 shows the echo train of a CPMG sequence. From these data, we extracted the signal (I_x magnetization in this example) at the end of each DD cycle (marked with blue squares in Fig. 4.6.2).A Matlab (Version 7.6) code is written to extract these points. Actually there were two different protocols to extract the values:

1. The echo maxima value during each cycle: this is easy but has the disadvantage that the transition or noise maybe greater than the echo maximum values.

2. Middle point between the pulses: this the most precise method and need precise calculations of the cycle time and the position of the echoes.

The decay of the echoes was mostly exponential fit to Eq. (4.6.1), with some exceptions discussed below.

$$M = M_\circ \exp(\frac{-t}{T_2}), \tag{4.6.1}$$

where:

M_0 : the maximum magnetization and T_2 : the transversal relaxation time decay constant.

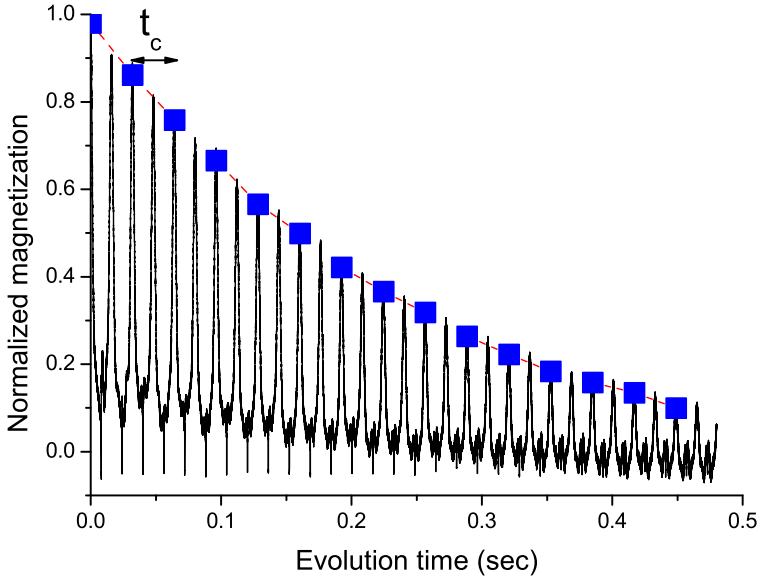

Figure 4.6.2.: Time evolution of the spin-system magnetization under the application of a CPMG sequence. The black solid line shows the evolution of the magnetization and the blue squares mark the echo amplitude at the end of a CPMG cycle. The echo maxima are used in this case for measuring the CPMG decay time. The cycle time was $t_c = 32$ ms.

4.6.2. Robustness comparison under pulse errors

To compare the sensitivity of the sequences to pulse imperfections, we prepared two orthogonal initial states I_x and I_y and then measured their decay as a function of time under the application of the different DD sequences described in Sec. (4.6).

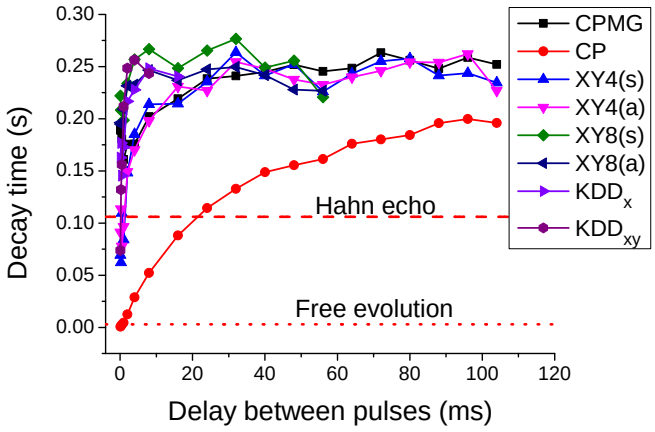

Figure 4.6.3.: Average decay times as a function of the delay τ between pulses for different DD sequences .

Figure 4.6.3 compares the decay times of different DD sequences as a function of the delay between pulses. For the CPMG sequence, we present the decay of the I_x and I_y magnetization separately, marked as CP and CPMG, respectively. Thus CPMG, CP sequences are very sensitive to the initial condition. For the other sequences, their perfor-

mance is quite symmetric with respect to the initial condition. For long delays between the pulses, the observed decay times reach a limiting value of ≈ 276 ms, irrespective of the sequence and the initial condition, and very close to the measured value of T_1. This is a verification of the assumption that all sequences can effectively decouple the slowly fluctuating environment.

For shorter pulse delays (i.e. more pulses in a given time interval), the signal decays more rapidly. This is most prominent for the CP sequence. In this situation, pulse imperfections add coherently and generate a rapid loss of magnetization [36].

As the pulse delays become shorter than 0.5 ms, which corresponds to 864 pulses during the 0.5 s measurement time, the other sequences also start to generate shorter decay times, and their decays become nonexponential. Figure 4.6.4 shows a representative example of such a signal. It can be fitted with a double exponential,

$$M(t) = a\, e^{-t/T_2^f} + b\, e^{-t/T_2^s} \tag{4.6.2}$$

with two decay times T_2^f and T_2^s.

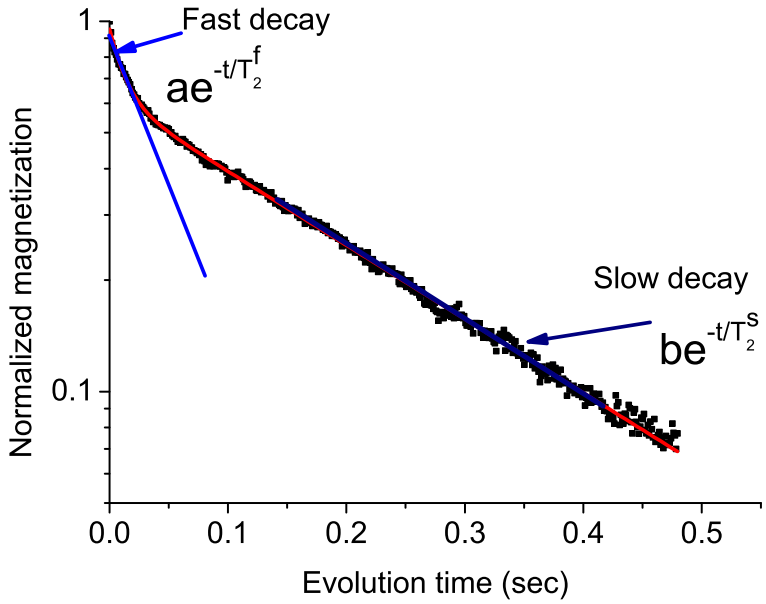

Figure 4.6.4.: Normalized spin magnetization as a function of the evolution time for short delays ($\tau = 100\,\mu$s) between the pulses for an XY8(s) sequence. Pulse errors dominate here, inducing a multi-exponential decay. The red solid line is a fit to eq. (4.6.2).

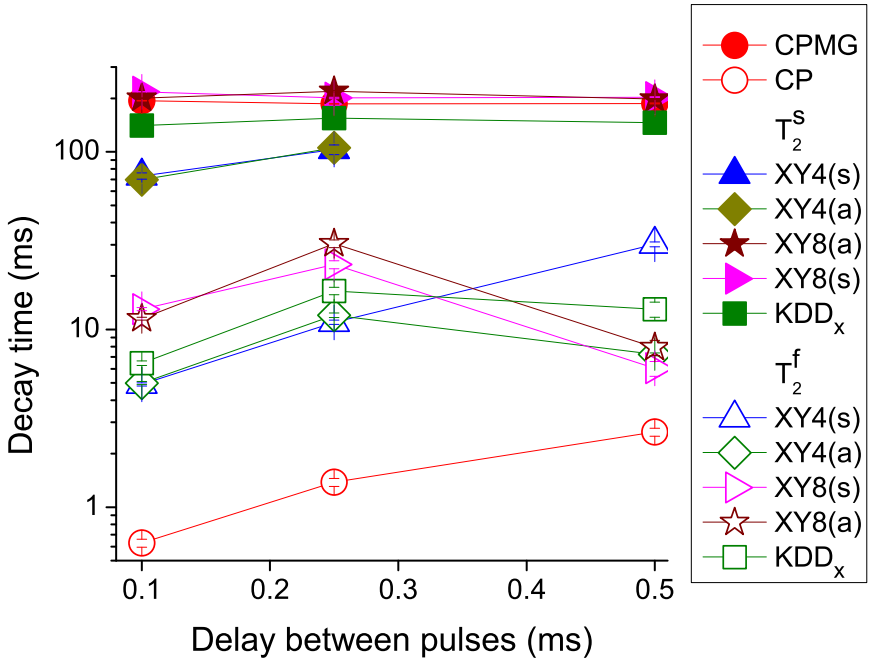

Figure 4.6.5.: Fitted decay times for the double-exponential decay

Figure 4.6.5 shows the decay times fitted with eq. (4.6.2) for different average delays between pulses. For the fast decay times (T_2^f), which are represented by empty symbols in Fig. 4.6.5, the performance of all DD sequences is quite similar. For the slow component (T_2^s, represented by filled symbols), XY8, CPMG, and KDD$_x$ perform better than XY4.

As we stated before, the decay time is dominated by the effect of pulse errors for short delays. The resulting average Hamiltonian projects the magnetization onto its eigenbase; this results in the fast decay component. After this projection, the remaining magnetization, which is not significantly affected by the pulse imperfections, decays on a slower timescale, which is dominated by the environment.

For a quantitative comparison of the different pulse sequences, we calculate the average magnetization decay resulting per pulse of the sequence. For this evaluation, we consider only the short-time component described by T_2^f.

Since the pulse error is the dominant source of decay under these conditions, we quantify its effect by measuring the fractional decay of the magnetization per pulse. The pulses are the same for all the DD sequences, but their effect, averaged over full cycles, shows how well the sequence is able to cancel the imperfections of the individual pulses.

Figure 4.6.6 shows the average decay per pulse for the different sequences, plotted against the number of pulses. For these data, the interpulse delay was $\tau = 100\ \mu s$. The most conspicuous feature is that CP performs very badly and CPMG very well. The compensated sequences lie between these two extremes, and we find that the higher order sequences (XY8, KDD) perform better than the lower order sequences (XY4). For unknown initial conditions, KDD shows the best performance. Under the present conditions, sequences that differ only with respect to time reversal symmetry perform quite similarly, in contrast to other cases discussed earlier [64].

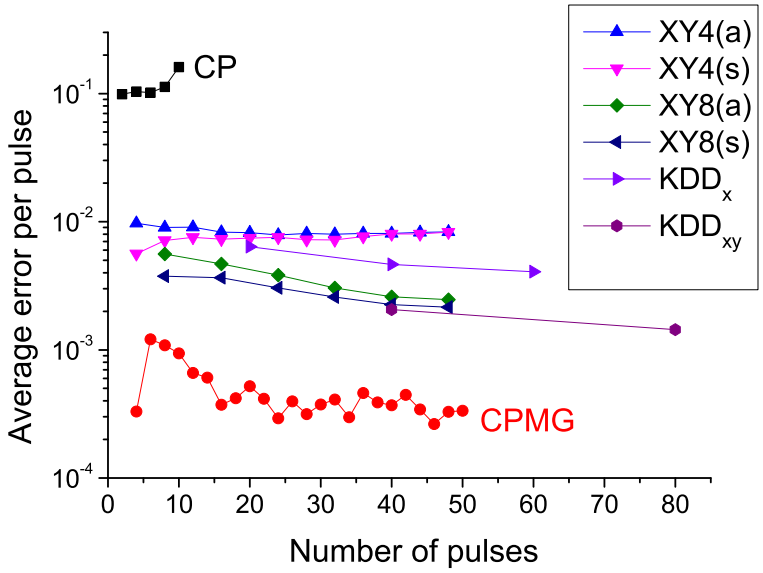

Figure 4.6.6.: Average error per pulse for different DD sequences with delay τ =100μs.

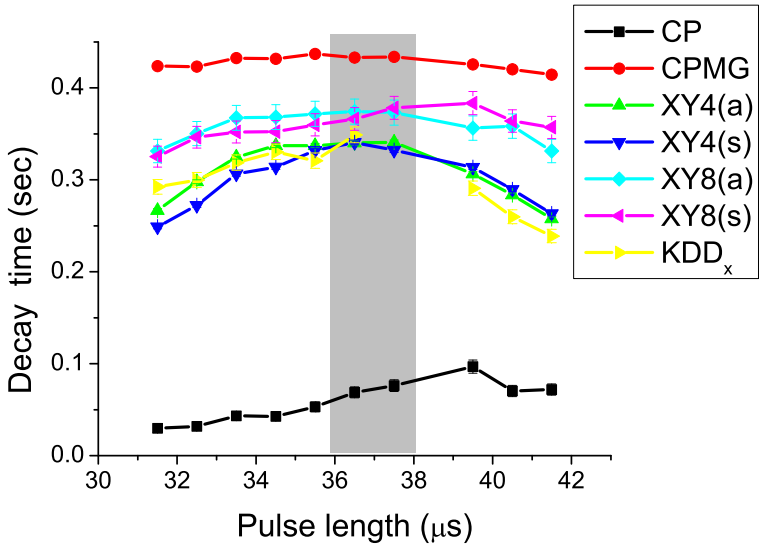

Figure 4.6.7.: Decay times of different DD sequences as a function of the pulse length of the DD pulses. The delay between pulses is 16 ms.

The DD sequence performance is sensitive to flip angle errors. We performed an experiment where we changed the pulse length and measure the decay times for each DD sequence. Figure 4.6.7 shows a comparison between decay times for the DD sequences versus small deviation in pulse length from the optimal π-pulse value where the average delay between pulses is 16 ms. The light gray rectangle (Fig. 4.6.7) marks the optimal values for the pulse length which correspond to the longest decoherence times.

4.7. Engineering the environment by external modulation field

The z shim generates a constant field along z axis. It would be interesting to have time-dependent field along z axis, for this purpose we change the experimental setup by building a new coil to generate an external field as explained below.

4.7.1. Experimental modification to generate additional field perturbation

In order to build an additional coil to generate an external time-dependent field along the z axis, the position of the rf coil inside the probe is determined. In liquid NMR spectrometer's 5 mm probes (i.e. NMR sample tube diameter) the sample length should be above and below the active region of the probe's coil, i.e. longer than 2 cm (length of the rf coil), in this case the sample-to-sample variations on the field homogeneity will be negligible. Otherwise the air has a different susceptibility which can affect the magnetic field homogeneity in the active region of the rf field. Another solution is to use susceptibility plugs matched with the NMR sample.

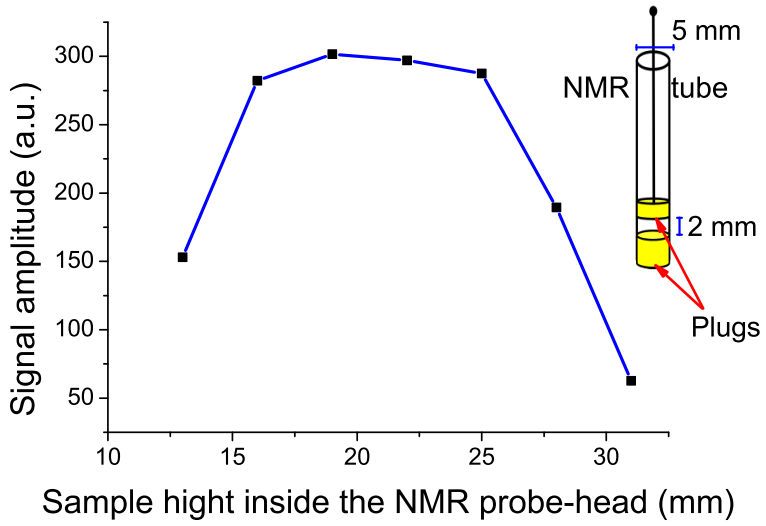

Figure 4.7.1.: NMR signal amplitude at different positions in the NMR probe-head along the z axis. In the right side is the NMR tube where plugs (yellow) are used to restrict an NMR sample of 2 mm length.

First the position of the rf coil is determined by moving the sample vertically along the NMR probe and measuring the NMR signal at different positions. Magnetic susceptibility plugs of polyetherimide is used to restrict the water sample to which we added 5 mg/100 ml $CuSO_4$. The length of the sample was 2 mm. Figure 4.7.1 shows the experimental data for an NMR signal at different positions in the NMR probe-head along the z axis, the highest signal located when the sample passes through to the coil position inside the NMR probe-head (in the yellow cylinder Fig. 4.7.2). Figure 4.7.2 shows the construction method of building the new coil to generate an additional time-dependent field along the z axis.

The new coil is a Helmholtz coil: a pair of circular coils on a common axis with equal currents flowing in the same sense is built at the center of the probe where the sample is located vertically along the z direction. An arbitrary wave generator (AWG) is used to generate a time-dependent signal, which is amplified and sent to the new coil to generate the desired field.

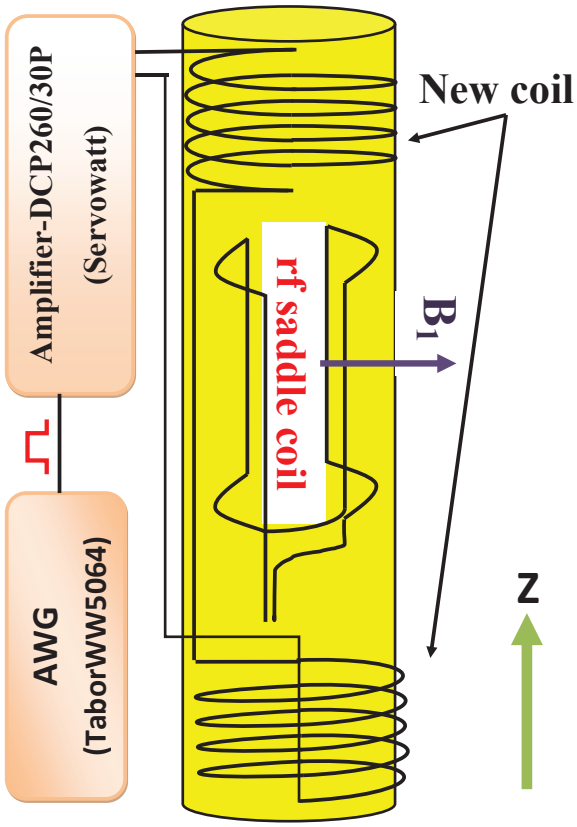

Figure 4.7.2.: Block diagram of the rf coil inside the NMR probe-head and the new coil is winded around the probe head and the devices for generating an additional time-dependent field (arbitrary wave generator [AWG] and an amplifier).

Figure 4.7.3 shows experimental data for calibration of the new setup to generate an additional filed using the new coil. Increment the DC voltage at the input of the amplifier (i.e. output of the AWG) results in linear increment of the offset frequency and current through the new coil.

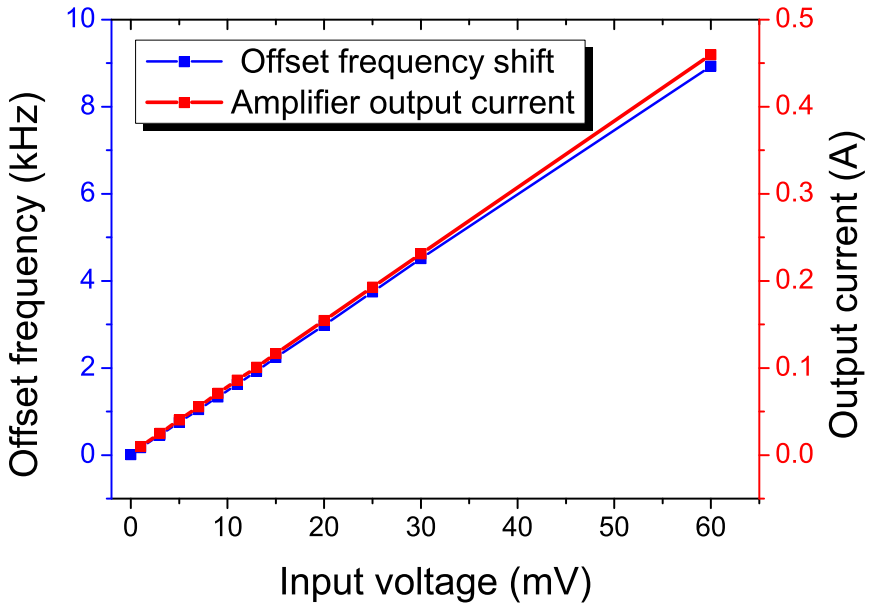

Figure 4.7.3.: Experimental data of the offset frequency for a proton (H_2O) NMR spectrum (blue squares) and current through the new coil (red squares) upon variation of the input voltage to the amplifier (used to generate current through the new coil).

4.7.2. Simulation of the FID signal during the sinusoidal modulation of the static magnetic field

The above discussion shows how the setup is optimized, e.g., to avoid the non-linearity in the output field generated by the new coil. In this subsection we will describe briefly the simulation procedure and compare simulation results with experimental data.

4.7.2.1. Simulation procedure

A numerical simulation program using Matlab Version 7.6 for calculating the NMR time-domain signal or frequency-domain spectrum involves the following steps:

If we consider spin 1/2 system, the spin operators are :

$$S_x = 0.5 \begin{bmatrix} 0 & 1 \\ 1 & 0 \end{bmatrix}; \; S_y = 0.5 \begin{bmatrix} 0 & -i \\ i & 0 \end{bmatrix}; \; S_z = 0.5 \begin{bmatrix} 1 & 0 \\ 0 & -1 \end{bmatrix}. \tag{4.7.1}$$

The transverse spin magnetization S_m , is the sum of the magnetization on x axis (S_x) and the magnetization on y axis (S_y) by Eq. (4.7.2):

$$S_m = S_x + iS_y. \tag{4.7.2}$$

The quantum state of the entire ensemble of the isolated spins 1/2 can be described using the spin density operator matrix ρ without referring to the individual spin states. Using the differential Liouville-von Neuman equation mentioned in chapter two, Eq. (2.1.5) we can rewrite

$$\frac{d}{dt}\rho(t) = -i[\mathcal{H}(t), \rho(t)], \tag{4.7.3}$$

which can be solved similarly as Eq. (2.1.16) to give

$$\rho(t) = U(t)\rho(0)U^{-1}.(t) \tag{4.7.4}$$

However U is defined by Eq. (4.7.5):

$$U(t) = T\exp\left\{-i\int_0^t \mathcal{H}(t')dt'\right\}, \tag{4.7.5}$$

where

U^{-1} is the complex conjugate transpose of the operator U.

T is the Dyson time ordering operator, which is defined to solve the exponential function at different times when they do not commute with each other.

If we introduce an additional perturbation which can be defined by a sinusoidal function oscillating along the static magnetic field then we can write the Hamiltonian as

$$\mathcal{H} = A(\sin(\Omega t' + \phi))S_z + \Omega_0 S_z, \tag{4.7.6}$$

where:

$\Omega, \phi, A =$ are consecutively the frequency, the initial phase, and the amplitude of the sinusoidal perturbation.

$\Omega_0 = \omega_l - \omega_{off}$ is the offset difference between the Larmor frequency and the transmitter rf frequency.

Assuming that $\Omega_\circ = 0$, we can write:

$$\int_0^t \mathcal{H}(t')dt' = \frac{AS_z}{\Omega}\left[-\cos(\Omega t' + \phi)\right]_0^t, \tag{4.7.7}$$

where: the integration is limited by the time interval of the sine wave t, this gives:

$$\int_0^t \mathcal{H}(t')dt' = \frac{AS_z}{\Omega}\left(-\cos(\Omega t + \phi) + \cos\phi\right). \tag{4.7.8}$$

We can write the evolution operator from Eq. (4.7.5) using Eq. (4.7.8):

$$U(T') = e^{\frac{-iAS_z}{\Omega}(-\cos(\Omega t+\phi)+\cos\phi)}. \tag{4.7.9}$$

If the spin density operator at thermal equilibrium state which is along the z axis (S_z) we can write :

$$\rho(0) = S_z. \tag{4.7.10}$$

Applying $\pi/2$ pulse:

$$S_z \to S_x. \tag{4.7.11}$$

.

We can calculate the FID by matrix multiplication, we use the evolution operator from Eq. (4.7.9). Using Eq. (4.7.11) and Eq. (4.7.4), we can calculate the density matrix $\rho(t)$. Then the expectation values of the magnetization are calculated by tracing the product of

the observable S_m as in Eq. (4.7.2) and the calculated density matrix $\rho(t)$. Then the result is the calculated value for the magnetization without including relaxation. To include relaxation we multiply the magnetization with an exponential function with a decay constant T_2^*. T_2^* is a decay time combined of two decay times: molecular interaction (T_2) and variations in B_0(i.e. magnetic field inhomogeneities = $T_{2inh.}$) given by Eq. (4.7.12) [76]:

$$1/T_2^* = 1/T_2 + 1/T_{2inh.}. \tag{4.7.12}$$

T_2^* can be measured directly from the FID decay.

4.7.2.2. Simulation results versus experimental data

The FID signal is measured under the sinusoidal modulation field with a frequency of 60 Hz as shown in Fig. 4.7.4. The sinusoidal modulation (i.e. modulated field) changes the phase of the FID. To show this change clearly, the data are converted from Cartesian coordinate to polar coordinate. The contour plots in Fig. 4.7.5 show the polar representation (i.e. amplitude/phase) for the simulation and the experimental data of the spin magnetization under the sinusoidal modulation. The spin magnetization is measured versus evolution time after a $\pi/2$ pulse synchronized with the pulse. During the sinusoidal modulation the spin magnetizations are measured experimentally for different frequency values (i.e. for the sine wave modulation): [Ω = 5 Hz, 60 Hz, 1 kHz] with an amplitude: A=10 mV(pp) = 3.54 mV (rms). In this comparison we are able to have consistence between simulation and experiments. For simulations we used the same parameters in the experiments (the amplitude for the sine wave: 3.54 mV (rms), which is equivalent to 528 Hz offset when applying DC with 3.54 mV, and the exponential decay time T_2^*= 0.020 sec, we have an offset of 70 Hz).

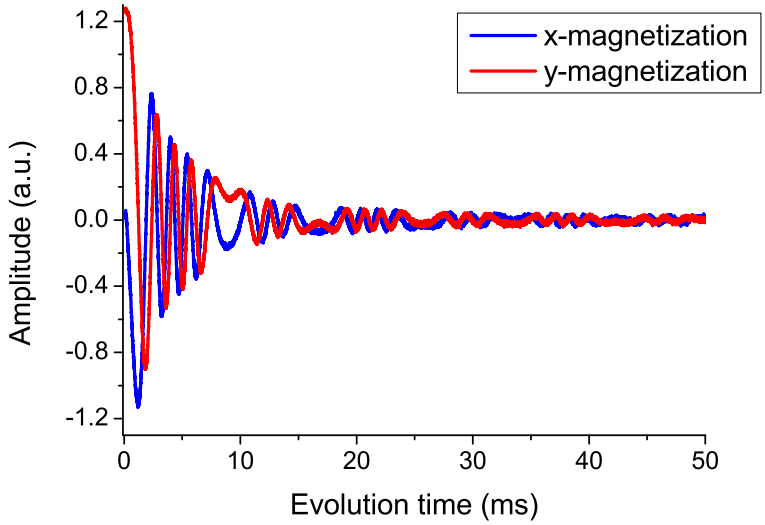

Figure 4.7.4.: Effect of sinusoidal modulation field on the FID where the modulated sinusoidal field has an effective amplitude of 3.54 mV and a frequency of 60 Hz. The magnetization is measured in both x axis (blue line) and y axis (red line).

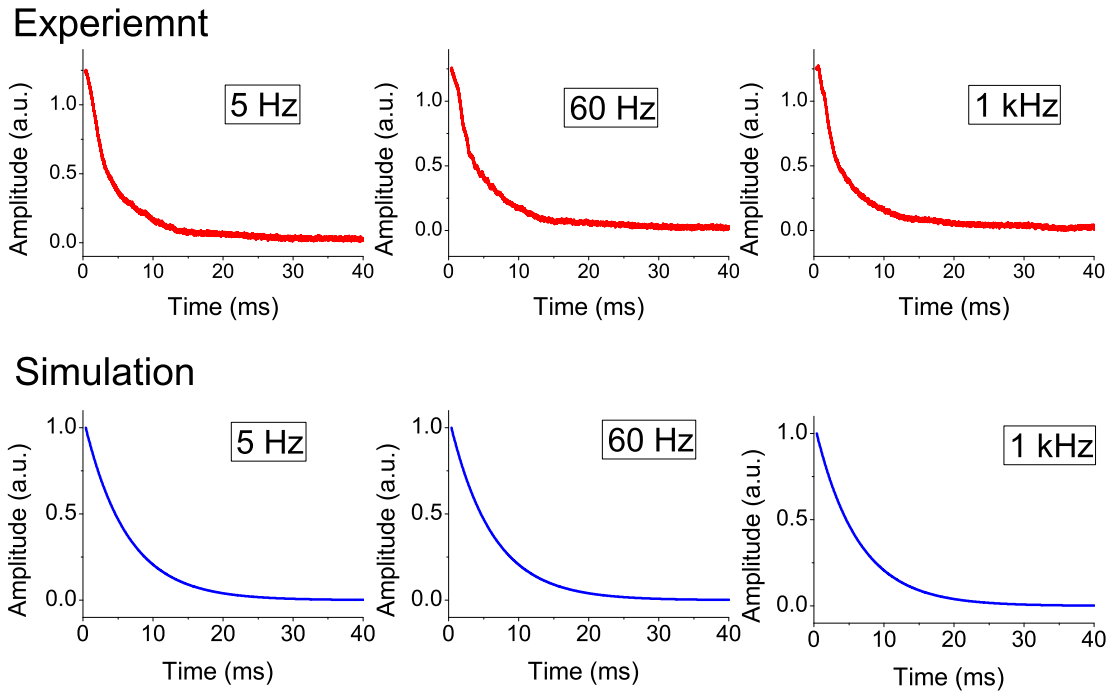

(a)

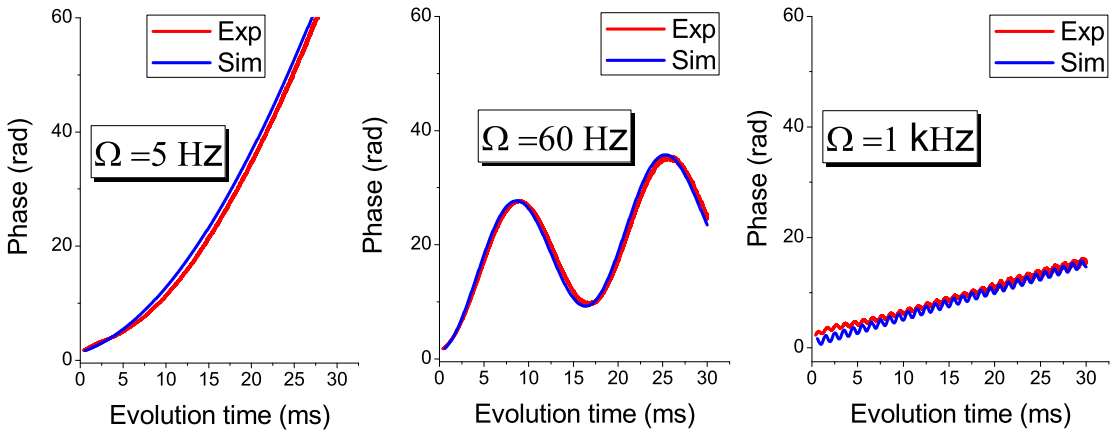

(b)

Figure 4.7.5.: Time evolution of magnetizations for experimental data and simulations during the sinusoidal modulation field with frequencies of 5 Hz, 60 Hz, 1 kHz. . The magnetizations are shown in the polar coordinate with the amplitude (Fig. 4.7.5a) and phase (Fig. 4.7.5b).

4.7.3. Dynamical decoupling pulse sequence performance under sinusoidal modulation

Noise spectroscopy in quantum computation systems uses the advantage that qubit can be used as a noise probe. An unknown spectral density can be determined by using DD sequences. The decay rates of the DD sequences are given by the spectral density at discrete frequency [54, 53].

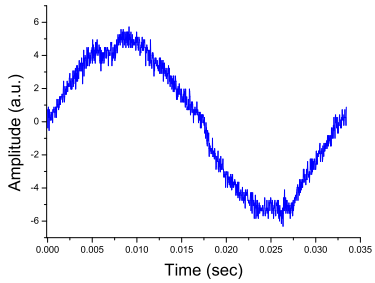

(a) Sinusoidal signal used for the field modulation to engineer the environment.

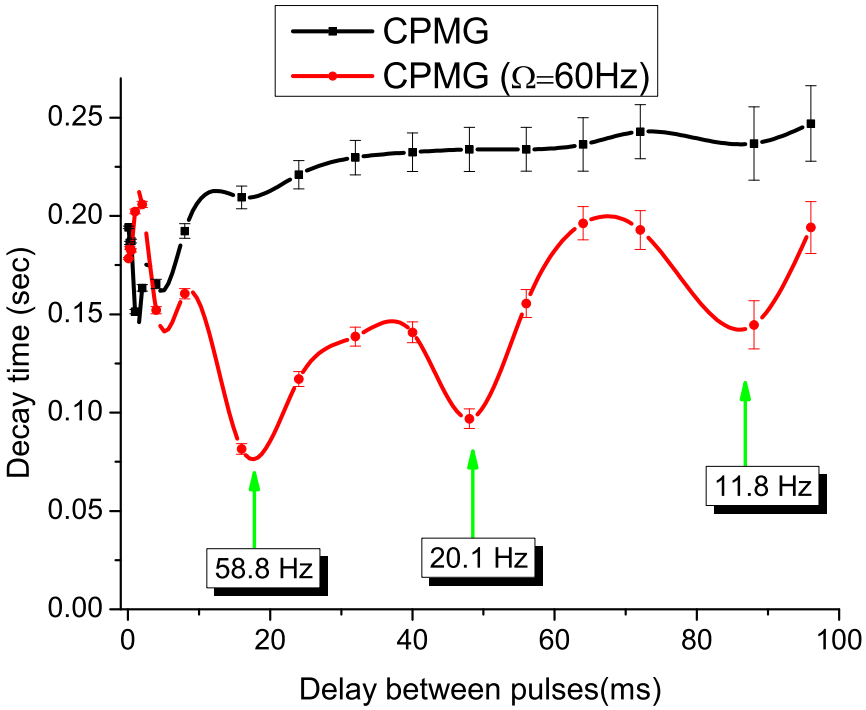

Figure 4.7.6.: Decay times as a function of the delay τ between pulses for the CPMG sequences (black) compared with the CPMG sequence under the sinusoidal modulated field (red). The sinusoidal field has a frequency of 60 Hz with a magnetic field strength of 0.0124 mT for longitudinal initial condition.

In our case we apply, instead of a noise function, a direct modulation sinusoidal signal with a define frequency to engineer the environmental spectral density. The CPMG sequence is applied to our system under a sinusoidal perturbation on the z axis with a frequency of 60 Hz and a magnetic field strength of 0.0124 mT. Figure 4.7.6 shows the decay times of the CPMG sequence (black) due to delay between pulses without the sinusoidal modulation signal (shown in Fig. 4.7.6a). The CPMG sequence performance deviates from the usual performance when applying the modulation field. The green arrow shows the first dip in Fig. 4.7.6 at 17 ms which corresponds to a modulation frequency of 58.8 Hz, which is near to our sinusoidal modulation frequency ≈60 Hz. This small difference between the modulation frequency and the measured one by the CPMG could be result from the uncontrolled noise coupled with the modulation sinusoidal field.

The main peak in Fig. 4.7.6 at the modulation frequency (60 Hz) has some satellite

peaks at lower frequencies. The decay of the main peak and its satellite peaks for the CPMG sequence under the modulation (sinusoidal field with a frequency Ω) can be given by

$$R(t) = \Omega/n, \tag{4.7.13}$$

where n=1,3,5.

These experimental results obviously show that we can see the second and the third dip near the third and matched exactly with the fifth fractions of the modulation frequency.

4.7.4. Rf coil inhomogeneity

The rf is power is strongly dependent on the geometrical construction of the rf coils [30]. For a given system, the field inhomogeneity can be measured from the nutation experiment where the pulse width is increased with the decay of the magnetization till it decays to zero. The field inhomogeneity can be determined from the spectral line shapes. The nutation experiment results in Figure 4.7.7 shows that the magnetic field inhomogeneity is $\approx$12%, where a) is the time domain data and b) its spectrum.

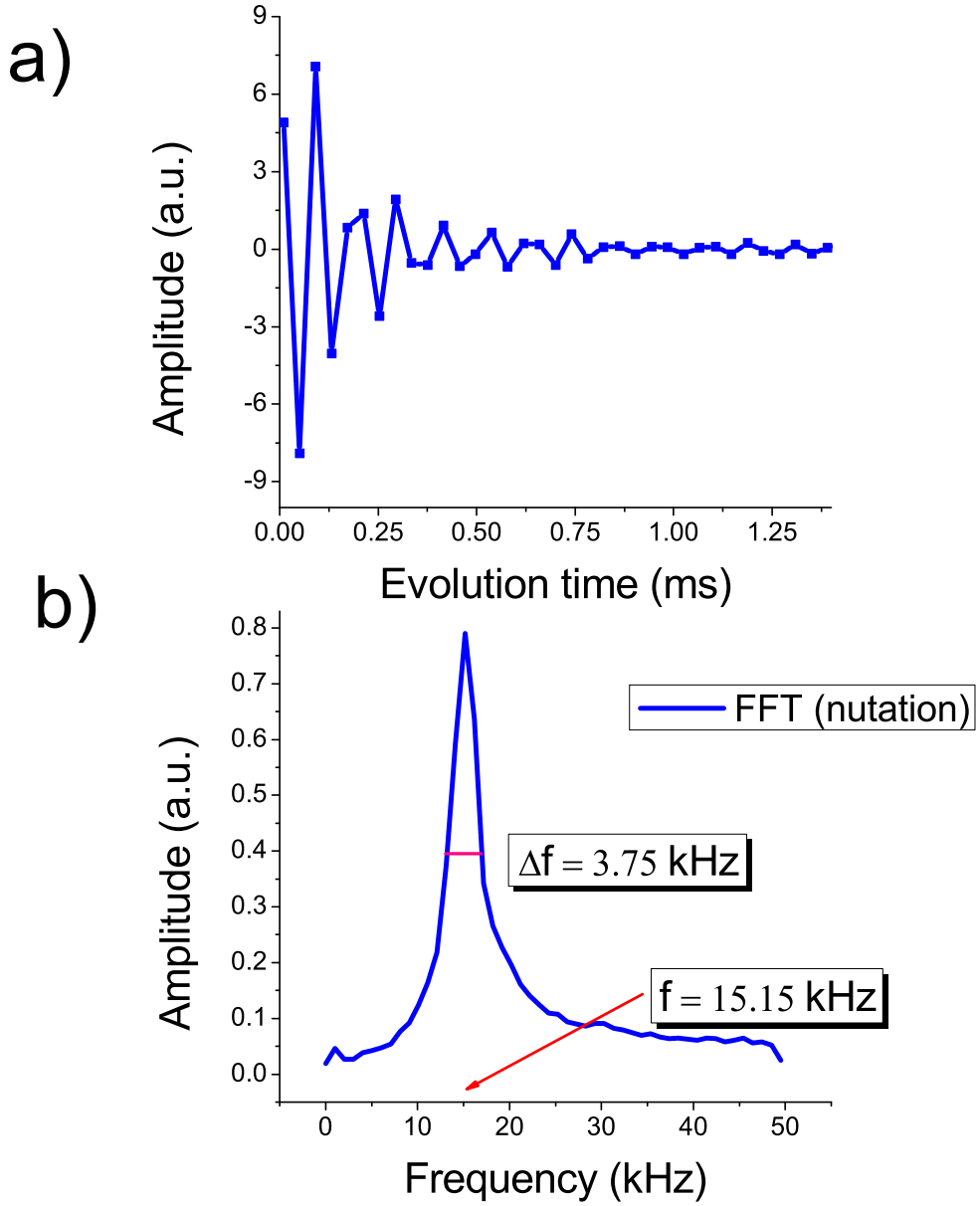

Figure 4.7.7.: Long nutation experiment to determine the field inhomogeneity: a) The nutation experiment b) Its spectrum (Fourier transform of (a))

4.8. Theoretical analysis of dynamical decoupling sequences by average Hamiltonian theory

4.8.1. Introduction

Manipulation of Hamiltonian requires an external time-dependent or an independent perturbation acts on the system. Time-independent perturbation changes can be, e.g., pressure or temperature. On the other hand time-dependent perturbations can be applied or removed quickly such as sample spinning or radio frequency pulses.

The average Hamiltonian theory (AHT) was first introduced by Haeberlen and Waugh

to interpret cyclic pulse sequences in the aim of seeking experimental methods for accomplishing high resolution solid NMR [114]. AHT describes the effect of the time-dependent perturbation Hamiltonian of multiple pulse sequences applied to the system during an interval $t_1 < t' < t_2$. The primary aim from AHT was to eliminate static dipolar line broadening in solids. Generally AHT can help to control the system efficiently without full knowledge of the system dynamics [30]. There is a minimum limit for the pulse spacing τ, for which it is possible to detect the FID signal between the pulses. This minimum is determined by a variety of technical limitations, such as rise and fall times, widths of square pulses and recovery time of the sensing system ($0 \ll \tau \ll \infty$).

If the evolution of the system is governed by a time-dependent Hamiltonian $\mathcal{H}(t)$, the effective evolution can be described by an average Hamiltonian $\widetilde{\mathcal{H}}(t_1, t_2)$. The Hamiltonian $\mathcal{H}(t)$ is periodic with cycle time t_c. The ratio t_c/T_2 is made usually small so that the system develops over long times Mt_c, where M is the number of cycles.

4.8.2. Average Hamiltonian theory calculations for dynamical decoupling sequences

Now we present the calculations of the AHT terms for the DD pulse sequences: XY4, XY8, CPMG and KDD$_x$. We consider a DD sequence with only flip angle errors. To simplify the calculation procedure, the Hamiltonians are transformed to the toggling frame (or the interaction picture), [115].

The remaining environmental noise fluctuates so rapidly that its effects cannot be reduced by DD as described in Sec. (4.2). It is a good approximation to describe these rapid fluctuations as a classical field affecting the precession frequency of the spins [77]. Thus Eq. (4.2.2) can be written

$$\mathcal{H}_{SE} = \Delta\omega_z(t) S_z, \tag{4.8.1}$$

where the average of the random precession frequency is $\langle \Delta\omega_z(t) \rangle = 0$ for every t. The effects of the environment will be an exponential attenuation e^{-t/T_2} independent of the delay between pulses.

We can write the pulse propagator as a composition of the product of the ideal pulse propagator $R_\phi = e^{-i\pi S_\phi}$ with a phase ϕ and two additional evolutions for flip angle errors as

$$R_\phi = e^{-i(1+\epsilon)\pi S_\phi} = e^{-iH_\phi(t_{p/2})} e^{-i\pi S_\phi} e^{-iH_\phi(t_{p/2})}, \tag{4.8.2}$$

where $H_\phi = \frac{\epsilon\pi}{t_p} S_\phi$ and t_p is the pulse length,

$$S_\phi = \cos(\phi) S_x + \sin(\phi) S_y. \tag{4.8.3}$$

The zero- and first-order average Hamiltonians terms are given by Eqs. 4.8.4, 4.8.5 under these two conditions:

1) $\mathcal{H}(t)$ is periodic: $\mathcal{H}(t) = \mathcal{H}(t + t_c)$.

2) The observation is stroboscopic and synchronized with the period of the Hamiltonian t_c, the evolution operator is $\exp\left\{-i\widetilde{\mathcal{H}}(0, t_c)\, Mt_c\right\}$where $\widetilde{\mathcal{H}}$is the effective Hamiltonian [114, 116].

$$\widetilde{\mathcal{H}_0} = \frac{1}{t_c}\sum_n \mathcal{H}_n \tau_n, \tag{4.8.4}$$

where $n = 1, 2, 3, ...$ and τ_n is the delay between pulses.

$$\widetilde{\mathcal{H}_1} = \frac{-i}{2t_c}\{\mathcal{H}_2\tau_2, \mathcal{H}_1\tau_1] + [\mathcal{H}_3\tau_3, \mathcal{H}_1\tau_1] + [\mathcal{H}_3\tau_3, \mathcal{H}_2\tau_2] + ...\}. \tag{4.8.5}$$

In the next calculations we will assume that the environment Hamiltonian $\mathcal{H}_E$=0.

4.8.2.1. XY4(s) and XY4(a) pulse sequence

For the sequences XY4(s) and XY4(a) considering the effect of the flip angle error the zeroth-order average Hamiltonian vanishes and the first-order term for both sequences is [64]

$$\widetilde{\mathcal{H}_1}^{XY4(s)} = \widetilde{\mathcal{H}_1}^{XY4(a)} = \frac{5\epsilon^2\pi^2}{16\tau} S_z, \tag{4.8.6}$$

where the second term shown in Ref. ([64]) vanishes, because the environment Hamiltonian (as in Eq. (4.6.2)) commutes with the system Hamiltonian.

This shows that there is no difference between symmetric and asymmetric sequences of the sequence XY4 up to first order terms of the average Hamiltonian, which is in good agreement with the experimental results of Fig. 4.6.6.

We consider now the XY8(s) and XY8(a) sequences. The zero-order and the first-order average Hamiltonian terms are null considering only the flip angle error effects [64]. Then the second-order term, is equal for both version of the XY8 sequence, is given by [64]

$$\widetilde{\mathcal{H}_2}^{XY8(s)} = \widetilde{\mathcal{H}_2}^{XY8(a)} = \frac{13\epsilon^3\pi^3}{1536\tau}(S_x + S_y). \tag{4.8.7}$$

This is also in good agreement with Fig. 4.6.6 where the symmetric and asymmetric versions of the sequence XY8 behave similarly, moreover they are more robust than the XY4 sequences.

4.8.2.2. CPMG and CP pulse sequence

Figure 4.8.1 shows a schematic representation of the CPMG pulse sequence and the rotation of the initial frame to the toggling frame due to the pulses.

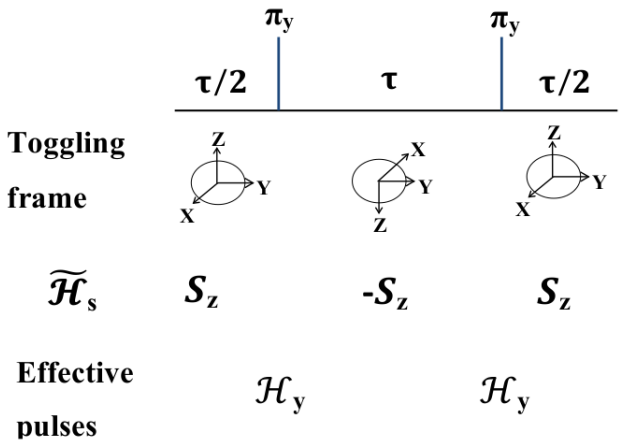

Figure 4.8.1.: Schematic representation of the CPMG dynamical decoupling sequence and the terms of the average Hamiltonian in the toggling frame. In each cycle of total length $t_c = 2\tau$, the two pulses spaced by τ and lead to a rotated coordinate system, known as toggling frame. The average Zeeman Hamiltonian is obtained by averaging the transformed Hamiltonian in the toggling frame.

Using Eqs. (4.6.2), (4.8.2), (4.8.3) the effective Hamiltonian terms can be written as

$$\tau_1\mathcal{H}_1 = \tau_1(\mathcal{H}_{SE}) + \frac{t_p}{2}\mathcal{H}_y = \frac{\tau}{2}(\omega_z S_z) + \frac{\epsilon\pi}{2}S_y, \tag{4.8.8}$$

$$\tau_2\mathcal{H}_2 = \tau_2(-\mathcal{H}_{SE}) + t_p\mathcal{H}_y = \tau(-\omega_z S_z) + \epsilon\pi S_y, \tag{4.8.9}$$

$$\tau_3\mathcal{H}_3 = \tau_3(\mathcal{H}_{SE}) + \frac{t_p}{2}\mathcal{H}_y = \frac{\tau}{2}(\omega_z S_z) + \frac{\epsilon\pi}{2}S_y. \tag{4.8.10}$$

Explicit calculations for the above terms using Eqs. (4.8.4, 4.8.5) give the zero-order term:

$$\widetilde{\mathcal{H}}_0^{CPMG} = \frac{2\epsilon\pi S_y}{t_c}, \tag{4.8.11}$$

and the first-order

$$\widetilde{\mathcal{H}}_1^{CPMG} = 0. \tag{4.8.12}$$

In the CPMG experiment, the initial condition is $\propto S_y$, which commutes with the average Hamiltonian zero-order term (Eq. 4.8.11) and is therefore not affected by pulse errors. In the CP experiment, the initial condition is $\propto S_x$, which is dephased by the pulse errors, in agreement with the data in Fig. 4.6.6 [36].

4.8.2.3. KDD$_x$ pulse sequence

The KDD$_x$ cycle is composed of ten pulses as in Fig. 4.6.1, thus we can write the effective Hamiltonian terms as

$$\tau_1\mathcal{H}_1 = \tau_1(\mathcal{H}_{SE}) + \frac{t_p}{2}(\mathcal{H}_{30}), \tag{4.8.13}$$

$$\tau_2\mathcal{H}_2 = \tau_2(-\mathcal{H}_{SE}) + \frac{t_p}{2}(\mathcal{H}_{30} + \mathcal{H}_{60}), \tag{4.8.14}$$

$$\tau_3\mathcal{H}_3 = \tau_3(\mathcal{H}_{SE}) + \frac{t_p}{2}(\mathcal{H}_{60} + \mathcal{H}_{150}), \tag{4.8.15}$$

$$\tau_4\mathcal{H}_4 = \tau_4(-\mathcal{H}_{SE}) + \frac{t_p}{2}(\mathcal{H}_{150} + \mathcal{H}_{-120}), \tag{4.8.16}$$

$$\tau_5\mathcal{H}_5 = \tau_5(\mathcal{H}_{SE}) + \frac{t_p}{2}(\mathcal{H}_{-120} + \mathcal{H}_{-y}), \tag{4.8.17}$$

$$\tau_6\mathcal{H}_6 = \tau_6(\mathcal{H}_{SE}) + \frac{t_p}{2}(\mathcal{H}_{-y}), \tag{4.8.18}$$

$$\tau_7\mathcal{H}_7 = \tau_7(-\mathcal{H}_{SE}) + \frac{t_p}{2}(\mathcal{H}_{-y}), \tag{4.8.19}$$

$$\tau_8\mathcal{H}_8 = \tau_8(H_{SE}) + \frac{t_p}{2}(\mathcal{H}_{-120} + \mathcal{H}_{-y}), \tag{4.8.20}$$

$$\tau_9\mathcal{H}_9 = \tau_9(-\mathcal{H}_{SE}) + \frac{t_p}{2}(\mathcal{H}_{150} + \mathcal{H}_{-120}), \tag{4.8.21}$$

$$\tau_{10}\mathcal{H}_{10} = \tau_{10}(\mathcal{H}_{SE}) + \frac{t_p}{2}(\mathcal{H}_{60} + \mathcal{H}_{150}), \tag{4.8.22}$$

$$\tau_{11}\mathcal{H}_{11} = \tau_{11}(-\mathcal{H}_{SE}) + \frac{t_p}{2}(\mathcal{H}_{30} + \mathcal{H}_{60}), \tag{4.8.23}$$

$$\tau_{12}\mathcal{H}_{12} = \tau_{12}(+\mathcal{H}_{SE}) + \frac{t_p}{2}(\mathcal{H}_{30}), \tag{4.8.24}$$

where:

$$\mathcal{H}_x = S_x\frac{\epsilon\pi}{t_p},\ \mathcal{H}_y = S_y\frac{\epsilon\pi}{t_p}, \tag{4.8.25}$$

$$\mathcal{H}_{30} = \left(\frac{\sqrt{3}}{2}S_x + \frac{1}{2}S_y\right)\frac{\epsilon\pi}{t_p}, \tag{4.8.26}$$

$$\mathcal{H}_{60} = \left(\frac{1}{2}S_x + \frac{\sqrt{3}}{2}S_y\right)\frac{\epsilon\pi}{t_p}, \tag{4.8.27}$$

$$\mathcal{H}_{150} = \left(-\frac{\sqrt{3}}{2}S_x + \frac{1}{2}S_y\right)\frac{\epsilon\pi}{t_p}, \tag{4.8.28}$$

$$\mathcal{H}_{-120} = \left(-\frac{1}{2}S_x - \frac{\sqrt{3}}{2}S_y\right)\frac{\epsilon\pi}{t_p}, \tag{4.8.29}$$

$$\mathcal{H}_{-90} = -S_y\frac{\epsilon\pi}{t_p}. \tag{4.8.30}$$

Explicit calculations of the previous twelfth Hamiltonian terms and using Eqs. (4.8.4, 4.8.5) give the zero-order

$$\widetilde{\mathcal{H}_0}^{KDD_x} = 0, \tag{4.8.31}$$

and the first-order as

$$\widetilde{\mathcal{H}_1}^{KDD_x} = 0. \tag{4.8.32}$$

The higher order terms were kept small by the design of the sequence. As shown in Ref. [117], this makes it robust against several systematic errors because it is a geometric quantum gate. In Ref. [42], a numerical simulation and experimental data showed that the KDD$_{xy}$ sequence is more robust against flip angle errors than the other DD sequences tested [113, 118]. Overall, the experimental comparison between the different sequences is in good agreement with the numerical simulations and analytical results based on average Hamiltonian theory.

5. Conclusion and outlook

5.1. Conclusion

In this project the experimental setup of the liquid NMR experiment (i.e. spectrometer configuration) was discussed. In addition, we were able to analyze the main sources of the electronic noise emitted from different devices. Also, we could reduce a kind of coherent noise (i.e. 50Hz noise) by separating common ground connections. Moreover, we constructed and tested a new setup configuration for the H-channel to avoid the complexity of using different frequency sources for generating rf pulses.

Optimization procedures such as tune-up sequences were applied towards performing high fidelity NMR quantum computing experiments. Furthermore, suitable repeated experimental times were optimized by adding $CuSO_4$ to the NMR sample to avoid obstacles (e.g. radiation damping). For quantum memory purposes, we have tested the robustness of different DD sequences by comparing them in an environment that interacts with the spins in such a way that the decoherence time under the application of DD sequences with ideal pulses is independent of the delay times between the pulses. This allowed us to study the robustness of the different DD sequences and thereby isolate the effects of the pulse errors. We found that the decoherence times of the most robust sequences, the KDD family, is the longest for arbitrary initial states. This is consistent with the measured error per pulse averaged over many cycles of a DD sequence, where the KDD sequences have the lowest effective error. In the regime studied, the time symmetrization of the cycles does not play a significant role in decoherence reduction, whereas only the phases of the pulses are important for reducing the effect of pulse errors.

In order to study the environmental decoherence sources and find the appropriate DD sequence for quantum computing, an additional coil was built in the experimental setup. Through this coil, using an AWG and a pulse amplifier, we were able to generate a time-dependent field which is synchronized with the pulse timing. We were able to achieve agreement with the simulated FID and experimental data under the effects of this sinusoidal modulation. The sine function modulation is applied to the system synchronized with the CPMG pulse sequence. The sinusoidal modulation frequency value is matched with the value measured by the experimental CPMG sequence decay time. Finally we calculated the average Hamiltonian terms for CPMG and KDD_x sequences taking into account flip angle errors. Comparing the expression of both versions (symmetric and asymmetric) of the sequences XY4 and XY8 showed no differences. Our experimental results for pulse errors are consistent with numerical simulations and predictions of average Hamiltonian theory.

Our results can be useful for better understanding of experimental implementations of DD sequences, and the influence of errors on quantum control of spin systems. Our findings strongly support that liquid NMR works as a good testbed for DD sequences and studying environmental decoherence effects. Our system can be a helpful tool for

simulating other unknown systems by inserting different kind of noise, which can be useful to better understanding for the decoherence effects.

5.2. Five-spin system for dynamical decoupling

Now we summarize some preparation experiments on the proposed molecule, 1,2-difluoro-4-iodobenzene for quantum computation experiments. The experiments were done on a Bruker Avance II 500 MHz spectrometer. The above mentioned molecule (1,2-difluoro-4-iodobenzene) composed of two fluorine atoms (F1, F2) can be regarded as a two qubit system and three protons (H1, H2, H3) can be regarded as environment. The molecule (structure is shown in Fig. 5.2.1) was dissolved in the liquid-crystal solvent ZLI-1132 to retain the dipolar couplings between the spins. To have a homogenous mixture the following procedure was performed: the mixture was heated above its clearing point≈343 K, then properly stirred and cooled down. This procedure was repeated several times thoroughly. To have a stable and homogenous magnetic field, an external deuterium lock signal was implemented. The lock channel of the 500 MHz spectrometer requires a significant signal to maintain the rf stability. Therefor we used an insert tube of 5 cm length. According to the data from Ref. [119] we recalculated the Hamiltonian under controlled temperature of 295 K. Table 5.2.1 shows the parameters of the spin qubits in the molecule. Figure 5.2.2a shows the fitted spectrum of protons compared with experimental data after a $\pi/2$ hard pulse while Fig. 5.2.2b shows the fluorine spectra.

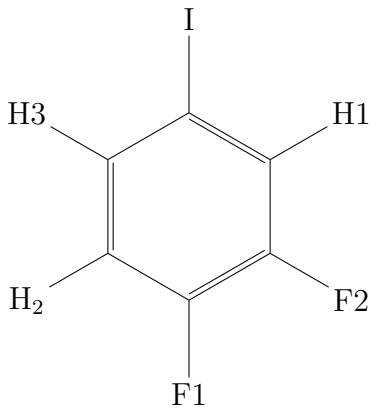

Figure 5.2.1.: Chemical structure of the molecule 1,2-difluoro-4-iodobenzene

	F1	F2	H1	H2	H3
F1	2603.7	-228.6	-292.1	-616.4	-321.8
F2		-1621.9	-2198.0	45.0	-55.3
H1			122.1	-35.8	52.0
H2				-37.4	-2605.5
H3					36.0
T_2^*	0.13	0.12	0.18	0.21	0.13

Table 5.2.1.: Parameters of the spin qubits in the molecule 1,2-difluoro-4-iodobenzene. The chemical shifts with respect to the transmitter frequencies of the proton and fluorine spins are shown as the diagonal terms and the dipolar couplings between spins are shown as the off-diagonal terms in units of Hz. The effective relaxation times T_2 are determined by fitting the peaks in the spectra.

We calculated some pulses, to use them in DD sequences. These pulses are strongly modulated pulses (SMP) for their robustness against flip angle errors and frequency offset errors. Table 5.2.2 shows some strong modulated pulses which are calculated for fluorine spins with different lengths and their theoretical fidelities[1].

no	pulse	pulse length (ms)	Fidelity %
1	π	1	97
2	π	1	97
3	π	1	97
4	π	1	99
5	$\pi/2$	2	97
6	$\pi/2$	2	97
7	$\pi/2$	2	97
8	$\pi/2$	2	97
9	$\pi/2$	0.496	97

Table 5.2.2.: Strongly modulated pulses calculated for fluorine spins with different lengths and their theoretical fidelity

[1]The pulses are located in: `afp://chaos._afpovertcp._tcp.local/Pulseprograms/Pulseprograms500/mustafa_SMP_pulses`

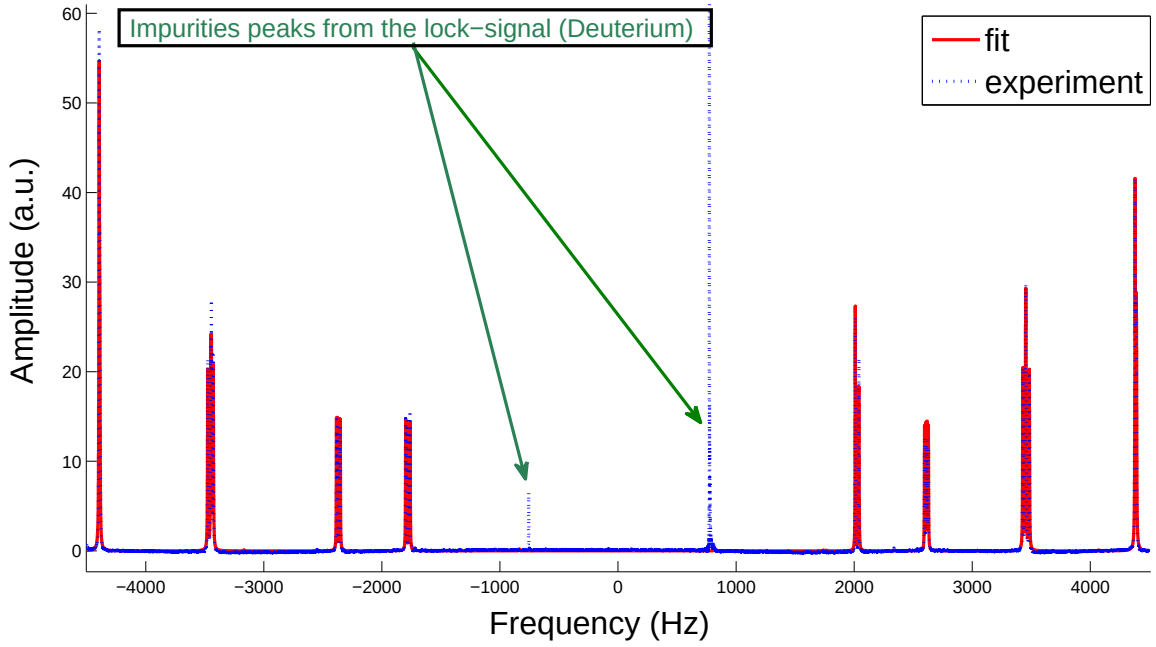

(a)

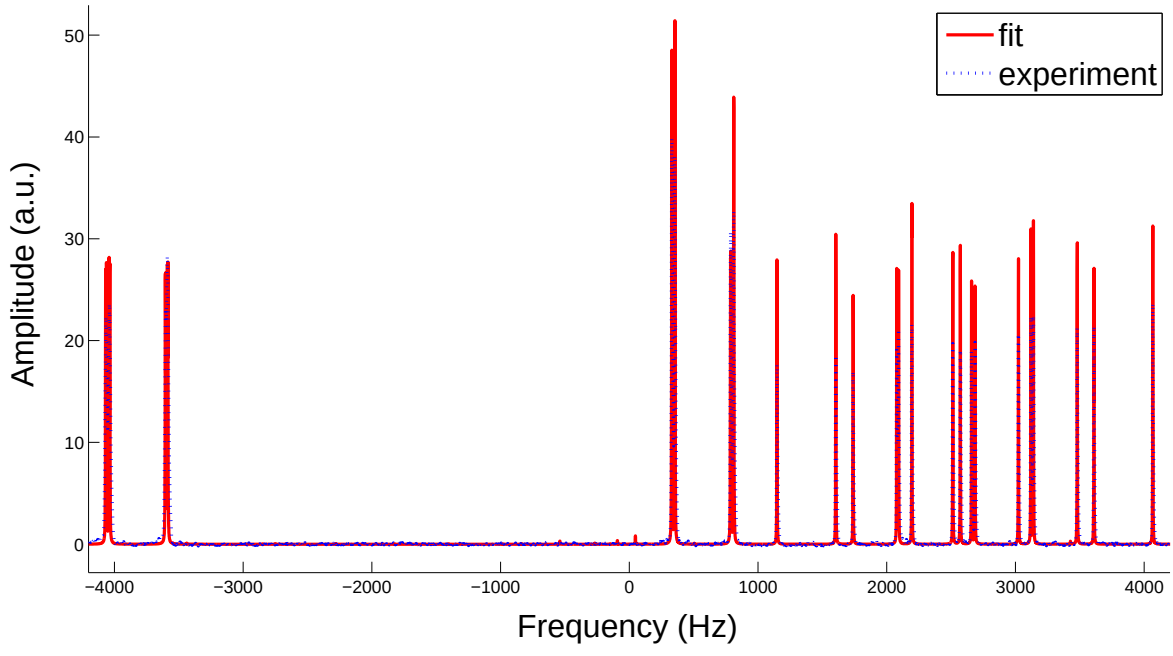

(b)

Figure 5.2.2.: a) Fitting results of the proton spins from the thermal states by a hard pulse. b) Fitting results of the fluorine spins from the thermal states by a hard pulse.

A. Signal check-up protocol in the 360 MHz Spectrometer

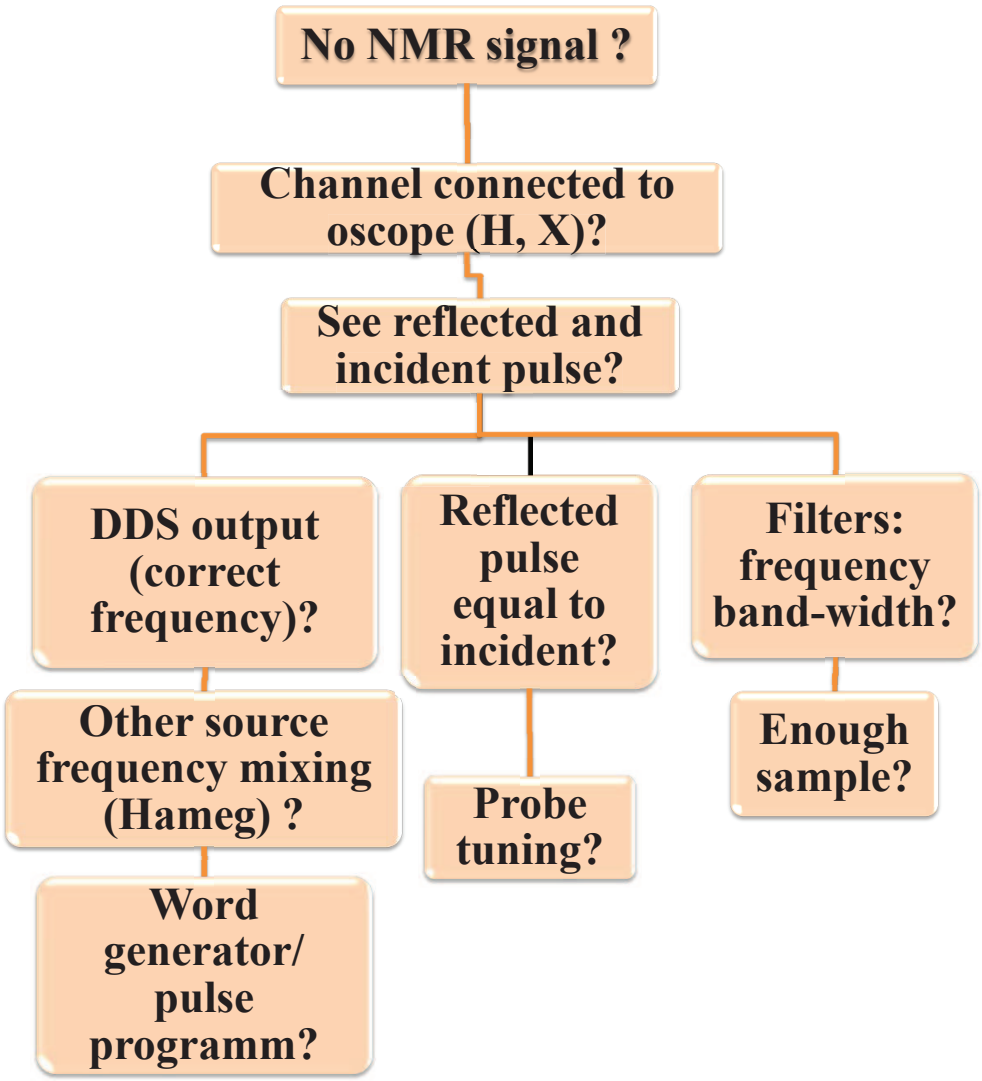

B. Interpreter pulse program: an example for multiple NMR experiments

```
1  ##################################################################
2  ### Interpreter pulse program: multiple pulse programs
3  ### Auther: Mustafa Ahmed Ali Ahmed
4  ### Sample: H2O+CuSO4
5  ### 360MHz spectrometer
6  ##################################################################
7  2D_Interpreter
8  #call the interpreter to run a multiple 2D experiments
9  pulse_program_name_1
10 #call the pulse program, this should be in the same folder
11 DATA_filename_1.1d
12 #save the data as DATA_filename_1.1d 2D_Interpreter
13 pulse_program_name_2 DATA_filename_2.2d
```

C. Interpreter pulse program: an example for a single NMR experiment

```
1  ##########################################################
2  ### Interpreter pulse program : CPMG pulse sequence
3  ### Auther: Mustafa Ahmed Ali Ahmed
4  ### Sample: H2O+CuSO4
5  ### 360MHz spectrometer
6  ##########################################################
7  !set:number_of_steps=1
8  #define the number of different experiments by changing a
       parameter (data0)
9  !set:number_of_scans=1
10 #define the number of scans for every experiment
11 !cyclops
12 #define the phase cycle by incrementing the rf pulse phase for
       four steps,
13 #every step with 90 degree
14 !digitalPhaseCorr:289,379,469,559;
15 #define the digital phase correction
16 !const:pw=35.6
17 #define a constant pi pulse
18 !const:pw_2=17.5
19 #define a constant pi/2 pulse
20 !set_2D_exp_parameters
21 #define 2D experiment parameters
22 !set:MaxPulseDurationH=2000000
23 #define the maximum pulse duration
24 !set:MaxDutyCycleH=0.09
25 #define the maximum duty cycle
26 delay;1
27 #start the pulse program after 1 microsecond delay
28 recycledelay;3
29 #3 second repetition time
30 +ddsH: phase1 =cycle0;0.26
31 #the plus sign means this step will be programmed parallel with
       the previous command, set the DDS(H) phase to zero with delay
        0.26 micro sec
```

```
32 pulseH;[pw_2]
33 #pi/2 pulse on H channel
34 +ddsH: phase1 = 0/4;0.26
35 #set the DDS(H) to zero phase with delay 0.26 micro sec
36 trigger;1
37 #send trigger signal to the oscope to start detection
38 (2000
39 #start a loop repeated 2000 times
40 acquireH;50
41 #open the receiver for 50 micro sec to detect a signal
42 +ddsH: phase1 =1/4+cycle0;0.26
43 #change the DDS phase four times by 90 degree every time
44 pulseH;[pw]
45 +ddsH: phase1 = 0/4;0.26
46 acquireH;100
47 +ddsH: phase1 =1/4+cycle0;0.26
48 pulseH;[pw]
49 +ddsH: phase1 = 0/4;0.26 acquireH;50
50 )
51 #end of the loop
52 delay;1
53 #end of the pulse program
```

Bibliography

[1] C. H. Bennett and D. P. DiVincenzo, Nature **404**, 247 (2000).

[2] J. Preskill, Proc. R. Soc. Lond. A **454**, 469 (1998).

[3] L. M. K. Vandersypen, I. L. Chuang, and D. Suter, eMagRes (2010).

[4] D. P. DiVincenzo, Fortschr. Phys. **48**, 771 (2000).

[5] J. Stolze and D. Suter, *Quantum Computing*, 2nd ed. (Wiley-VCH, Weinheim, 2008).

[6] R. Feynman, Int. J. Theor. Phys. **21**, 467 (1982).

[7] R. M. Serra and I. S. Oliveira, Phil. Trans. R. Soc. A **370**, 4615 (2012).

[8] D. Suter and T. S. Mahesh, J. Chem. Phys. **128**, 052206 (2008).

[9] I. I. Rabi, J. R. Zacharias, S. Millman, and P. Kusch, Phys. Rev. **53**, 318 (1938).

[10] N. A. Gershenfeld and I. L. Chuang, Science **275**, 350 (1997).

[11] D. G. Cory, A. F. Fahmy, and T. F. Havel, Proc. Natl. Acad. Sci. USA **94**, 1634 (1997).

[12] Quantum computation roadmap, available online at `http://qist.lanl.gov/qcomp_map.shtml`.

[13] E. R. Jenista, A. M. Stokes, R. T. Branca, and W. S. Warren, J. Chem. Phys. **131**, 204510 (2009).

[14] T. Staudacher, F. Shi, S. Pezzagna, J. Meijer, J. Du, C. A. Meriles, F. Reinhard, and J. Wrachtrup, Science **339**, 561 (2013).

[15] W. H. Zurek, Rev. Mod. Phys. **75**, 715 (2003).

[16] M. Nielsen and I. Chuang, *Quantum Computation and Quantum Information* (Cambridge University Press, Cambridge, 2000).

[17] P. Kaye, R. Laflamme, and M. Mosca, *An Introduction to Quantum Computing* (Oxford University Press, New York, 2007).

[18] G. A. Álvarez and D. Suter, Phys. Rev. Lett. **104**, 230403 (2010).

[19] A. M. Souza, G. A. Álvarez, and D. Suter, Phys. Rev. A **86**, 050301 (2012).

[20] T. D. Ladd, F. Jelezko, R. Laflamme, Y. Nakamura, C. Monroe, and J. L. O´ Brien, Nature **464**, 45 (2010).

[21] L. Viola, E. Knill, and S. Lloyd, Phys. Rev. Lett. **82**, 2417 (1999).

[22] K. Khodjasteh and D. A. Lidar, Phys. Rev. Lett. **95**, 180501 (2005).

[23] G. S. Uhrig, Phys. Rev. Lett. **98**, 100504 (2007).

[24] G. Gordon, G. Kurizki, and D. A. Lidar, Phys. Rev. Lett. **101**, 010403 (2008).

[25] J. Clausen, G. Bensky, and G. Kurizki, Phys. Rev. Lett. **104**, 040401 (2010).

[26] W. Yang, Z.-Y. Wang, and R.-B. Liu, Front. Phys. **6**, 2 (2011).

[27] J. Preskill, Proc. R. Soc. Lond. A **454**, 385 (1998).

[28] D. G. Cory, M. D. Price, W. Maas, E. Knill, R. Laflamme, W. H. Zurek, T. F. Havel, and S. S. Somaroo, Phys. Rev. Lett. **81**, 2152 (1998).

[29] E. Knill, R. Laflamme, and W. H. Zurek, Science **279**, 342 (1998).

[30] L. M. K. Vandersypen and I. L. Chuang, Rev. Mod. Phys. **76**, 1037 (2005).

[31] E. Hahn, Phys. Rev. **80**, 580 (1950).

[32] L. Cywinski, R. M. Lutchyn, C. P. Nave, and S. DasSarma, Phys. Rev. B **77**, 174509 (2008).

[33] W. Yang and R.-B. Liu, Phys. Rev. Lett. **101**, 180403 (2008).

[34] M. J. Biercuk, H. Uys, A. P. VanDevender, N. Shiga, W. M. Itano, and J. J. Bollinger, Phys. Rev. A **79**, 062324 (2009).

[35] J. Du, X. Rong, N. Zhao, Y. Wang, J. Yang, and R. B. Liu, Nature **461**, 1265 (2009).

[36] G. A. Álvarez, A. Ajoy, X. Peng, and D. Suter, Phys. Rev. A **82**, 042306 (2010).

[37] G. de Lange, Z. H. Wang, D. Rista, V. V. Dobrovitski, and R. Hanson, Science **330**, 60 (2010).

[38] C. Barthel, J. Medford, C. M. Marcus, M. P. Hanson, and A. C. Gossard, Phys. Rev. Lett. **105**, 266808 (2010).

[39] S. Pasini and G. S. Uhrig, Phys. Rev. A **81**, 012309 (2010).

[40] C. A. Ryan, J. S. Hodges, and D. G. Cory, Phys. Rev. Lett. **105**, 200402 (2010).

[41] A. Ajoy, G. A. Álvarez, and D. Suter, Phys. Rev. A **83**, 032303 (2011).

[42] A. M. Souza, G. A. Álvarez, and D. Suter, Phys. Rev. Lett. **106**, 240501 (2011).

[43] I. Almog, Y. Sagi, G. Gordon, G. Bensky, G. Kurizki, and N. Davidson, J. Phys. B. **44**, 154006 (2011).

[44] B. Roy Bardhan, P. M. Anisimov, M. K. Gupta, K. L. Brown, N. C. Jones, H. Lee, and J. P. Dowling, Phys. Rev. A **85**, 022340 (2012).

[45] Y. Pan, Z.-R. Xi, and J. Gong, J. Phys. B **44**, 175501 (2011).

[46] A. Shukla and T. S. Mahesh, (2011), arXiv:1110.1473v1 .

[47] H. Bluhm, S. Foletti, I. Neder, M. Rudner, D. Mahalu, V. Umansky, and A. Yacoby, Nat. Phys. **7**, 109 (2011).

[48] B. Naydenov, F. Dolde, L. T. Hall, C. Shin, H. Fedder, L. C. L. Hollenberg, F. Jelezko, and J. Wrachtrup, Phys. Rev. B **83**, 081201 (2011).

[49] A. G. Kofman and G. Kurizki, Phys. Rev. Lett. **87**, 270405 (2001).

[50] A. G. Kofman and G. Kurizki, Phys. Rev. Lett. **93**, 130406 (2004).

[51] J. Zhang, X. Peng, N. Rajendran, and D. Suter, Phys. Rev. A **75**, 042314 (2007).

[52] D. D. Bhaktavatsala Rao and G. Kurizki, Phys. Rev. A **83**, 032105 (2011).

[53] J. Bylander, S. Gustavsson, F. Yan, F. Yoshihara, K. Harrabi, G. Fitch, D. G. Cory, Y. Nakamura, J.-S. Tsai, and W. D. Oliver, Nat. Phys. **7**, 565 (2011).

[54] G. A. Álvarez and D. Suter, Phys. Rev. Lett. **107**, 230501 (2011).

[55] S. Kotler, N. Akerman, Y. Glickman, and R. Ozeri, Phys. Rev. Lett. **110**, 110503 (2013).

[56] N. Bar-Gill, L. Pham, C. Belthangady, D. Le Sage, P. Cappellaro, J. Maze, M. Lukin, A. Yacoby, and R. Walsworth, Nat. Commun. **3**, 858 (2012).

[57] K. Khodjasteh and D. A. Lidar, Phys. Rev. A **75**, 062310 (2007).

[58] T. E. Hodgson, L. Viola, and I. D'Amico, Phys. Rev. A **81**, 062321 (2010).

[59] Z.-H. Wang and V. V. Dobrovitski, J. Phys. B **44**, 154004 (2011).

[60] Z. Xiao, L. He, and W.-g. Wang, Phys. Rev. A **83**, 032322 (2011).

[61] K. Khodjasteh, T. Erdélyi, and L. Viola, Phys. Rev. A **83**, 020305 (2011).

[62] X. Peng, D. Suter, and D. A. Lidar, J. Phys. B **44**, 154003 (2011).

[63] Z.-H. Wang, W. Zhang, A. M. Tyryshkin, S. A. Lyon, J. W. Ager, E. E. Haller, and V. V. Dobrovitski, Phys. Rev. B **85**, 085206 (2012).

[64] A. M. Souza, G. A. Álvarez, and D. Suter, Phys. Rev. A **85**, 032306 (2012).

[65] G. A. Álvarez, A. M. Souza, and D. Suter, Phys. Rev. A **85**, 052324 (2012).

[66] A. M. Souza, G. A. Álvarez, and D. Suter, Phil. Trans. R. Soc. A **370**, 4748 (2012).

[67] L. Viola and E. Knill, Phys. Rev. Lett. **90**, 037901 (2003).

[68] J.-M. Cai, B. Naydenov, R. Pfeiffer, L. P. McGuinness, K. D. Jahnke, F. Jelezko, M. B. Plenio, and A. Retzker, New J. Phys. **14**, 113023 (2012).

[69] H. Carr and E. Purcell, Phys. Rev. **94**, 630 (1954).

[70] S. Meiboom and D. Gill, Rev. Sci. Instrum. **29**, 688 (1958).

[71] J. Keeler, *Understanding NMR Spectroscopy*, 2nd ed. (John Wiley & Sons, New York, 2010).

[72] R. Macomber, *A Complete Introduction to Modern NMR Spectroscopy*, Wiley-Interscience publication (John Wiley & Sons, New York, 1998).

[73] H. Friebolin, *Basic One- and Two-Dimensional NMR spectroscopy* (Wiley-VCH, Weinheim, 1992).

[74] M. Levitt, *Spin Dynamics: Basics of Nuclear Magnetic Resonance*, 2nd ed. (John Wiley & Sons, 2008).

[75] P. Callaghan, *Principles of Nuclear Magnetic Resonance Microscopy*, Oxford Science Publications (Oxford University Press, New York, 1994).

[76] G. Rule and T. Hitchens, *Fundamentals of Protein NMR Spectroscopy*, Focus on Structural Biology (Springer, Dordrecht, The Netherlands, 2005).

[77] A. Abragam, *Principles of Nuclear Magnetism*, International Series of Monographs on Physics (Oxford University Press, New York, 1983).

[78] R. Freeman, *A Handbook of Nuclear Magnetic Resonance* (Longman Scientific & Technical, Harlow, England, 1987).

[79] F. Bloch, Phys. Rev. **70**, 460 (1946).

[80] D. Pozar, *Microwave Engineering*, 2nd ed. (John Wiley & Sons, New York, 1998).

[81] E. da Silva, *High Frequency and Microwave Engineering* (Elsevier, London, 2001).

[82] E. Fukushima and S. Roeder, *Experimental Pulse NMR: A Nuts and Bolts Approach*, Advanced book program (Addison-Wesley, London, 1981).

[83] M. Eickhoff and H. G. Krojanski, *DDS Manual* (2004).

[84] J. Mispelter, M. Lupu, and A. Briguet, *NMR Probeheads for Biophysical and Biomedical Experiments: Theoretical Principles and Practical Guidelines* (Imperial College Press, London, 2006).

[85] J. Lambert and E. Mazzola, *Nuclear Magnetic Resonance Spectroscopy: An Introduction to Principles, Applications, and Experimental Methods* (Pearson Higher Education, Upper Saddle River, New Jersey, 2003).

[86] G. N. Chmurny and D. I. Hoult, Concepts Magn. Reson. **2**, 131 (1990).

[87] Resonance research Inc., *User Manual Matrixshim ^{TM} MHU-series*, *v* 97/8 ed.

[88] D. Hoult and R. Richards, J. Magn. Reson. **24**, 71 (1976).

[89] J. White, *High Frequency Techniques: An Introduction to RF and Microwave Engineering* (John Wiley & Sons, Hoboken, 2004).

[90] S. Vaseghi, *Advanced Digital Signal Processing and Noise Reduction* (John Wiley & Sons, Chichester, 2008).

[91] H. Ott, *Noise Reduction Techniques in Electronic Systems* (John Wiley & Sons, New York, 1988).

[92] W. G. Clark, Rev. Sci. Instrum. **35**, 316 (1964).

[93] M. Augustine, Prog. Nucl. Magn. Reson. Spectrosc. **40**, 111 (2002).

[94] G. B. J.H. Chen, A. Jerschow, Chem. Phys. Lett. **308**, 397 (1999).

[95] C. Szántay and A. Demeter, Concepts Magn. Reson. **11**, 121 (1999).

[96] R. Freeman, *Spin Choreography: Basic Steps in High Resolution NMR* (Oxford University Press, New York, 1998).

[97] X.-A. Mao and C.-H. Ye, Concepts Magn. Reson. **9**, 173 (1997).

[98] W. A. Anderson and J. T. Arnold, Phys. Rev. **101**, 511 (1956).

[99] X. an Mao, J. xin Guo, and C. hui Ye, Chem. Phys. Lett. **218**, 249 (1994).

[100] D. Burum, M. Linder, and R. Ernst, J. Magn. Reson. **43**, 463 (1981).

[101] J. Gruska, *Quantum Computing* (McGraw-Hill, New York, 1999).

[102] N. Bloembergen, E. M. Purcell, and R. V. Pound, Phys. Rev. **73**, 679 (1948).

[103] A. Maudsley, J. Magn. Reson. **69**, 488 (1986).

[104] T. Gullion, D. B. Baker, and M. S. Conradi, J. Magn. Reson. **89**, 479 (1990).

[105] H. Wittkamp, "Optimierung von geformten RF-Pulsen," Bachelorarbeit (2010).

[106] S. Pasini, P. Karbach, C. Raas, and G. S. Uhrig, Phys. Rev. A **80**, 022328 (2009).

[107] M. D. Grace, J. M. Dominy, W. M. Witzel, and M. S. Carroll, Phys. Rev. A **85**, 052313 (2012).

[108] L. Viola and E. Knill, Phys. Rev. Lett. **94**, 060502 (2005).

[109] G. Quiroz and D. A. Lidar, (2012), arXiv:1210.5538 .

[110] M. Schlosshauer, *Decoherence: and the Quantum-to-Classical Transition* (Springer, Heidelberg, 2007).

[111] M. J. Biercuk, H. Uys, A. P. VanDevender, N. Shiga, W. M. Itano, and J. J. Bollinger, Nature **458**, 996 (2009).

[112] E. L. Hahn, Phys. Rev. **77**, 297 (1950).

[113] R. Tycko, A. Pines, and J. Guckenheimer, J. Chem. Phys. **83**, 2775 (1985).

[114] U. Haeberlen and J. S. Waugh, Phys. Rev. **175**, 453 (1968).

[115] A. Pines and D. Suter, J. Magn. Reson. , 509 (2004).

[116] R. Ernst, G. Bodenhausen, and A. Wokaun, *Principles of Nuclear Magnetic Resonance in One and Two Dimensions* (Clarendon Press of Oxford University Press, Oxford, 1987).

[117] T. Ichikawa, M. Bando, Y. Kondo, and M. Nakahara, Phil. Trans. R. Soc. A **370**, 4671 (2012).

[118] J. A. Jones, (2013), arXiv:1303.1745v1 .

[119] J. Zhang, R. Laflamme, and D. Suter, Phys. Rev. Lett. **109**, 100503 (2012).

Acknowledgments

Thanks God, perhaps it is good to write this verses from the Nobel Quran: "... And if you would count the blessings of Allah you would not be able to count them..." [The Nobel Quran 14:34].

I would like to express my earnest gratitude to my supervisor Prof. Dr. Dieter Suter for giving me an opportunity to broaden my horizon. I would not have completed this thesis without his guidance, encouragement, advices and patience.

I want to sincerely thank Dr. Gonzalo A. Álvarez who introduced me to the field of quantum computation and played an essential role in completion of this work. I truly appreciate the help and valuable advices of Dr. Jingfu Zhang and Prof. Dr. Alexander Martins de Souza.

I would like to thank Prof. Dr. Götz S. Uhrig for reading this thesis and giving valuable comments. Thanks are also extended to the examination committee.

It is a pleasure for me to thank Dr. Reiner Küchler who helped me to carry out my first NMR experiment, six years ago, and further supported me in experimental techniques. I'm grateful to the technical and administrative support of Angelika Sommer, Anja Sapsford, Walerian Goralcyk and Horst Rombeck as well as answering personal questions.

I would like to acknowledge the friendly atmosphere and scientific cooperation from all current and previous members of E3 group. I appreciate the help of Andranik Baghdasaryan, Rahuman Sheriff and Wulayimu Maimaiti in grammar and misspelling corrections while writing this thesis.

The workshops at the Physics Department allowed technical implementation of many projects. For the effective cooperation, I would like to thank all employees of Development of electronics, Electronics Workshop, Mechanical Workshop, Preparation laboratory and low temperature unit.

I would also like to acknowledge the financial support from the International University of Africa in Sudan.

I'm grateful to my mother Maryam Mergani who always keeps praying for me. Thanks for the love and patience of my wife, Sarah Saeed and my children, Abdelrahman and Maryam (who were born during the period of this work). Lastly I would like to thank everyone who directly or indirectly helped me to finish this thesis.